Unterschrift des Betreuers

TECHNISCHE
UNIVERSITÄT
WIEN

VIENNA
UNIVERSITY OF
TECHNOLOGY

DIPLOMARBEIT

Quality Assurance and Performance Tests of Silicon Detector Modules for the CMS/Tracker

ausgeführt am

Institut für Hochenergiephysik
der Österreichischen Akademie der Wissenschaften

und am

Atominstitut
der Österreichischen Universitäten

unter Anleitung von
Univ.Doz. Dipl.-Ing. Dr.techn. Manfred KRAMMER

durch

Marko Dragicevic
<dragicevic@hephy.oeaw.ac.at>

Kaiserstrasse 43/9
1070 Wien

1. Mai 2005

Unterschrift

Abstract

After providing a short overview of the LHC accelerator, the CMS experiment and it's various detector systems, we will have an in-depth look on silicon semiconductor particle detectors. Various important aspects like theoretical principles, radiation damage and actual design considerations are discussed and the quality assurance scheme for the sensor and module production is introduced. A strong emphasis is made on the ARC module teststand which was set up and operated be the author.

Another important aspect in establishing a good quality assurance scheme is flexibility and keeping an eye on the unexpected. At one such occasion, the author had to gather custom made test equipment, to investigate certain effects in silicon sensors manufactured by ST Microelectronics. Conclusions from these measurement could only be drawn very cautiously, as the manufacturing process and many of its subtle changes, remained a well kept secret of the company. Nevertheless, the investigations proofed to be useful and ST Microelectronics was able to remedy the problems.

A manufacturing, assembly and quality assurance process can only be declared successful, when the final *product* in the end is working within the specifications. To prove that this is true for the CMS tracker detector modules, the author joined a collaboration of young physicists to examine the performance of a selection of modules in a testbeam at the DESY research facility in Hamburg, Germany. As a novelty, fully irradiated CMS detector modules where put into a testbeam for the very first time. It will be shown, that module types used in this testbeam are capable of working well within specs even after experiencing the full 10 years of LHC lifetime.

Contents

		LEP	TEVA-TRON	HERA	LHC
physics start		1989	1987	1992	2007
particles		e^+e^-	p$\bar{p}$	ep	pp
beam energy	$E_{Beam}[GeV]$	105 GeV	1 TeV	e:30 GeV p:920 GeV	7 TeV
center of mass energy	$E_{cm}[GeV]$	210 GeV	1 TeV	300 GeV	14 TeV
Luminosity	$\mathcal{L}[cm^{-2}s^{-1}]$	2.2×10^{31}	2.1×10^{32}	1.4×10^{31}	10^{34}

Table 1: List of most important key features of some major colliding machines built up to now - data from oktober 2004.

1 The Large Hadron Collider

Man's thriving thirst for a better understanding of our universe, has led to the construction of ever more complex, bigger, and most problematically, more expensive machines to probe nature. Among these efforts, the building of large colliding machines is definitely one of the most enticing and demanding tasks. Basically being a gigantic microscope, particle accelerators are the most efficient tools thought of, to discover the secrets that lay beyond subatomic region. Not only do they allow a glimpse on how matter is constructed and forces are interacting, it also gives a keen insight on the beginning of the Universe and numerous other aspects not only science but mankind itself is so eager to uncover.

Starting in the early 30's with the *Van de Graaff Generator* up to recently built and operated machines like the SLC in Stanford, or the LEP in CERN, particle accelerators and their accompanying experiments became ever more challenging. The latest and biggest (and probably also the last of it's kind), is the *Large Hadron Collider* (LHC).

1.1 The Machine

From 1989 till end of 2000 the LEP, a synchrotron accelerating electrons and protons up to ≈105 GeV was operated very successfully at CERN, Geneva. After dismantling the machine, the old LEP tunnel - a 100 meter below the Jura with a circumfence of about 27 km - became the home for the LHC. Since R&D for the new machine began back in 90s, its key features changed several times. Table 1.1 shows the most important specs that were up to date in October 2004.

After some controversy concerning the shutdown date of LEP in the light of some new possible discoverys (some faint hints on the Higgs Particle showed up), dismantling of the old machind and construction of the LHC and its accompanying 4 experiments started.

The LHC will be capable of accelerating protons up to 7 TeV resulting in a center-of-mass energy of 14 TeV and colliding them at a luminosity of $10^{32}cm^{-2}s{-}1$. These two parameters are the most important characteristics of an accelerator.

- Center-of-Mass Energy $E_{cm}[GeV]$: quantifies the energy that is available for particle production at the center-of-mass. In colliding beam experiments with two particle beams of equal mass and kinetic energy this equals two times the beam energy $E_{Beam}[GeV]$ as the center-of-mass is not moving at the interaction point. For fixed target experiments, only a fraction of E_{Beam} is available for particle production.

- Luminosity $\mathcal{L}[cm^{-2}s^{-1}]$: describes the probability for an interaction between two colliding particle bunches. It can be easily derived from the beam geometry, the bunch dimensions and the bunch timing:

  $$\mathcal{L} = f \frac{n^2}{4\pi\sigma_x\sigma_y}, \tag{1}$$

  where

  f ... bunch crossing frequency
  n ... number of particles per bunch
  σ_x... beam dimension in x coordinate
  σ_y... beam dimension in y coordinate

  Now, this provides us an easy way to calculate the event rate of a given process:

  $$R = \mathcal{L}\sigma \tag{2}$$

  Reaching high luminosities is essential to get a high rate if interactions, as most *interesting* processes have very low cross sections.

One of the major constrains put to the LHC and ring colliders in general, is the emission of *synchrotron radiation.* As charged particles are accelerated, they are radiating electromagnetical waves. On a circular track, even when the particles are not gaining any more velocity, the centripetal force still is an acceleration. The energy loss due to the emitted EM-radiation is described by:

$$\frac{dE}{dT} = \frac{e^2c}{6\pi\epsilon_0 R^2}\frac{E_p^2}{(m_oc^2)^4}, \tag{3}$$

where

E ... energy loss due to radiation
T ... cycle duration
ϵ_0 ... dielectric constant of vacuum
R ... radius of the particle trajectory
E_p... kinetic energy of the particle
m_0... rest mass of the particle

This equation is governed by to factors: the inverse square of the accelerators diameter, and the relation of the particles energy to its rest mass. As a consequence of these problems, the insane circumference of 27 km and the use of protons (which are 1836 times heavier than electrons) should make the LHC feasible.

1.2 Physics at LHC

Previous generations of particle accelerators have led to a deep understanding of the forces that govern the subatomic world. This understanding has been incorporated in the so called *Standard Model* (SM). So far the SM has proven to be an exceptional tool to describe and predict particle interactions.

At the core, the SM describes 2 kinds of particles: *bosons* and *fermions.* While bosons are spin 1 particles (therefore obey the *bose statistic*) and the carriers of the three fundamental forces, the fermions have spin 1/2 (therefore obey the *fermi statistic*) and form the constituents of the known observable matter in the universe.

The fermions are differentiated into *leptons* and *quarks*, where only quarks take part in strong interaction. Each of these families is then further classified into 3 generations, each consisting of 2 particles. The four fermions in each generation behave almost exactly as their counterparts in the other generations, but they have a different mass and usually higher generation fermions are quickly decaying into first generation ones. Furthermore there exists an antiparticle to each of the 12 fermions, which mimics most properties like mass and spin, but swapping positive - negative electric charges and color - anticolor.

To sum it all up (omitting antiparticles):

Fermions spin 1/2

Leptons

Flavor	Mass GeV/c^2	Charge
electron e	511×10^{-6}	-1
e neutrino ν_e	$< 1 \times 10^{-8}$	0
muon μ	0.106	-1
μ neutrino ν_μ	$< 2 \times 10^{-4}$	0
tau τ	1.7771	-1
τ neutrino ν_{tau}	< 0.02	0

Quarks

Flavor	Mass GeV/c^2	Charge
up u	3×10^{-3}	2/3
down d	6×10^{-3}	-1/3
charm c	1,3	2/3
strange s	0.1×10^{-3}	-1/3
top t	175	2/3
bottom b	4,3	-1/3

Bosons spin 1

Name	Mass GeV/c^2	Charge
photon γ	0	0
W^-	80,4	-1
W^+	80,4	+1
Z^0	91,187	0
gluon g	0	0

All the matter that is seen in our macroscopic world is made of first generation particles only. The nucleus of atoms is made of protons and neutrons, which are categorized as *Baryons* because they are made of 3 quarks. Only first generation quarks are contained in protons (uud) and neutrons (udd). The nuclei is held together by the strong and the weak interaction or, to put it in other words, by the exchange of gauge bosons - $W^\pm$ and Z^0 bosons for the weak interaction and gluons for the strong interaction.

Electrons form the outer "shell" of atoms and are tied to the nucleus by electromagnetic force which is carried by photons.

Neutrinos exist in vast numbers around us (most of them produced in the hot furnace of the sun), but as they only interact weakly[1] (leptons do not take part in strong interactions and neutrinos are electrically neutral) they are very hard to detect.

While the SM describes most of the interactions seen so far with astonishing accuracy, it still has some flaws. The LHC is believed to be quite the right tool to solve at least some of those mysteries.

1.2.1 The Higgs Boson

One of the main problems of the SM is that the exchange bosons should have zero mass. Previous experiments have already proven, that this is true for gluons and for photons, but contradictionary the W and Z bosons are heavy particles. To remedy this problem, theorist introduced the so-called *Higgs-field.* Because of a non vanishing vacuum expectation value, this field is not subject to *symmetry breaking* and is automatically giving mass to the weak interaction gauge bosons. Additionally, one gets the masses of the fermions as well, as these particles couple to the spin 0 higgs boson.

Until now, the Higgs boson is only hypothetical and has not been measured yet. According to the theorie's prediction, the Higgs mass must be quite large - more than 114GeV -as the LHC's predecessor, the *Large Electron Positron* (LEP) collider was not able to find the Higgs boson up to $\approx 110 GeV$. The LHC will be able to easily surpass this value and far beyond, to prove the Higgs theory to be either another perfect triumph of physics (and maybe a hot topic for swedish gold[2]), or not to be incorporated in nature.

1.2.2 CP Violation

One of the main mysteries of cosmology is the simple fact that we live in an universe with more matter than antimatter. When introducing the concept of the *Big Bang* one would naturally assume that matter and antimatter would synthesize perfectly symmetrical. But - fortunately - there was slightly more matter after the Big Bang, nevertheless the mechanisms that made that possible, are not yet understood.

One of the most promising attempts to solve this riddle is the concept of Charge Parity (CP) violation. The standard model already describes CP violation in weak interactions, although it is not enough to explain the abundance of matter in the universe.

An interesting decay mode that could reveal some new insights on CP-violation and which is accessible by the LHC is, the B-meson systems. Due to the high luminosity of the LHC it should be possible to make precise measurements of the Cabibbo-Kobayashi-Maskawa-matrix V_{CKM} which is an unitary matrix describing the mixing of down-type (d,s,b) to up-type (u,c,t) quarks.

1.2.3 SUSY search

A very promising extension of the SM is *Super-Symmetry* (SUSY). It postulates a symmetry that relates bosons and fermions giving every fermion a SUSY

---

[1] they only take part in the weak force - but that also means that they generally interact very weakly with other matter

[2] also known as *Nobel Prize*

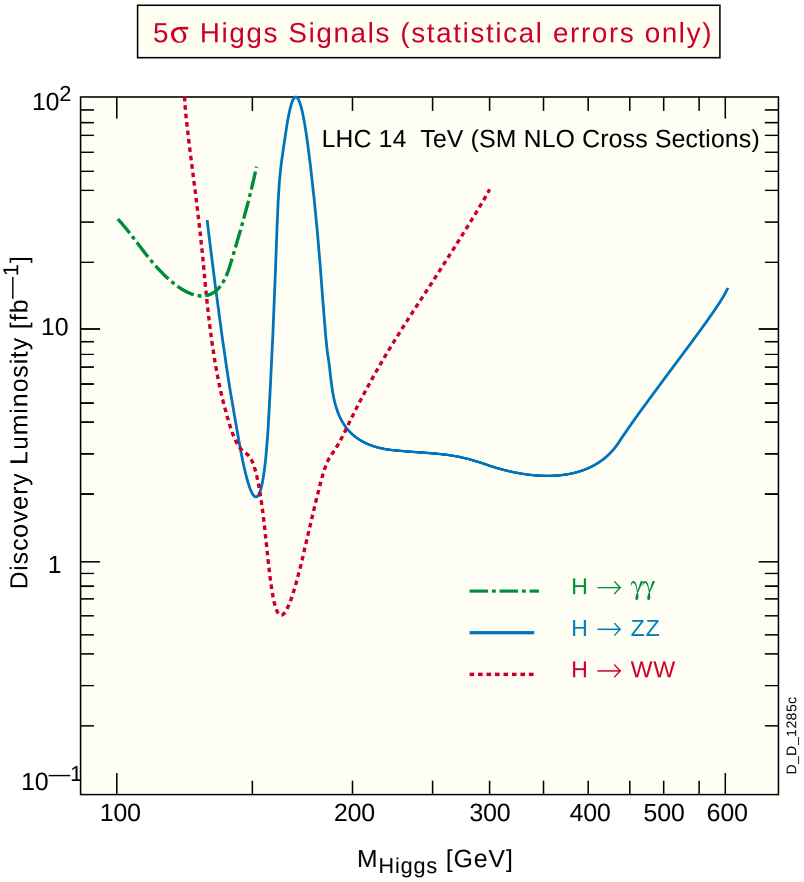

Figure 1: Integrated luminosity required for the discovery (5 σ signal-to-background ratio) of the Higgs as a function of the Higgs mass.

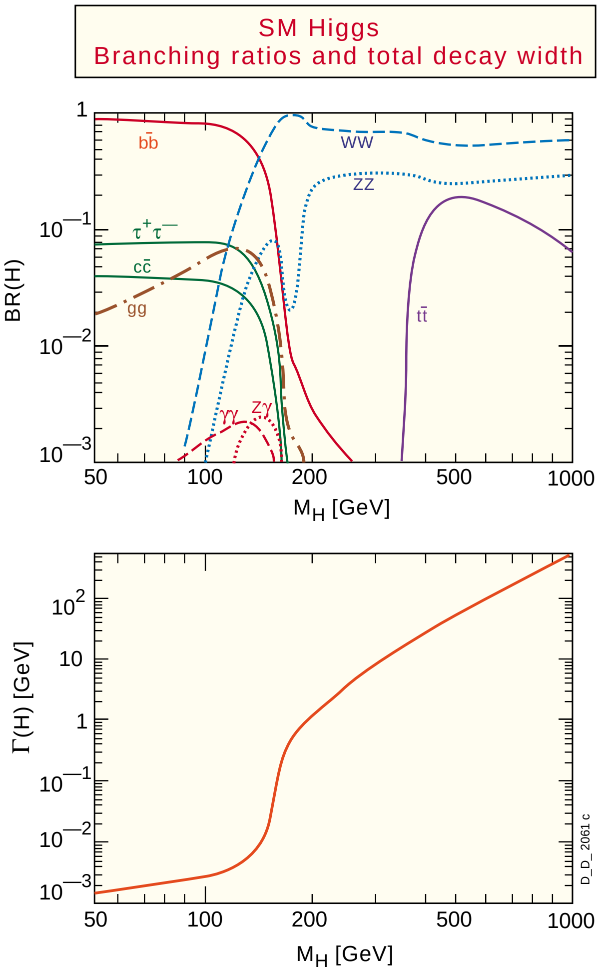

Figure 2: Branching ratios and decay width for the SM Higgs-boson as a function of its mass.

partner which is a boson and vice versa. Most of these supersymmetric partners are expected to be very heavy, which has prevented discovery until now but the LHC should be capable of seeing signatures originating from such SUSY particles.

SUSY is also one of the main foundations needed for more sophisticated theories like *string theory.* Although the region were string theory would become visible are far from attainable - even in the far future, SUSY signature might be a first touchstone for either making these theories basically possible or eradicating them as a possible description of our nature.

1.2.4 Quark Gluon Plasma

A Quark Gluon Plasma is believed to be a new phase of hadronic matter which governed the universe during its first few instants after the Big Bang. These conditions can be simulated by the LHC by colliding heavy ions.

2 The Compact Muon Solenoid

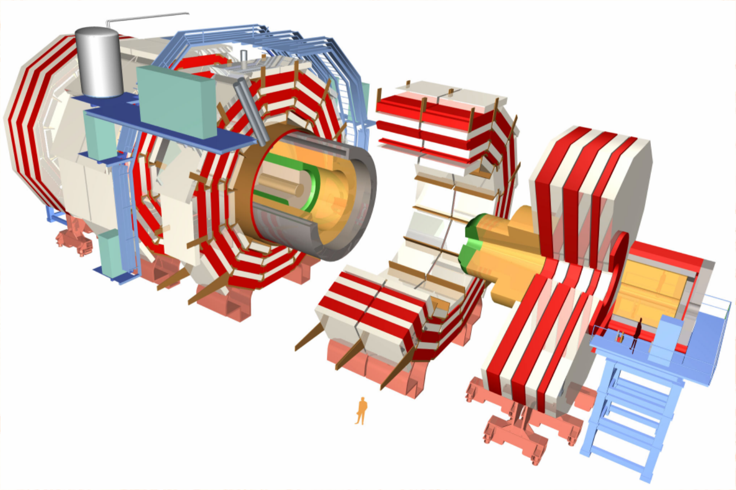

Total weight:	12,500 t
Overall diameter:	15 m
Overall length:	21.6 m
Magnetic field:	4 Tesla
Detector Channels:	15,000,000

The LHC will incorporate 4 different Experiments, 2 specialized ones - *A Large Ion Collider Experiment* (ALICE)[3] and *Large Hadron Collider beauty experiment* (LHCb)[4] and two multi purpose ones - *A Toroidal LHC ApparatuS* (ATLAS) and *Compact Muon Solenoid* (CMS).

The CMS experiment is bound to have a very performant muon detection system to identify muon jets caused by proton-proton interactions. This led to a design incorporating a strong superconducting magnet system enabling the muon chambers to be relatively small. Allthough the ATLAS experiment is 8 times bigger in terms of volume, the total mass of CMS of 12500 tons is twice the mass of ATLAS. So the CMS name gives credit to these three key features: compactness, muon chambers and the superconducting solenoid.

As fig. 3 shows, the several layers of detectors are structured like onionskins, but in a cylindrical form. The collision point is surrounded by the silicon tracker, the pixel detector in the very center. Next are the calorimeters, while the muon chambers form the most outward detector layer. Each consecutive detector layer is more voluminous and more massive. This comes quite naturally, as the innermost part - the tracker, should measure the precise particle tracks without influencing them, while the calorimeters should absorb the particles to measure their energy.

To see how different particles are traversing the detector, producing distinctive signatures in each of the detectors, fig. 4 shows a transverse slice of the CMS experiment. It can be divided into three parts: Tracker, calorimeters and muon chambers.

---

[3] Aimed at studying quark-gluon plasma

[4] Aimed at precise measurements of CP violation

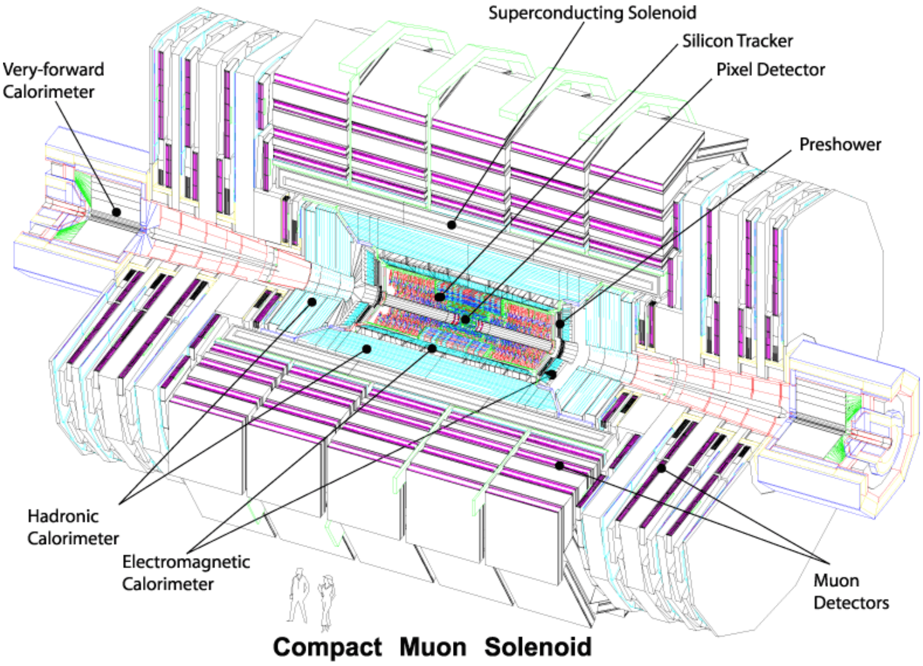

Figure 3: The onion like structure of the CMS detectors.

In the innermost layer, the *silicon tracker* is capable of precisely measuring the tracks of charged particles. The tracks are all curved because of the high 4 Tesla field which is produced by the superconducting solenoid. This already gives some data on the particle momentum as well. Neutral hadrons, such as neutrons are traversing the tracker in a straight line, not exciting any signal.

The *calorimeters* will then absorb and measure the energy of most charged and neutral particles. Light particles which are interacting electromagnetically like the electron and the photon, are stopped in the *Electromagnetic CALorimeter* (ECAL) while the heavier hadrons, charged and neutral, shower in the *Hadronic CALorimeter* (HCAL).

Muons are the only charged particles able to escape the calorimeters. They are then detected by the muon chambers in the outermost layer. Only the barely interacting neutrinos cannot be detected anywhere in the detectors. The only way to get some information about them is to sum up the energies and momenta of all other particles and attribute the missing fraction to the neutrinos.

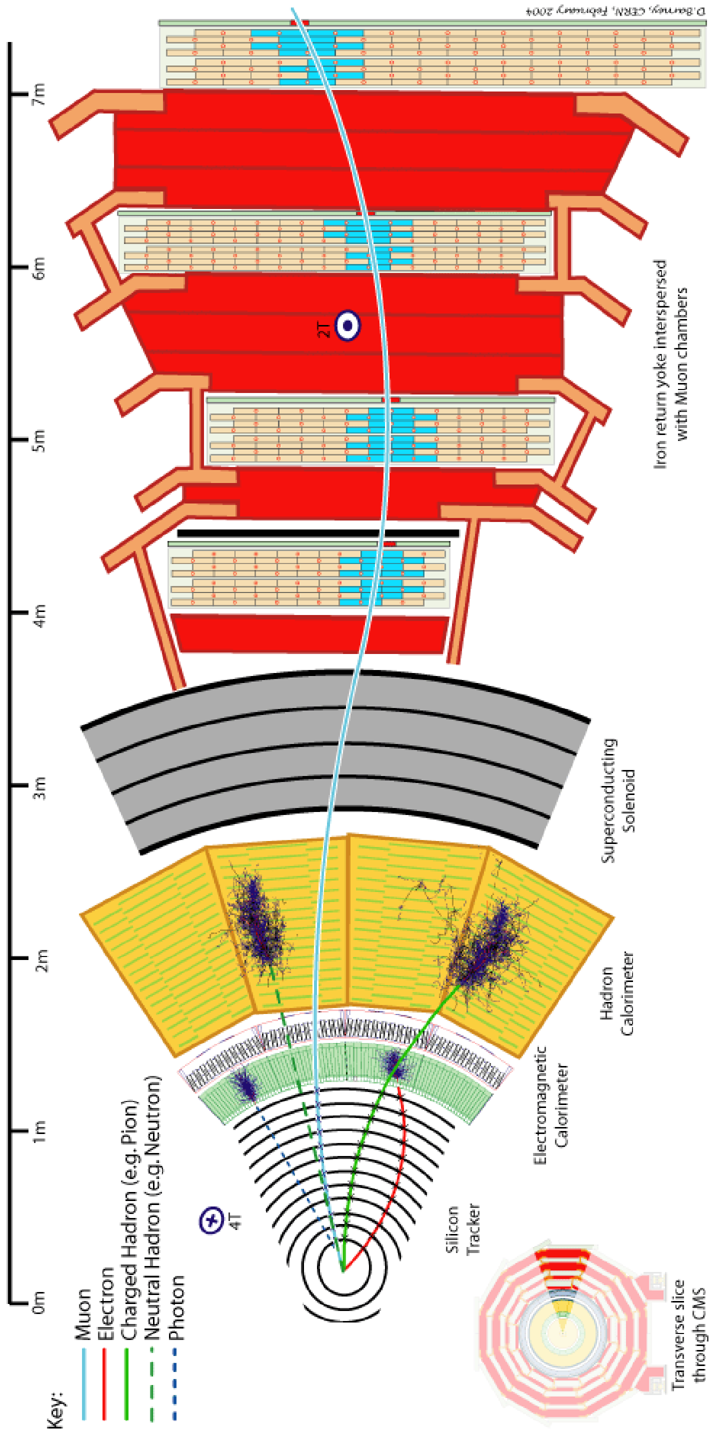

Figure 4: A transverse slice of the CMS experiment. Typical signatures of different particle types are shown.

2.1 The Tracker System

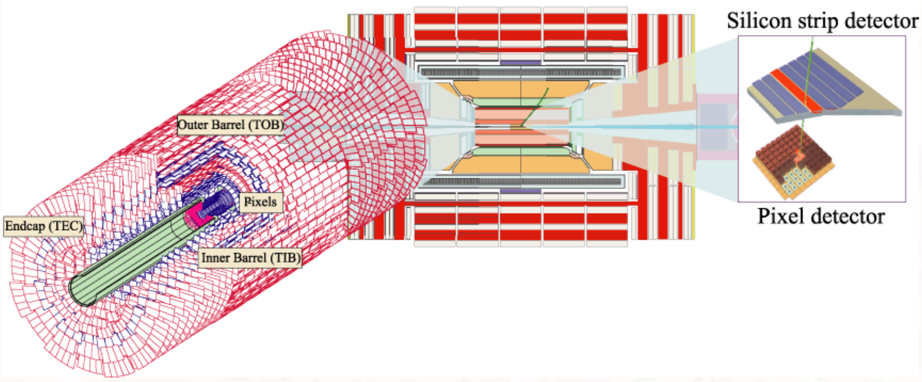

Overall Diameter:	2.4 m
Overall length:	5.4 m
Number of sensors:	25000
Active silicon area:	206 m^2
Running temperature:	$-10°$C
Humidity:	$<$ 30% RHD for 10 years

According to the initial proposal, the *CMS tracker* should have been equipped with *MicroStrip Gas Chambers* (MSGC). But due to problems with ageing and high voltage stability this concept was dropped in favor of an even more daring detector: an all silicon tracker. Containing multiple layers of semiconducting material the area covered by silicon adds up to 206 m^2 - the world largest silicon device!

The design of the tracker should enable it to make precise measurements of charged particle tracks. Two very important key elements are then extracted from the gained data:

- The vertex of a particle is reconstructed to determine its creation point and to compare the actual data with the calculated processes. As most interesting particles only have a very limited lifetime, two vertices can be very close to each other and to distinguish them, the reconstructed tracks have to be very precise.
- Due to the large 4 Tesla magnetic field sustained by the solenoid coil, the charged particles traverse the tracker on curved tracks. This enables the calculation of the transverse momentum and, quite easily by looking at the orientation of the curvature, gives the polarity of the charged particle.

The calculation of the transverse momentum follows a very simple concept. Due to the high magnetic field, the trajectory of a charged particles is a helix with the radius R. The momentum perpendicular to the B-filed can than be determined (non relativistic) by

$$p_T = qBR, \tag{4}$$

where q is the electric charge of the particle and B the magnetic field.

One of the main problems for the tracker is the harsh radiation environment. This is especially crucial in the innermost layers of the tracker where the applied dose is the largest (see fig. 5).

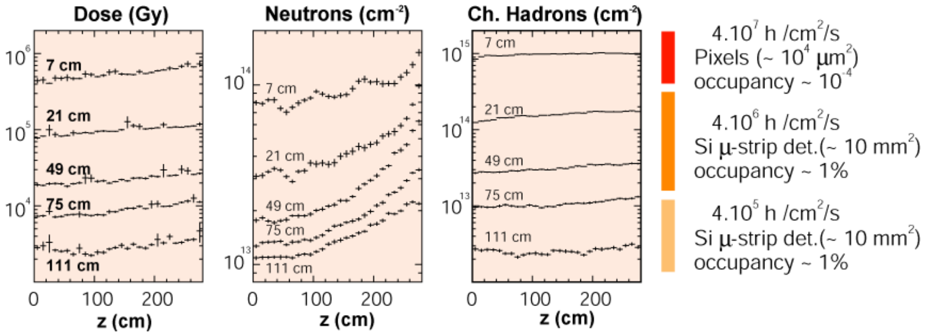

Figure 5: Dose rates and particle densities as a function of the distance from the interaction point.

The tracker collaboration opted for a two stage system, a small pixel device for the innermost layers, surrounded by a silicon strip detector. The pixel system, which is exposed to the highest radiation level will have a limited lifetime only, therefore it will be deployed inside the tracker, when the first full physics runs are scheduled for CMS. This way the precious device is not wasted for mere calibration or machine development runs.

The strip detector is exposed to much lower radiation levels but still radiation hardness was an very important issue to make the device withstand the full 10 years of the CMS environment. This is discussed in more detail in section 3.2.

2.2 Calorimetry

The main task of a calorimeter is the determination of a particles energy. This is done by completely absorbing the particles in an appropriate absorber material. Only muons and neutrinos are capable of escaping the calorimeters but the former ones can still be detected and measured in the muon chambers. To achieve a precise measurement of the neutrino energy it is very important for the detector to be completely hermetical for all other hadrons and leptons. That way it is possible to simply attribute the missing integral energy to the neutrinos.

Due to the different behaviour of hadrons and leptons in matter the calorimeter comprises two different systems, one for hadrons and one for electromagnetically interacting fermions and bosons like electrons and photons.

2.2.1 Electromagnetic Calorimeter

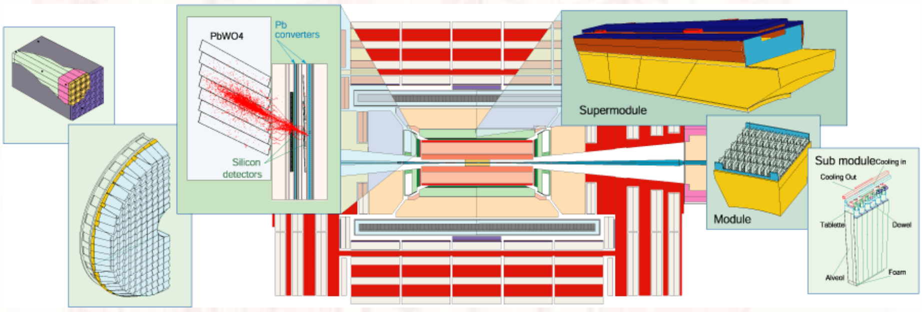

Number of crystals:	≈ 80,000
Total crystal volume:	11.18 m^3
Total crystal wheight:	92.6 t

The ECAL's purpose is to capture lightweight particles, which are interacting electromagnetically like electrons and photons. They deposit their energy in electromagnetic showers while heavier fermions like muons, protons and neutrons pass the detector due to their much higher mass.

Two parameters are very important when characterizing the performance of an electromagnetic calorimeter:

Radiation Length Within one *radiation length* X_0 a particle is typically interacting once with the matter it is traversing. So electrons would radiate a photon, while photons would create an electron-positron pair.

Molier Radius As the created secondary particles are interacting with matter again, producing particles themselves, the absorption process of the incident particle is triggering an electromagnetic shower of photons and electrons. The transversal dimensions of such shower are described by the *molier radius.*

The energy of the incident particle is often detected by measuring the photon emission of a scintillator which is proportional to the deposited energy. For the CMS detector, high density lead tungsten crystals ($PbWO_4$)(see fig. 7) have been selected for their short radiation length and their small molier radius which gives the calorimeter a good resolution(see fig. 6). Radiation hardness is another major factor, which is fulfilled by the chosen material. The light yield is not influenced by the radiation, but the crystal looses transparency. This is measured by a light injection mechanism, which records the crystals translucency and a compensation factor can be calculated.

2.2.2 Hadronic Calorimeter

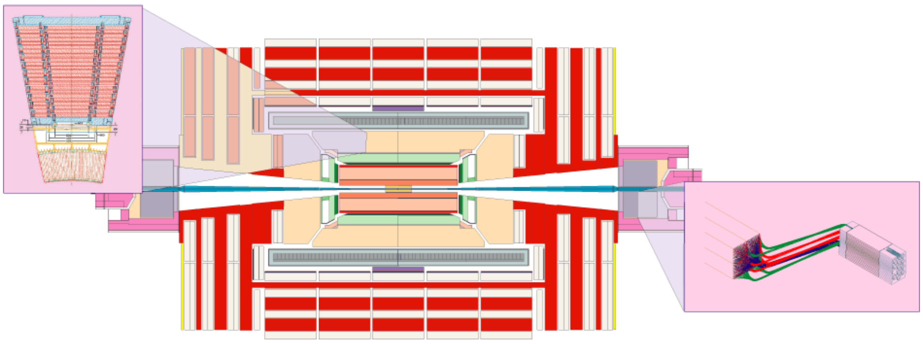

The Hadronic Calorimeter (HCAL), plays an essential role in the identification and measurement of quarks, gluons, and neutrinos by measuring the energy and direction of jets and of missing transverse energy flow in events. Missing energy forms a crucial signature of new particles, like the supersymmetric partners of quarks and gluons. For good missing energy resolution, a hermetic calorimetry coverage to $|\eta|$=5 is required. The HCAL will also aid in the identification of electrons, photons and muons in conjunction with the tracker, electromagnetic calorimeter, and muon systems.

A Hadron calorimeter is usually made of two components: an absorber material, which is creating *hadronic showers* via strong interaction with the nuclei and an detection material which is measuring the released energy. At CMS the HCAL is outfitted with 50mm thick copper plates interleaved with 4mm thick scintillator sheets (see fig. 8).

Similar to the ECAL a parameter called *absorption length* (λ) describes the major performance factor. To achieve the desired value of approximately 11λ,

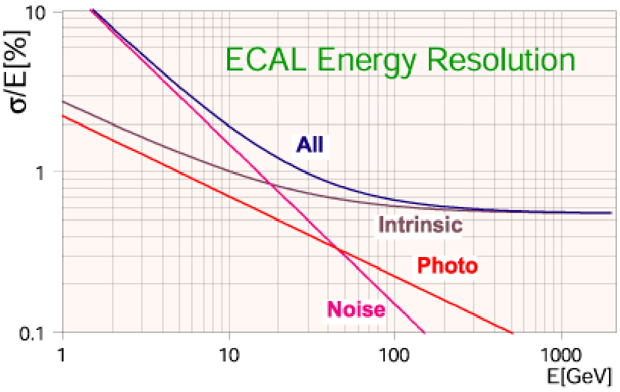

Figure 6: Energy resolution is driven by three factors: photostatics, electronic noise and constant term.

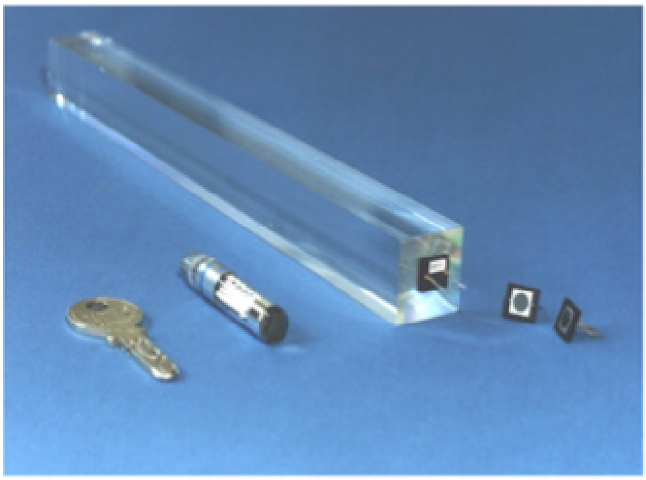

Figure 7: The CMS electromagnetic calorimeter will consist of over 80,000 lead-tungstate (PbWO4) crystals equipped with avalanche photodiodes or vacuum phototriodes and associated electronics.

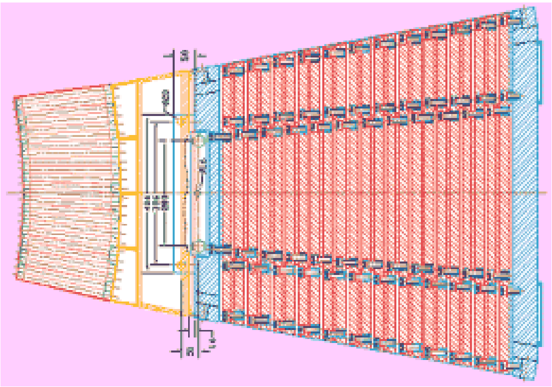

Figure 8: A wedge consisting of alternate layers of absorber (copper) and detector (scintillator) sheets.

an *outer barrel calorimeter* situated just outside the magnet coils had to be installed.

2.3 The Magnet System

The CMS magnet system comprises a *superconducting coil* and a massive *iron return yoke*. The coil must be embedded inside a vacuum tank and several ancillaries such as cryogenics, high current power supplies are need to operate the system. With a total weight of about 12,000 tons it will be the largest superconducting magnet system to date. The energy stored inside the coil would suffice to melt 18 tons of gold!

One of the major aspects of designing a good detector is the configuration of the magnetic field. The measurement of the momentum of charged particles is based on the bending of their trajectories. Together with a precise alignment of the individual detector systems, a large bending power is one of the major factors in achieving a high momentum resolution.

2.3.1 The Superconducting Solenoid

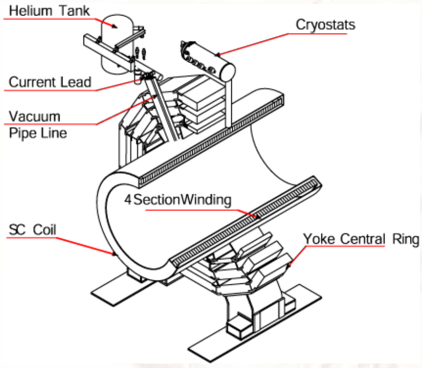

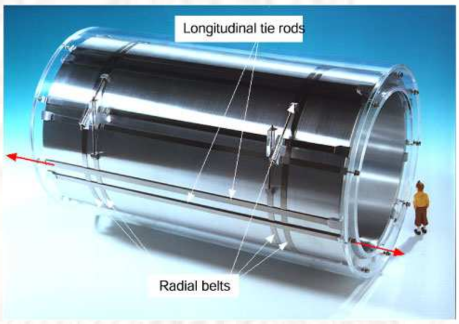

Free inner diameter:	5.9 m
Overall length:	13 m
Coil weight:	220 t
Magnetic field:	4 Tesla
Stored energy:	2.7 GJ
Axial compression force	148 MN

The CMS design of the superconducting coil favored a solenoid over a toroidal layout because of smaller size for similar bending power. Still, the inner radius of the coil is large enough to accommodate the inner tracker and the calorimeters.

Additionally a solenoid provides a field parallel to the beam where the bending of the tracks is in the transverse plane, determining the transverse position of the vertex with better accuracy. The strong bending in this plane allows triggering on tracks from the vertex.

The high magnetic field of 4 Tesla is of utmost important for efficient triggering on muons. It is high enough to saturate the complete return yoke, while a 3 Tesla field could only saturate the first 1.1 m. This would lead to significantly decreased efficiency of the 1st level trigger (see fig. 9)

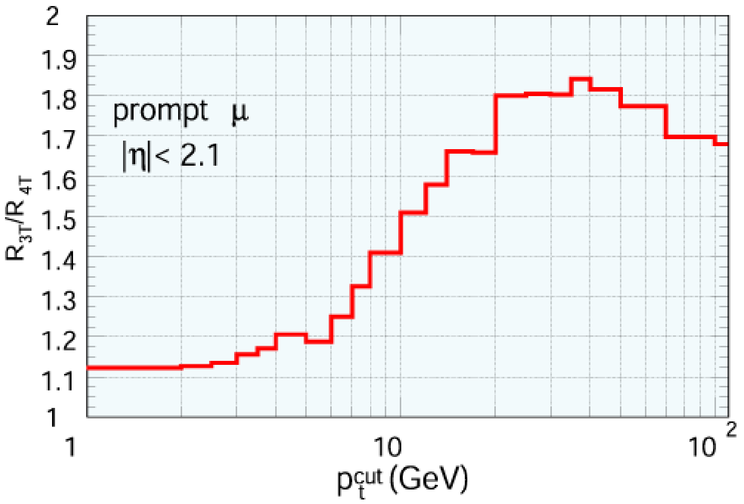

Figure 9: The effect of a different magnetic field strength on the single-muon trigger rate for a 4 T to a 3 T field. For high momentum muons this would give almost a factor of 2 difference in the trigger rate.

2.3.2 The Magnet Return Yoke

Diameter:	14 m
Overall length:	21.6 m
Thickness:	1.5 m
Coil weight:	12000 t
Maximum attraction force	85 MN

The *magnet return yoke* is a massive construction made of about 12000 t of iron. This is approximately the same amount of iron used in the eiffel tower!

The system is designed as a 12-sided cylindrical structure made of 5 rings for the barrel part and 2 endcaps. Each ring is divided into 3 layers, where the innermost one supports the superconducting coil while the space between the individual layers is equipped with *muon chamber*.

Another important design feature of the yoke is, that only the central barrel ring is a stationary part, while all other 4 barrel rings and the endcaps are running on floor rails. This enables insertion and maintenance of the muon stations.

2.4 The Muon System

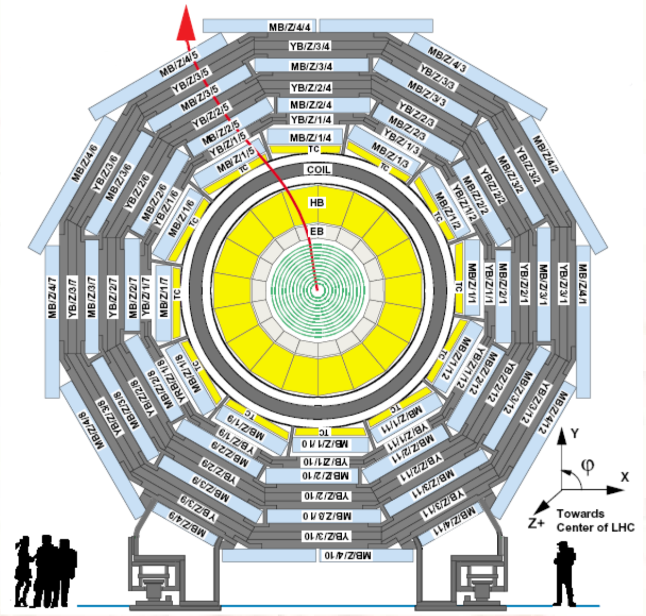

Number of DTs:	250
Number of CSCs:	540
Number of RPCs:	1020

As muons are expected to provide clean signals for a wide range of physics processes, the *muon system* is very important for the CMS experiment. The detectors are placed in four layers inside the magnet return yoke. Particles passing the inner layers of the experiment have already gone through at least 10 interaction lengths. Only muons (and of course the almost non-interacting neutrinos) should be able to get that far. The muon system has two major tasks:

- Identify and precisely measure the momentum (together with the tracker) of muons
- Provide fast trigger information

To achieve the designated performance, the system will use three types of detectors (see fig. 10): *Drift Tubes* (DT) and *Cathode Strip Chambers* (CSC) to obtain precise measurement of momentum and position and *Resistive Plate Chambers* (RPC) to provide fast information for a fast first level trigger.

All of the three different detectors are gaseous detectors and share some common features:

- They are filled with a gas which gets ionized when a charged particle (muon) traverses the detector.
- Charges are collected by HV electrodes, which pick up the signal.
- The generated charges are amplified by the gas multiplication effect. The multiplication factor can be quite high when the anode is made of a thin wire.

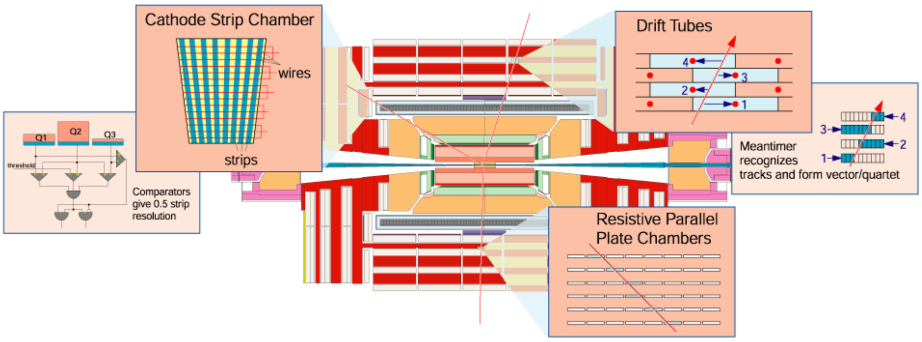

Figure 10: The 3 types of detectors used for the muon system.

2.4.1 Drift Tubes

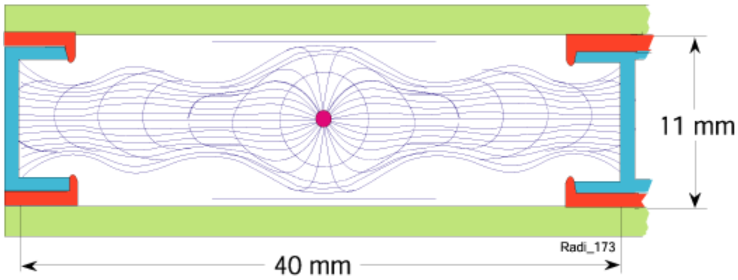

Drift tubes are located in the barrel only, where the magnetic field is guided and almost fully contained by the iron yoke. Each of the four centimeter wide tubes contain a single wire. When the muon passes through the tube, it ionizes the gas inside. The liberated electrons move along the field lines to the positively charged wire. The coordinate perpendicular to the wire axes is calculated by measuring the time taken by the ionization electrons to migrate to the wire.

2.4.2 Cathode Strip Chambers

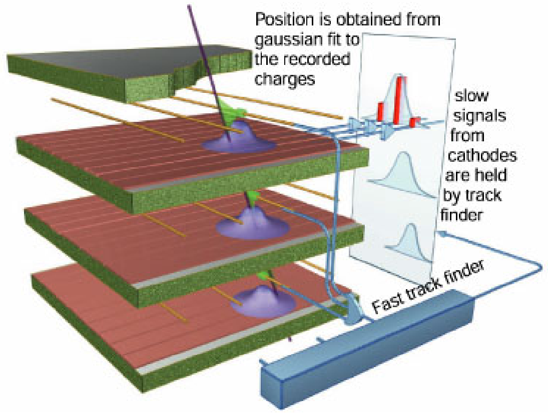

These detectors are used in the endcaps, where the magnetic field is intense and very inhomogeneous which would render DTs useless. CSCs are multiwire proportional chambers, where one cathode plane is segmented into strips running across the wires. 2 coordinates can be extracted from detector simultaneously, as the signal induced by the ionizing muon is transfered to the wire and to the perpendicular strips, by movement of the ions in the electric field.

2.4.3 Resistive Plate Chambers

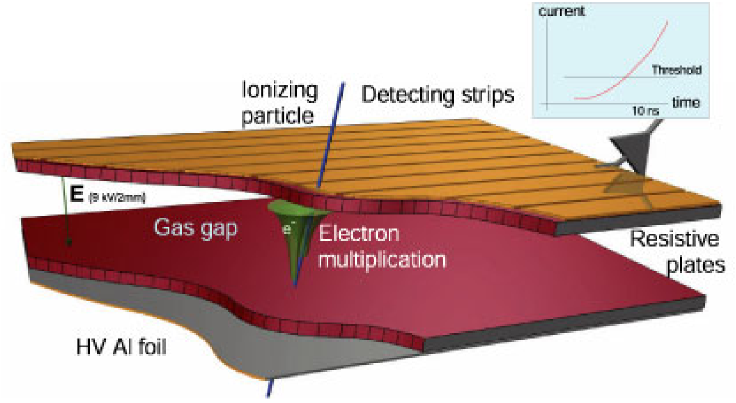

Providing fast trigger information is the task of these gaseous detectors. The time resolution is in the order of 1ns, comparable to fast scintillators. They are distributed over the barrel and the endcaps.

The RPC consists of two parallel plates made of a high resistive plastic material. This allows the construction and operation of very large and thin detectors that can operate at a high rate and with a high gas gain without developing streamers or catastrophic sparks.

The electric field inside is uniform. Electrons generated by the ionizing particle experience multiplication when traveling to the positively charged resistive plate. A proper threshold setting allows the detection of a signal dominated by the electrons generated near the cathode. The threshold setting determines to a large extent the time delay of the pulse, the time resolution and also the efficiency. With a proper choice of the resistivity and plate thickness, the rate capability can reach several thousand Hertz per cm^2.

As the plastic material is transparent to the electric signal generated by the electron avalanches, it is picked up by external metal strips.

3 The Silicon Strip Detector

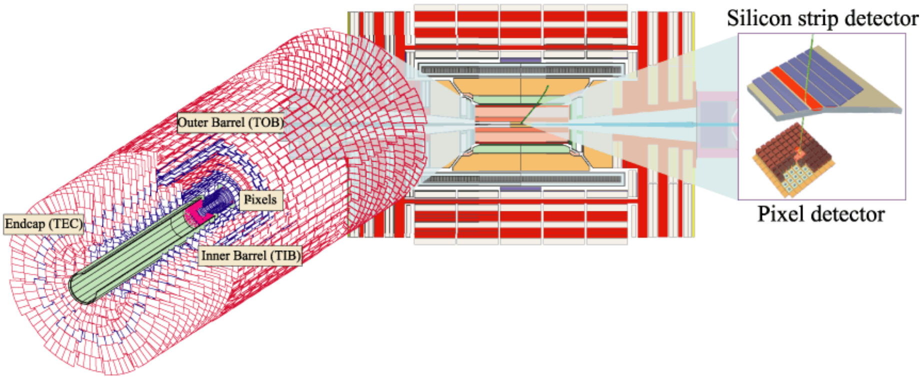

To get a better understanding of the design choices the tracker collaboration made when settling the specifications of the microstrip tracker, it is essential to grasp the concept of a silicon detector device.

The harsh radiation environment in the tracker region is a major challenge to overcome, so some basic introduction on radiation damage on silicon detectors is given as well in this chapter.

After covering the most important aspects of semiconductor detectors in general, a closer look on the design choices of the CMS tracker collaboration will be provided. This is all done from a pre-manufacturing viewpoint. Some problems that were only encountered when the design phase was long concluded and manufacturing has begun, will be discussed in subsequent chapters.

3.1 A Si Detector in Principle

At first, it is necessary to take a closer look on how the actual detection process inside the silicon is working. We will see what happens to ionizing particles in matter generally and how this can be used to generate signals carrying information on the incident particle.

3.1.1 Energy Loss

When particles are traversing matter, various effects can occur like Cherenkov radiation, nuclear reactions or, most importantly, ionization. An effect widely used in detectors is ionization. At high energies, the deflection the incident particles experiences is low and the created signal can be amplified and recorded quite easily. The drawback is, that only electrically charged particles can cause ionization.

The charged particles electric field causes the atoms inside the traversed matter to be stripped of some or more of their electrons. These free electrons are then available for signal detection after proper amplification. The energy loss in matter was first described by H. A. Bethe and F. Bloch [4]:

$$-\frac{dE}{dx} = Kz^2\frac{Z}{A}\frac{1}{\beta^2}\left[\frac{1}{2}ln\frac{2m_ec^2\beta^2\gamma^2T_{max}}{I^2} - \beta^2 - \frac{\delta}{2}\right], \tag{5}$$

where the variables are explained in table 3.1.1.

Symbol	Definition	Units or Value
A	Atomic mass of medium	gmol^{-1}
β	particle velocity $\frac{v}{c}$	
c	speed of light	299,792,458 ms^{-}1
δ	Density effect correction to ioniziation energy loss	
ϵ_0	permittivity of free space	$8.854187817 \times 10^{-12}$ Fm^{-1}
E	incident particle energy $\gamma M c^2$	MeV
γ	$(1-\beta^2)^{-\frac{1}{2}}$	
I	Mean excitation energy	eV
K	$4\pi N_A r_e^2 m_e c^2$	0.307075 MeVcm^{-2}mol^{-1}
m_e	Electron mass	$9.10938188(72) \times 10^{-31}$ kg
N_A	Avogadro's number	$6.02214199(47) \times 10^{23}$ mol^{1}
r_e	classical electron radius $\frac{e^2}{4\pi\epsilon_0 m_e c^2}$	2.817940285(31) fm
T_{max}	maximum kinetic energy transfer to a free electron	
T_{cut}	kinetic energy transfer cut for restricted energy loss formula	
z	Atomic mass of particle	
Z	Atomic mass of medium	

Table 2: List of variables used in the energy loss equations.

At lower energies a $\frac{c}{z}$ correction term is necessary for tightly bound atomic electrons and at higher energies (which are much more relevant for CMS) radiative effects begin to be important.

Fig. 11 shows the stopping power calculated for some elements. Relativistic particles having energy loss rates close to the minimum are called *Minimum Ionizing Particles* (MIPs).

But it is important to note, that most detectors measure the mean energy *deposited* in the material and not the whole energy *lost* by the particle. This happens due to high energy knock-on electrons which carry a certain amount of energy out of the active detector material. Of course, this is especially true for thin (typically a few 100 μm) semiconducting detectors. The *restricted energy loss rate for relativistic ionizing particles* leads to:

$$-\left.\frac{dE}{dx}\right|_{T<T_{cut}} = K z^2 \frac{Z}{A} \frac{1}{\beta^2} \left[\frac{1}{2} ln \frac{2 m_e c^2 \beta^2 \gamma^2 T_{max}}{I^2} - \frac{\beta^2}{2} \left(1 + \frac{T_{upper}}{T_{max}} \right) - \frac{\delta}{2} \right], \quad (6)$$

where $T_{upper} = MIN(T_{cut}, T_{max})$.

3.1.2 Charge Collection

Now that we have seen how charged particles deposit their kinetic energy due to ionization of the material, we have to think of a way to collect and measure the produced charge. Simply applying an electrical field across the material should transport the created electron-hole pairs to their respective electrodes, but does this produce a reasonable *Signal-to-Noise*(S/N) ratio?

The number of charged carriers is the quotient of the total energy loss E_{loss} of the incident particle and the energy necessary for electron-hole pair production E_{eh}:

$$n = \frac{E_{loss}}{E_{eh}} \quad (7)$$

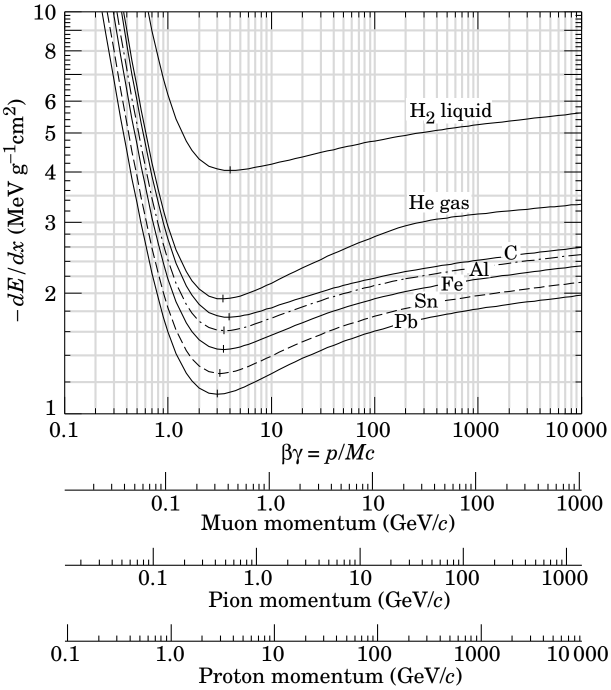

Figure 11: Energy loss rates in several different absorber materials.

In silicon E_{eh} is around 3.6 eV which comprises not only the band gap but some other excitations like phonons as well. When a MIP traverses silicon of 300 μm thickness, the total energy loss is ≈80keV which gives us ≈22000 electron hole pairs.

The intrinsic charge carriers in silicon are of the order $p = n = n_i \approx 10^{10} cm^{-3}$. Comparing this to the charge yield of a MIP shows, that the chances of extracting a signal are merely non existent with such a devastating S/N ratio.

To get rid of the intrinsic charge carriers inside the silicon, we introduce a simple *pn-junction* like a diode. By applying a reverse bias voltage, the area around the junction gets free of the excess charge carriers (see fig. 12). This way, there are almost no intrinsic charge carriers left in the depleted zone. A particle ionizing the area is then the only source of free charge carriers in that region. The S/N ratio is now at reasonable values and we can measure the generated charge by the current induced when they drift towards the electrodes. The current is proportional to the sum of both carrier velocities which are different for holes and electrons:

$$j = \frac{e}{D}\left(\sum v_e + \sum v_h\right) \qquad (8)$$

where,

e . . . elementary charge
D . . . detector thickness
v_e . . . drift velocity for electrons
v_h . . . drift velocity for holes

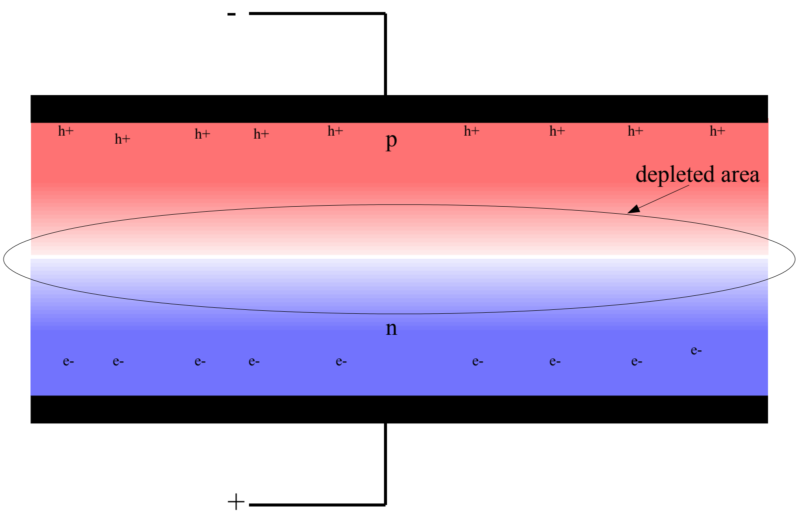

Figure 12: By applying a reverse bias voltage, charge carriers are transported away from the junction towards their respective electrodes.The size of the depleted area depends on the reverse bias voltage.

The integrated current gives the total collected charge, which can be amplified and measured by appropriately selected devices:

$$Q_c = \frac{e}{D} \int (\sum v_e + \sum v_h) dt. \tag{9}$$

3.2 Radiation Damage

The effects of radiation on silicon detectors have to be carefully evaluated to ensure proper operation over the full length of the experiment's expected duration. Today, most effects are only partly understood. We have to rely on careful evaluation of radiation experiments and parametrization of the resulting effects, without a complete understanding about the physical background.

Still, the research findings look promising and we can be quite optimistic on whether silicon detectors will endure the full period of many years of detector operation without loosing too much of their important characteristics.

As the tracker is situated very close to the main interaction point in the beam pipe, radiation hardness is a very essential feature of its design. But it is not only the sensitive silicon detectors that have to withstand the challenging conditions, but also the electronics that are situated on the modules and therefore inside the radiation environment.

The silicon detectors have to endure a large variety of radiation, which, for simplicity, we are going to divide into two types:

- Charged Particles (protons, pions, electrons,...)
- Neutral Particles (neutrons)

Neutral particles such as neutrons, interact by scattering elastically with the semiconductor nucleus, while charged particles like protons or electrons scatter by electrostatic interaction as well. The mass of the scattering particle is also important, because it limits the maximum energy that can be transferred from the impinging radiation. Therefor electrons for example, hardly ever transfer enough energy to create lattice defects, but they are ionizing the area they are passing.

In table 3.2 some important characteristics of the primary interactions of radiation are given. The concepts of point and cluster defects will be clarified later. Fig. 13 shows the non ionizing energy loss for different particle energies. The comparison of fluences of different particles is the *hardness factor* κ according to [3]:

$$\Phi_{eq}^{1MeV} = \kappa\Phi \tag{10}$$

where κ is defined as:

$$\kappa = \frac{EDK}{EDK(1MeV)} \tag{11}$$

with EDK the *E̲nergy spectrum averaged D̲isplacement K̲ERMA*[5]

$$EDK = \frac{\int D(E)\Phi(E)dE}{\int \Phi(E)dE} \tag{12}$$

where $\Phi(E)$ is the differential flux and

$$D(E) = \sum_k \sigma_k(E) \int dE_R f_k(E, E_R) P(E_R) \tag{13}$$

the displacement KERMA or the damage function for the energy E of the incident particle, σ_k the cross section for reaction k, $f_k(E, E_R)$ the probability of the incident particle to produce a recoil of energy E_R in reaction k and $P(E_R)$ the partition function (the part of the recoil energy deposited in displacements). $EDK(1MeV)$=95 MeVmb. The integration is done over the whole energy range.

3.2.1 Bulk and Surface Damage

In this chapter we are going to investigate the effects of the two types of radiation (neutral and charged particles) on the semiconductor grid and the insulating oxide layer. As we have learned from the preceding chapter, the interaction depends on whether the particles are charged or not and on their mass.

The actual detection process occurs in the depleted silicon zone. Imperfections in the silicon crystal lattice structure, would influence the detector properties, generally to the worse. Defects created by impinging radiation which dislocates silicon atoms from their lattice site are the main concern in this area. As said before, heavy particles scatter with the silicon nucleus and transfer kinetic energy to it. If the energy transferred exceeds about 15 eV, a dislocation of a lattice atom is possible. To be more specific, at a recoil energy of about 25eV, the probability of displacement is roughly one half (for silicon).

---

[5] K̲inetic E̲nergie R̲eleased per unit M̲A̲ss is the sum of the initial kinetic energies of all the charged particles liberated by uncharged ionizing radiation (neutrons and photons) in a sample of matter, divided by the mass of the sample. It's measured in Grays.

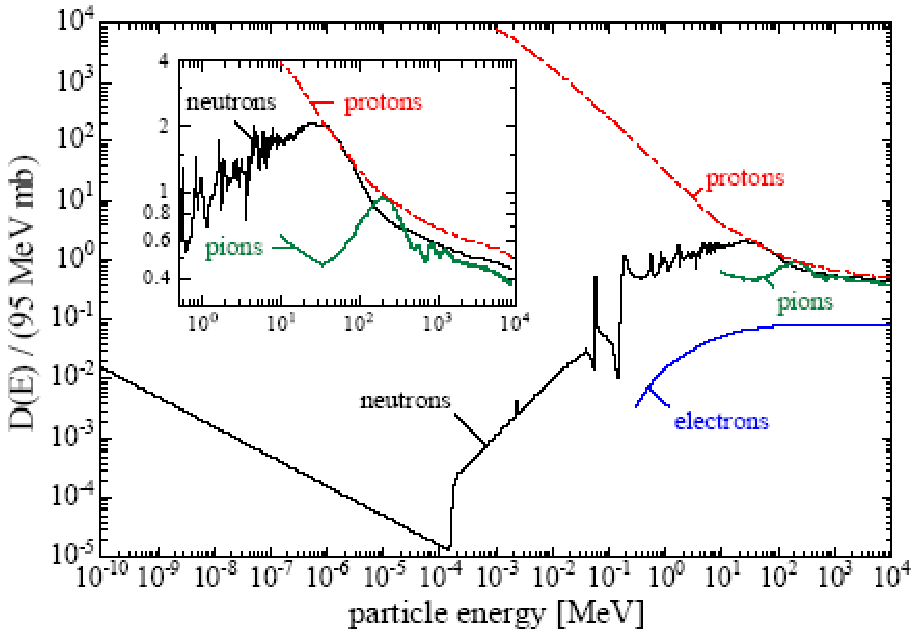

Figure 13: Non ionizing energy loss of different particles. The cross sections are normalized for 1 MeV neutrons with *equivalent fluence* Φ_{eq}

Radiation	Electrons	Protons	Neutrons	Si^{+}
Interaction	Coulomb scattering	Coulomb and nuclear scattering	Elastic nuclear scattering	Coulomb scattering
$T_{max}[eV]$	155	133,700	133,900	1,000,000
$T_{av}[eV]$	46	210	50,000	265
$E_{min}[eV]$				
point defect	260,00	190	190	25
defect cluster	4,600,000	15,000	15,000	2,000

Table 3: Characteristics of interaction of radiation with silicon and of primary knock-on atoms. The radiation energy is 1 MeV, T_{max} is the maximum kinematically possible recoil energy, T_{av} the mean recoil energy and E_{min} the minimum radiation energy needed for the creation of a point defect and for a defect cluster.

Recoil energies below roughly 1-2 keV create only isolated point defects, between 2 keV and 12 keV the energy is high enough to create one defect cluster and additional point defects and above 12 keV several clusters and additional point defects will be produced. A cluster is a dense agglomeration of point defects that appear at the end of a recoil silicon track where the atom looses its last 5-10 keV of energy and the elastic scattering cross-section increases by several orders of magnitude.

In the insulating oxide layer which separates the p-type silicon from the aluminium read-out strips, the situation is different. The structure is already highly irregular, therefor the interaction of radiation with the nucleus can be safely ignored. The additional damage to the oxide structure will not alter the properties of that region.

Much more important is the ionization by charged particles, as well as by photons. One may consider the oxide as a region with a high density of defects whose charge state can be altered by irradiation. New electrons and holes are created in the SiO_2 layer. The electron mobility is several orders of magnitude larger than that of holes. Compared with holes, radiation-generated electrons will diffuse out of the insulator in relatively short time and the capture of holes is the dominant process that changes the oxide's properties.Radiation damage of oxide therefor manifests itself as a buildup of positive charge due to semipermanent trapped holes, which is sensed in a shift in the flat-band voltage.

3.2.2 Changes in Properties due to Defect Complexes

The defects in detector bulk material are still mobile at room temperature. Part of those defects will even vanish either by an interstitial filling a vacancy or by diffusing out of the surface. They may however also become stable by interacting with another radiation induced defect, or with an imperfection from the crystal growth process. Let's have a look on the effects and changes in detector properties that are caused by these stable defects. Before going into depth, it is worth mentioning that these defects can have one of the following main consequences:

- Alterations of charge density in the space-charge region
- Formation of recombination-generation centers
- Formation of trapping centers

Alterations of Charge Density in the Space-Charge Region The original dopants such as phosphorus or boron may be captured into new defect complexes, thereby loosing their original function as flat donors or acceptors. They may assume a charge state different from the original one. This will change the effective doping of the semiconductor. In fig. 14 the fluence dependence of the effective doping of an originally n-type silicon can be seen. The dashed lines correspond to the parameterisation of that effect. At a certain fluence, the silicon even changes it's doping state from n-type to effectively p-type. This effect is called *Type Inversion*.

$$N_{eff}(\Phi) = N_{D,0}e^{a\Phi} - N_{A,0} - b\Phi \tag{14}$$

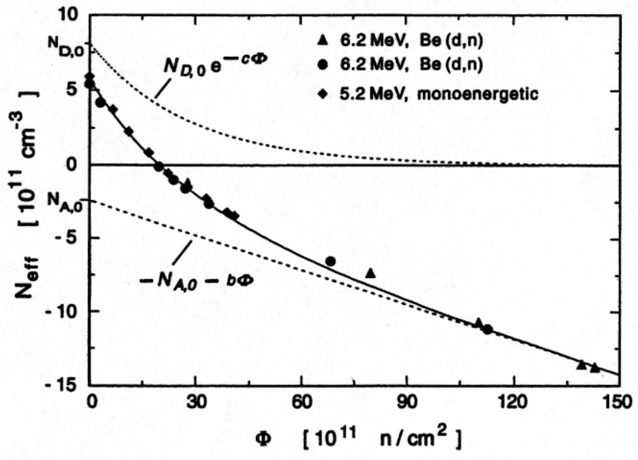

Figure 14: Fluence dependence and parameterization of the effective doping according to equation 14 for an n-type silicon wafer irradiated with neutrons [2]. The data has been corrected for self-annealing occurring during the extended irradiation period. (Caution: Fluence $\doteq$ Integrated Flux)

with $N_{D,0}, N_{A,0}$ donator and acceptor concentration before irradiation and a,b constants to be determined experimentally. These material independent damage parameters have been determined as a=3.54 $\times$ 10^{-13} cm^2± 4.5% and b=7.94 $\times$ 10^{-2} cm^{-1}±8.0%

As a consequence of the alteration in space charge configuration, the operating voltage of the detector changes.

Recombination-Generation Centers These defects can capture and emit electrons or holes. Therefor the volume-generated leakage current is raised. The leakage current as a function of the 1 MeV neutron equivalent fluence is shown in fig. 15. A linear relationship between current and fluence is found. For fluences above type inversion, a stronger rise is observed. It can be parameterized as:

$$\frac{\Delta I_{vol}}{V} = \alpha\Phi, \tag{15}$$

where α is usually:

$$\alpha = (3.99 \pm 0.03) \times 10^{-17} A/cm. \tag{16}$$

Trapping Centers Another problem is the trapping of an electron/hole and remission a short time afterwards. The charge is released too late to contribute to the detection signal. Therefor the signal is smaller while more noise is produced resulting in an reduced S/N ratio.

As with the present knowledge on detector physics, it is not possible to explain these effects in all detail, we have to restrict ourselves to global parameterization of the fluence dependence of the trapping time which will result to:

$$\frac{1}{\tau_t} = \frac{1}{\tau_{t0}} + \gamma\Phi \tag{17}$$

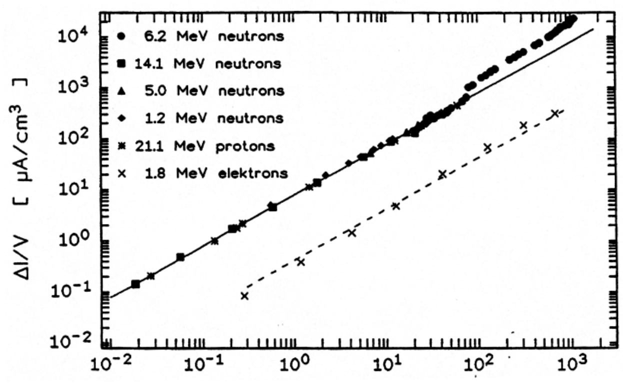

Figure 15: A 1MeV neutron equivalent fluence dependence and parameterization of the volume-generated current for an n-type silicon wafer irradiated with neutrons [2]. The data has been corrected for self-annealing occurring during the extended irradiation period. (Caution: Fluence $\doteq$ Integrated Flux)

where τ_t is the average time a hole/electron stays trapped and τ_{t0} is the value before radiation. This parameterization works well for hole and electron trapping at moderate fluence. A value of $\gamma \approx 0.24 \times 10^{-6}$ cm^{2}s^{-1} is found

For electrons at high fluences, a steeper increase of trapping probalility was observed (see fig. 16).

3.2.3 Annealing

Observing a radiation-damaged detector after an extended period of radiation exposure, one notices that the resulted damage diminishes with time. This effect is called *annealing*. The rate of damage decrease is strongly dependent on temperature.

This effect can be (naively) interpreted as diffusion of radiation induced crystal defects out of the detector bulk and most importantly, by the recombination of vacancies and interstitials. Still, one must keep in mind that annealing is a rather complicated process involving many different and only partially understood interactions between defects and defect complexes.

In fig. 17 annealing of radiation induced change of effective doping is shown over an extended period of time at constant room temperature (20°C). One may notice an inversion of the annealing effect on the time scale of months.

3.2.4 Reverse Annealing

The inversion of the annealing process is called *reverse annealing*. The effective doping of irradiated silicon detectors after the initial decrease, is increasing again after a few weeks of room temperature annealing. This surprising new effect can be explained as the transformation of radiation-induced electrically inactive defect complexes into electrically active ones. Reverse annealing is also strongly temperature dependent. Below approximately 0°C the process is almost completely suppressed.

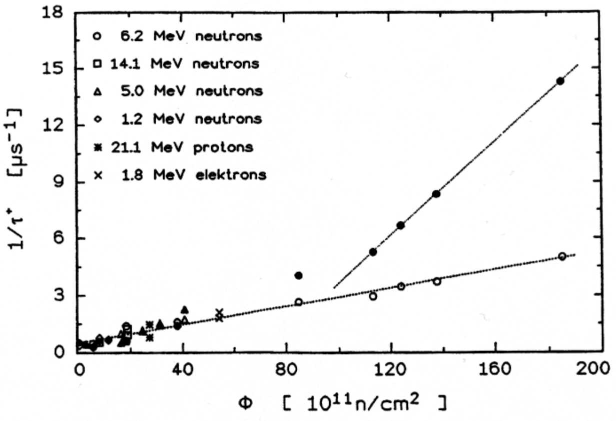

Figure 16: A 1MeV neutron equivalent fluence dependence and parameterization of the inverse trapping-time constant for holes *(open symbols)* and electrons *(solid symbols)* for an n-type silicon wafer irradiated with neutrons [2]. (Caution: Fluence $\doteq$ Integrated Flux)

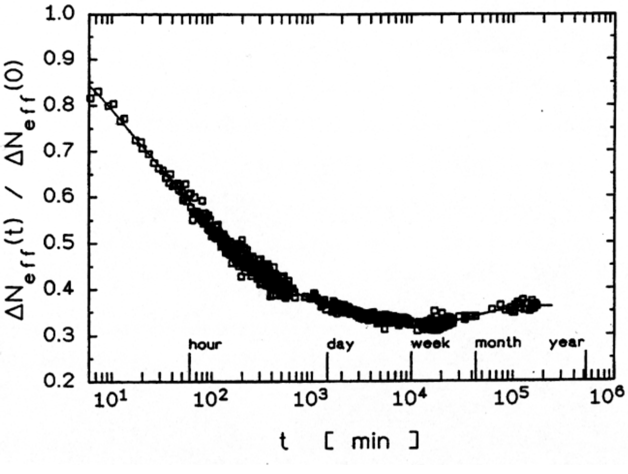

Figure 17: Room temperature annealing of radiation-induced change of effective doping [2]. Data are corrected so as to correspond to a short irradiation followed by a long-term observation at constant (20°C) temperature. Observed is a decrease on the time scale of weeks (annealing) followed by a rise (reverse annealing) on the time scale of months.

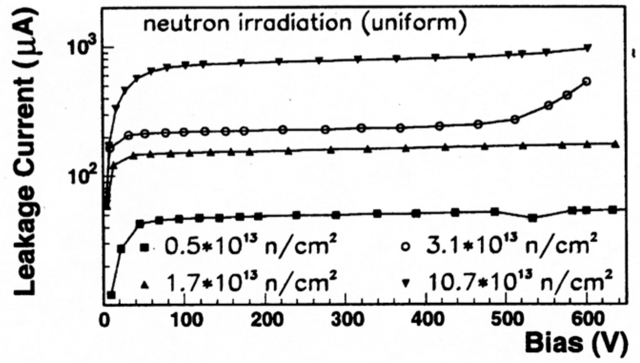

Figure 18: I - V curves for 3 × 6 cm^2 devices after uniform neutron irradiation, for Hamamatsu detectors, at -10°C temperature.

3.2.5 Test Results for the CMS Experiment at LHC

The figures show selected results from [2]. They are laboratory measurements and beam tests of heavily irradiated microstrip silicon detectors. They should offer further insights on the performance of irradiated silicon detectors and are only printed here without any further discussion.

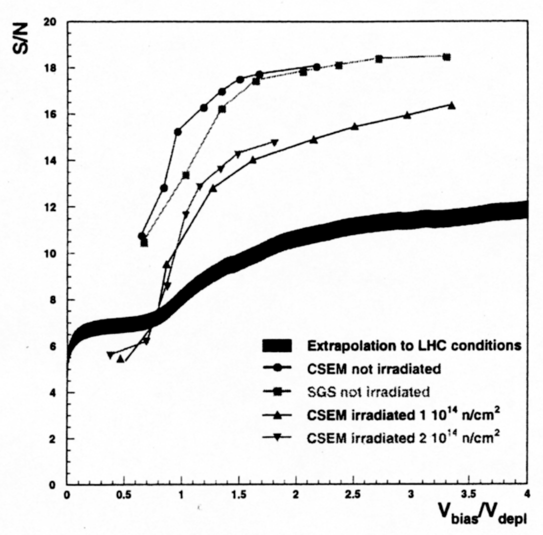

Figure 19: Signal-to-noise ratio as a function of bias voltage in over-depletion units, for two non-irradiated detectors (CSEM,SGS), and two detectors (CSEM) irradiated at 1×10^{14} n/cm^2 and 2×10^{14} n/cm^2 respectively. The readout pitch is 50 μm, the strip length is 12,5 cm. The operating temperature is -10°C. The thick band is an analytical extrapolation to the experimental conditions foreseen at the LHC.

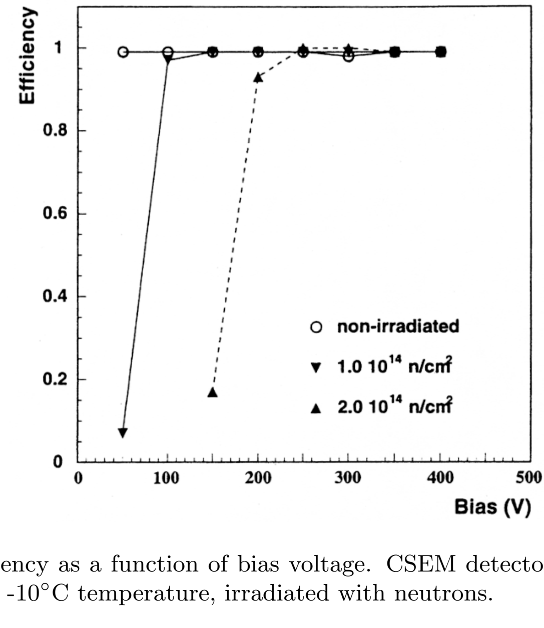

Figure 20: Efficiency as a function of bias voltage. CSEM detectors of 75 μm pitch, 11 cm length, at -10°C temperature, irradiated with neutrons.

type	length [mm]	height [mm]	pitch [μm]	strips	quantity
IB1	63.3	119.0	80	768	1536
IB2	63.3	119.0	120	512	1188
OB1	96.4	94.4	122	768	3360
OB2	96.4	94.4	183	512	7056
W1 TEC	64.1-87.9	87.2	81-112	768	288
W1 TID	64.6-93.8	112.9	80.5-119	768	288
W2	88.1-112.2	90.2	113-143	768	864
W3	64.9-83.0	112.7	123-158	512	880
W4	59.7-73.2	117.2	113-139	512	1008
W5a	98.9-112.3	84.0	126-142	768	1440
W5b	112.5-122.8	66.0	143-156	768	1440
W6a	86.1-97.4	99.0	163-185	512	1008
W6b	97.5-107.5	87.8	185-205	512	1008
W7a	74.0-82.9	109.8	140-156	512	1440
W7b	82.9-90.8	98.8	156-172	512	1440

Table 4: Geometrical dimensions of the strip sensors. The thin sensors of the *Inner Barrel* (IB) and the thick sensors of the *Outer Barrel* (OB) are rectangular. The sensors of the *Tracker EndCaps* (TEC) and the *Tracker Inner Disk* are wedge-shaped (W1-W7).

3.3 The Si Strip Detector at CMS

After reviewing the basics about silicon detector and the problems arising due to the high radiation environment, the actual design choices for the CMS silicon microstrip detector are discussed in this chapter. First we will see the layout of the silicon itself and how it is prepared to meet the various challenges. Then we will introduce various components that are gathered around the silicon to form the full featured detector modules which are used in the tracker.

3.3.1 Silicon Sensor Design

Various different layouts have been designed to suit the geometrical boundaries in the various regions of tracker. Table 4 shows some data on the different silicon layouts and fig. 21 shows their location in the tracker.

Nevertheless, all of them share common features which are only adapted to suit the various locations. The bulk material is 320 μm or 500 μm thick, high resistivity, n-type phosphorus doped *<111>*[6] *silicon.* For the inner region, 320 μm is a good compromise between S/N ratio and depletion voltage, while ensuring good mechanical stability and production yield. Nevertheless, the thick 500 μm sensors are used in the outer regions, to compensate the increase in noise due to long strips with a gain in signal.

The backplane is made of *n^+ doped material*, while the strips are made of p^+. The strips are *capacitively coupled* to aluminium readout strips located above

---

[6] This parameter describes the crystal orientation of the silicon. <100> is usually the common configuration resembling simple cubes, while the <111> configuration used for the tracker is still cubelike of course, but they are "standing" on one corner

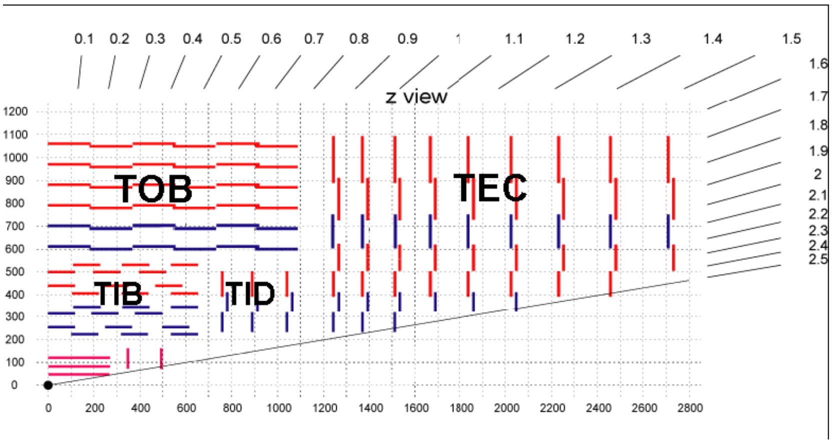

Figure 21: View of the CMS Tracker. Pixel layers are shown in pink, layers containing microstrip sensors are shown in red (single sided) and blue (double-sided).

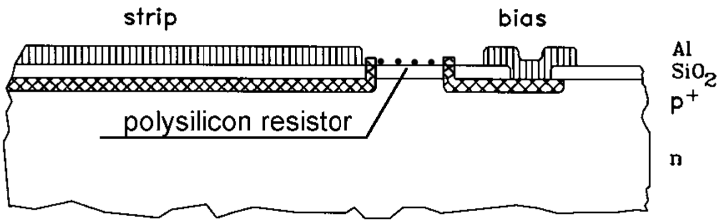

Figure 22: A cut along the strips. The bias ring is connected to the strips via a polysilicon restistor of a few MΩ.

them with a little *metal overhang* and separated by the isolating silicon-oxide (SiO_2) layer. Fig. 23 shows a sketch of the composition.

The strips are surrounded by the bias ring, which is applying the voltage (ground level in this case) to the strips via a *polysilicon resistor* see fig 22. The *guard ring* is a floating p^+ implanted ring surrounding the whole structure including the bias ring. The photo of the edge of a silicon sensor in fig. 24 shows all the basic structures very nicely.

Design choices - why made:

<111> type silicon was used to reduce surface charges. By using this orientation, one can minimize the number of dangling bonds on the surface of the silicon. See fig. 25 for a graphical explanation.

n^+ doped material for the backplane was used to have a device that is capable of working after type inversion. Before type inversion it additionally reduces the leakage current.

Capacitively coupled readout strips are used to get rid of the leakage current running on the implanted strips. This makes it easier for the pre-amps in the readout chips to get a proper signal.

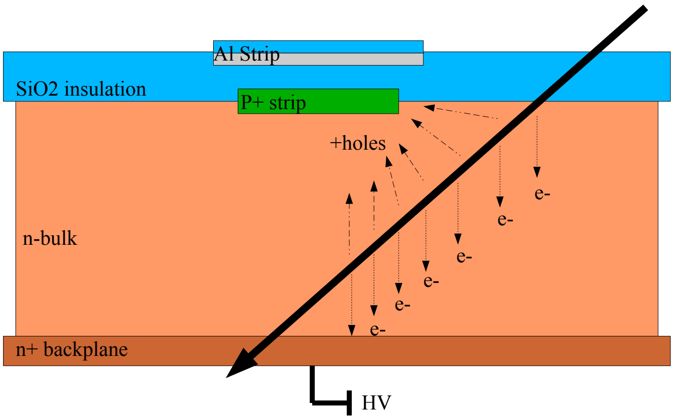

Figure 23: Layout of the silicon detector seen from a cut perpendicular to the strips. For simplicity only one strip is shown here. The implanted p^+ strips are grounded and therefore have a negative potential compared to the backplane. This is the situation *before* type inversion!

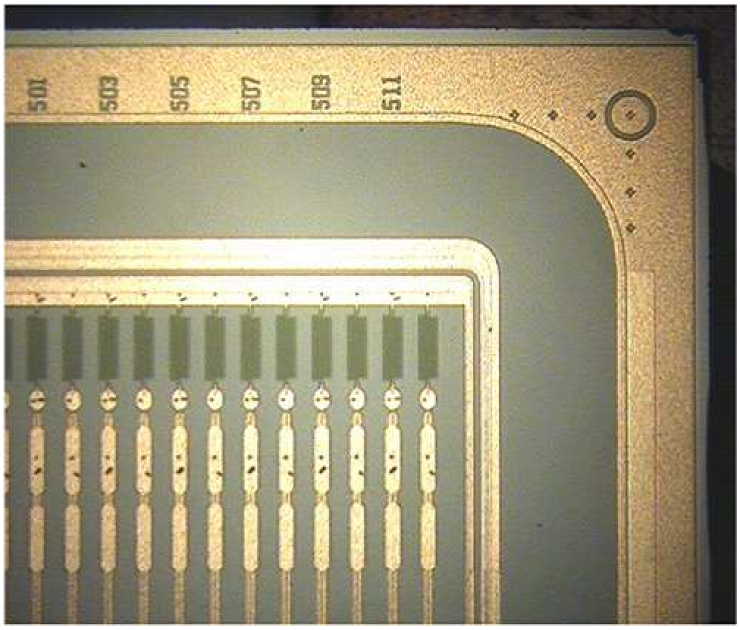

Figure 24: The edge of a sensor.

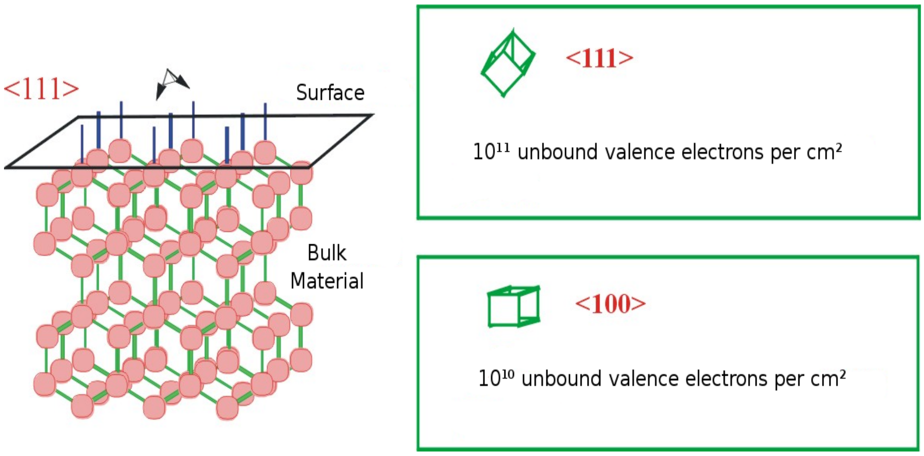

Figure 25: Dangling bonds in a <111> configuration.

The metal overhang extends the field lines a little beyond the region the implant itself would reach. This ensures a flatter, continuous potential drop.

Polysilicon resistors are deposited between the bias ring and each strip, to put the implant at the desired potential.

The guard ring is limiting the sensor to the cut edges. It protects the active sensor area from influences of the borders.

3.3.2 Detector Module Layout

The silicon sensors are integrated into modules, serving not only as a stabilizing and handling frame, but already containing some readout functionality. These components have to be situated as near as possible to the detector to ensure proper signal processing.

As already discussed previously, there are a number of different detector geometries for the various locations inside the the tracker. This is reflected in the module designs. Let aside the different geometries, there are modules with one or two sensors, 512 or 768 channels (which affects the number of readout chips, either being four or six) and normal and stereo ones. Nevertheless, all of the modules share the same basic components (see fig. 26):

The carbon frame serves as the support structure for all the components, and is equipped with various mounting holes for assembling them into larger structures. The used carbon material ensures some of the most important considerations for a support structure:

- Low mass to minimize any unintentional interactions with particles.
- High mechanical stability despite their low weight to ensure the robustness of the modules themselves and the tracker on the whole.

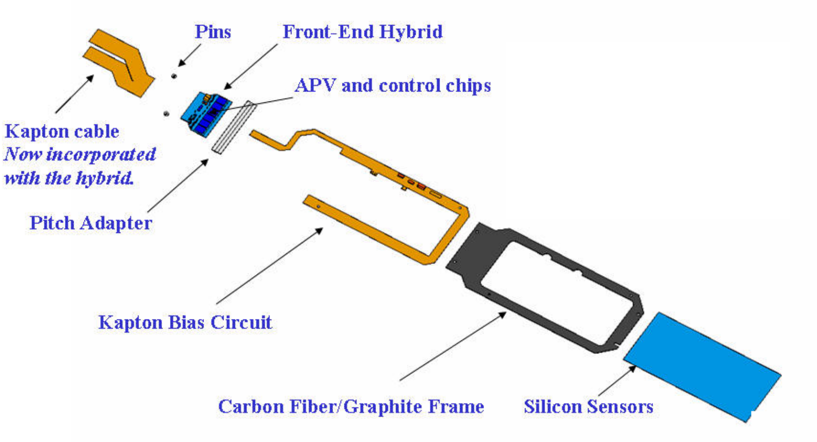

Figure 26: Basic components of a CMS Tracker Module.

- Having a *Thermal Expansion Coefficient* (CTE) similar to silicon is important, as a temperature variation between assembly and operation of up to 40°C is expected[7]
- Radiation hardness is a requirement essential for all the components located inside the tracker. The used carbon material is inert to radiation for the most part.

Kapton bias circuitry is necessary to distribute the HV to the sensor backplane. Some additional components ensure the stability of the bias voltage and two thermistors provide temperature feedback of the module.

The hybrid

is an integrated component itself. It houses all the readout electronics for the module on a small board:

---

[7] For testing purposes even higher temperature variations have been exerted on the modules up to 70°C without any difficulties. The reason for this ”beyond specs”’ procedure, was to test the glued backplane-kapton connection which showed some deficiencies during early production stages.

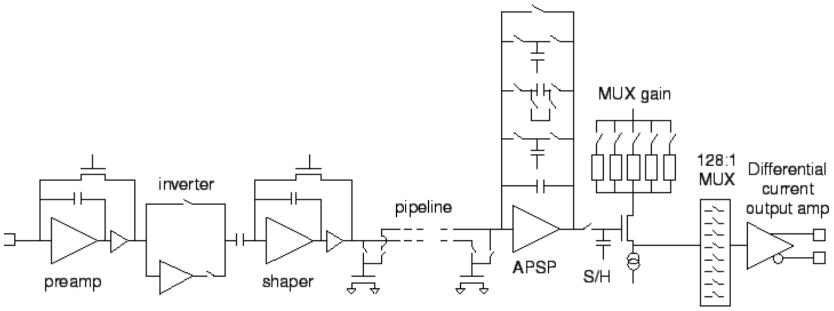

Figure 27: Block diagram of the APV readout chip. The schematics to the left of the 128:1 multiplexer (MUX) is implemented individually for each of the 128 channels.

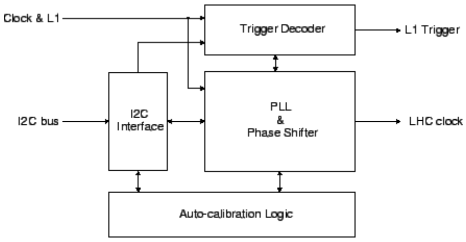

Figure 28: Block diagram of the PLL-Delay chip.

The *P̲itch A̲dapter* (PA) connects the input stage of the on-modul readout electronics with the aluminium strips on the detector. This is necessary, as the pitch of the input channels on the chips (43 μm) is generally much smaller than on the silicon(61-254 μm). The PA is adapting the different silicon geometries to the hybrids. It is made of a glass substrate with 1.5 μm aluminium strips including bonding pads on each end.

The *A̲nalog P̲ipeline V̲oltage* (APV) is the main readout chip. It is directly coupled to the aluminium strips on the detector via the PA. The APV chip series was designed as a front-end amplifier for the tracker and is manufactured in the radiation hard 0.25 μm IBM Deep Submicron CMOS process. The design includes a preamp, an inverter, a shaper, a 192 cell pipeline, and a deconvolution filter for each channel as well as a 128:1 multiplexer with an differential output amp (see fig. 27).

The APVMUX is a set of fast switches. It is able to multiplex the output of an APV pair together into a single output line. An I^{2}C interface is used to program the chip.

The *P̲hase L̲ocked L̲oop* (PLL) has to provide clock and trigger signals with an adjustable delay. As both signals are transmitted via the same line, the PLL is responsible to decode both signals. A trigger is actually encoded into the 40 Mhz CMS clock as a missing clock pulse. Additionally a clock phase shifter is implemented as well. It is adjustable in 24 1.04 ns taps within one clock cycle. An I^{2}C interface is used to program the chip (see fig. 28).

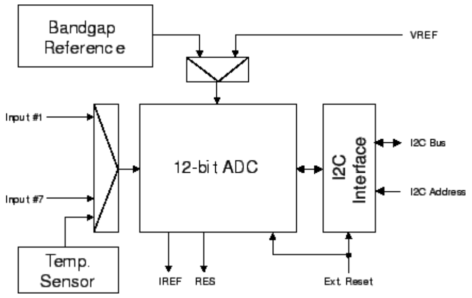

Figure 29: Block diagram of the DCU.

The *Detector Control Unit* (DCU) is monitoring low voltages (1.25 V and 2.5 V), leakage current and temperatures (see fig. 29 for a block diagram). The temperature is measured inside the DCU and with an external thermistor on the kapton bias circuitry. The chip can be programmed and red out via an I^2C interface.

The Rigidifier should provide additional stability to the silicon. It should protect the sensor from mechanical stress during the post assembly test phase and during the assembly into larger structures.

4 Quality Assurance Scheme

The completed tracker will house ≈15000 detector modules, all of them being very delicate pieces of hardware built out of various sub components. To make sure that the components meet the specifications, and to monitor and debug the assembly process, a well though over *Quality Assurance* (QA) program had to be developed.

Two programs used to monitor the silicon detectors and the assembled modules were introduced at the *Institut für HochEnergiePHYsik* (HEPHY) in vienna[8]. Both programs will be discussed in separate chapters.

To support the QA program and record all the test results a specialised database has been installed.

4.1 The CMS Tracker Database

When dealing with such a high number of parts, which are produced, tested and assembled in various different locations around the world[9], it is essential to collect all the data recorded on each part, to provide the data to all institutes and even to simply track the location of every part. This made the development and maintenance of a central database inevitable.

The CMS Tracker *DataBase* (TrackerDB) is located at the *Centre National de la Recherche Scientifique* (CNRS) in Lyon. It is implemented in Oracle 10i offering a SQL interface. Several different *User Interfaces* (UIs) where developed to retrieve and enter data into the TrackerDB. Some of the most interesting UIs are:

Name	Link & Features
BigBrowser	http://cmsdoc.cern.ch/~cmstrkdb/
	Main Interface to the TrackerDB. Feeding all assembly and testing data into the DB
VisualDB	http://wwwhephy.oeaw.ac.at/u3w/e/ewidl/www/visualdb/visualDB.html
	Printing nice histograms of sensor data
trkNavigator	http://hep.fi.infn.it/CMS/testres/trkNavigator/
	Retrieve module, sensor and hybrid data from the TrackerDB
Module Production DB Browser	http://cms.ct.infn.it/modprod/
	Web interface to monitor the module production status
relay.pl	http://wwwhephy.oeaw.ac.at/u3w/b/bergi/www/relay/
	PERL script to retrieve any data from the TrackerDB
queryDB.py	http://risoldi.home.cern.ch/risoldi/filesdocs/pythonDB/
	Phyton script to retrieve any data from the TrackerDB

---

[8] Institut für Hochenergiephysik, Nikolsdorfergasse 18, A-1040 Wien

[9] This is not an exaggeration! The tracker collaboration does not only include European institutes but also the USA are contributing some major parts and Japan's Hamamatsu corporation is one of the two major suppliers of the silicon sensors. Even Pakistan is involved in the Tracker project, as they are deliving the module frames.

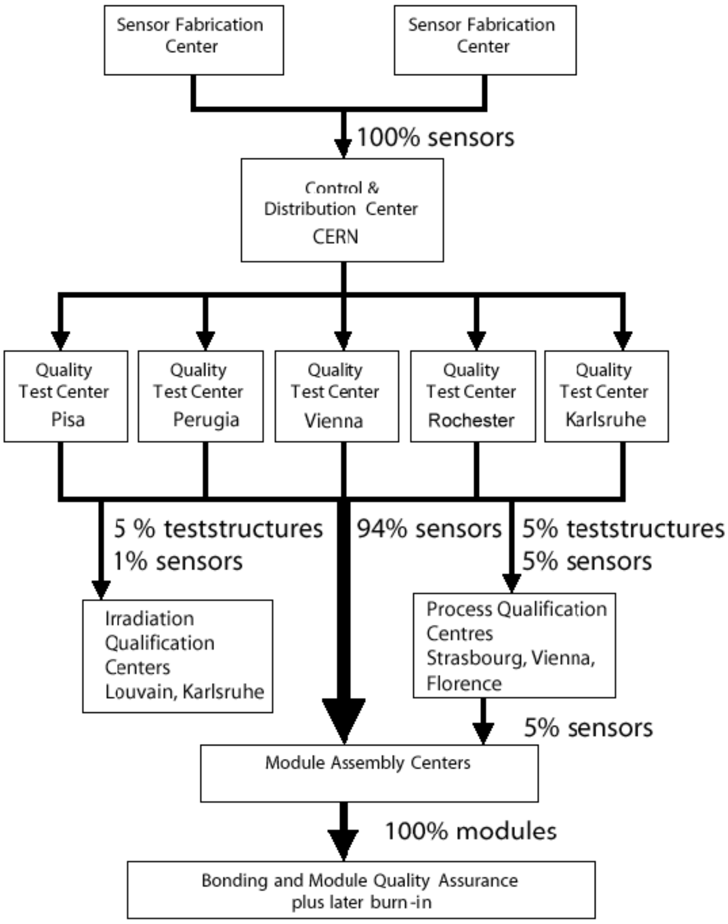

Figure 30: Sensor quality assurance plan. Apparently, sensors are shipped among different laboratories quite often.

4.2 Sensors

The silicon sensors, the *heart* of the detector, is manufactured by two companies: Hamamatsu, Japan and STMicroelectronics, Italy. Both companies are entitled to already run certain tests on the sensors, to characterize important parameters. This should make sure that already 98% of the delivered sensors will be accepted by the tracker collaboration in the subsequent tests. The test sequence can be seen in fig. 30 The QA scheme foresees three different stages: quality, process and irradiation tests. Not all sensors are subjected to each of the tests, as this would unnecessarily lengthen the test duration.

Not only the sensors are subjected to tests, but the wafers containing the sensors have been outfitted with teststructures, which are used for certain tests, as will be described later.

The sensor flow according to the QA plan in fig. 30:

- Each sensor is tested at the manufacturer to make sure that it is within specs. The data is later fed to the TrackerDB and the sensors are shipped to CERN for registration in the TrackerDB and distribution to the *Quality Test Centers* (QTC).

- The 5 QTCs will then conduct a full characterization on a small percentage of sensors. Again, all the data will be fed to the TrackerDB.
- About 5% of the teststructures are shipped to the three *Process Qalification Centers* (PQC). These centers receive about 5% of sensors as well, to perform *Long Term Validation* (LTV) tests.
- Another 5% teststructures and 1% of sensors is shipped to the two *Irradiation Qalification Centers* (IQC). The two centers perform irradiation either with neutrons or protons.
- 94% of the sensors are shipped to the module assembly centers via the QTCs, another 5% should be passed down from the LTV centers. The 1% irradiated sensors are lost for module production.

4.2.1 Quality Test Control

The QTC measurements are extensive tests, perfromed on the silicon sensor. They characterize some of the major parameters to ensure that individual sensors are within specs. The measurements include:

Visual Inspection utilizing a microscope is done to make sure, that the silicon did not experience any obvious mishandling like scratches or broken corners. As the edges are an area of high fragility, special attention is payed to these regions of the detector.

IV-Curves are taken to determine the total leakage current at 0 V to 550 V reverse bias voltage. This is done by contacting the bias ring and the backplane applying the desired voltage and measuring the resulting current.

CV-Curves are important to determine the depletion voltage of the sensor. Again the voltage is applied between bias ring and backplane, while measuring the total capacity of the detector. The voltage at which the minimum capacitance is reached is stated as the depletion voltage (at zero irradiation).

The Per-Strip Leakage Current ($\mathbf{I}_{strip}$) is measured for each strip on the detector at a reverse bias voltage of 450 V. It should not exceed 100nA otherwise the channel will be marked as *leaky strip*.

The Polysilicon Resistance (R_{poly}) is measured for each strip. Accepted values should be within 1.5±0.5 MΩ for each channel and an uniformity of 0.3 MΩ with respect to the average R_{poly} for all strips of the sensor is required.

I_{diel} is measured to ensure that there are no undesired connections between the implanted strip and the aluminium readout strip, so called *pinholes*. By applying a small voltage of 10V between backplane and the aluminium readouts, the resulting current is measured. If the dielectric SiO_2 layer is still intact, there should be no measurable current.

Figure 31: Pictures of the probe station setup. The left picture shows a long shot of the equipment including the computer, the measuring devices and the light tight box. The right picture shows a closer look into the box. A microscope, the contact needles and the motorized XY-table can be seen.

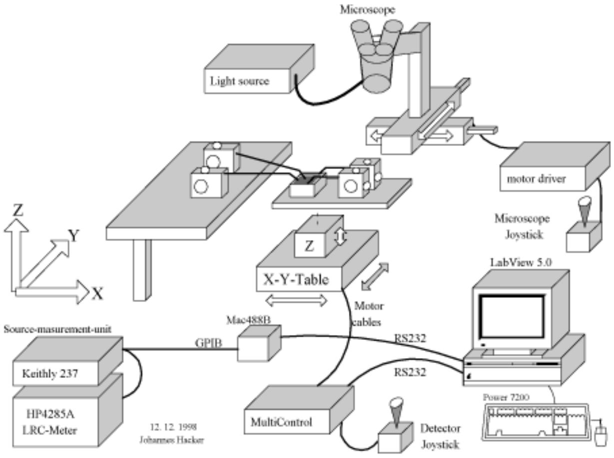

Figure 32: System overview of the semiautomatic probe station used for quality tests on silicon sensors.

The Interstrip Capacitance (C_{AC}) is another test for pinholes. This time two strips are contacted with three needles, where the AC and the DC pad on one strip and the AC pad on an adjacent strip are used. If the aluminium readout strips are shorted, only this switching scheme is ensuring that a different capacity is measured (about twice as much) than when they are still will isolated from each other.

A semiautomatic probe station (see fig. 31) has been set up to perform the tests. After manual insertion, it is able to complete a test on a sensor in about 3-4 hours without any further user interaction. Fig. 32 shows a block diagram of the equipment used to set up the station.

The detector is situated on a chuck in a light tight box, and is contacted with several needles. The HV bias voltage is applied to the backplane via the chuck, while the bias ring and 2 adjacent strips are contacted with needles.

Figure 33: The LTV setup

Theses contacts are plugged into a switching matrix, which connects the sensor with the voltage supply and various measuring equipment. The equipment is monitored and operated with an Apple Macintosh computer running a custom made LabView[10] application.

The test data gathered on each sensor is stored locally and inserted into the TrackerDB for further reference. Sensors not fulfilling all the minimum specifications are rejected. Nevertheless complications in the manufacturing process can (and have) happen and may force the test procedures to be changed and made compatible to the new situation. One such occasion is described in chapter 6.

4.2.2 Longterm Validation

An important aspect of the quality control process is the investigation of longterm effects. Aging of the detector can have a significant impact on the performance and the harsh radiation environment inside the CMS experiment is usually making things even more difficult.

The goal of the LTV measurements is to detect fluctuations in sensor dark current over an extended period of time and under defined and monitored environmental conditions. It is a very simple but time consuming test, therefore a simultaneous measurement of several sensors was approached. The current setup as pictured in fig. 33 consists of:

Keithley 2410 source measure unit. It serves as a power supply for the reverse bias voltage for each sensor. Contrary to most other measurements a voltage of -400 V is applied to bias ring while the backplane is connected to ground.

Keithley 2700 scanning multimeter with 7702 multiplexer card. This device

---

[10] LabView by National Instruments is a visual programming language suitable to quickly prototype user interfaces and control applications. Take a look at http://www.ni.com/labview/ for more information.

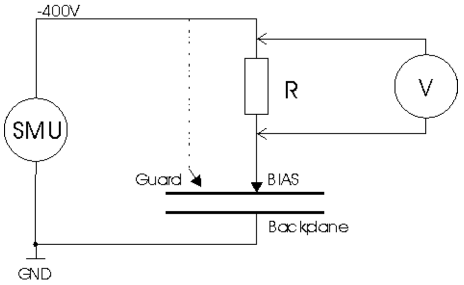

Figure 34: The LTV measuring principle.

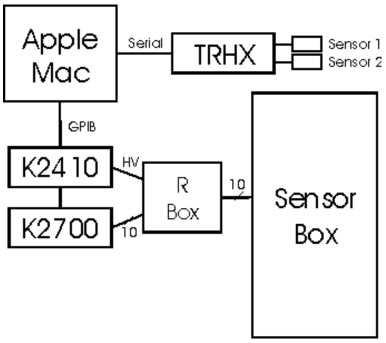

Figure 35: The LTV setup. The Apple Macintosh computer was later replaced by a standard PC.

is able to measure up to 40 different channels, 10 are used in the current setup.

TRHX Temperature and Relative Humidity eXtended. This little gadget, made by Markus Friedl is able to monitor several temperature and humidity sensors and transfer the data to a computer via the common RS232 serial interface.

R Box box of resistors. It contains the resistors, which are coupled into the bias circuit of each sensor to measure the current.

Sensor box light and air tight sensor container. It has some convenient sliding tables for inserting the sensors while sealing it from the outside environment during measurement (see fig. 36).

4.2.3 Process Qualification Control

Testing each of the 25000 sensors at the QTC is an impossible task and would requiring to much manpower, equipment and time. So only a fraction of the manufactured sensors will be tested in QTC while most of them will be accepted based on the process qualification tests. The idea is, that among a batch of sensors which are produced in a single sequence on the same machine, on the same day, the parameter spread is supposed to be quite low. So if a batch's process can be qualified as good, the whole batch is accepted.

To monitor the process quality some special structures have been designed to be included on each wafer. So each of the 300 mm wafers does not only contain a single detector, but also a bunch of test structures, the so-called *half moon*. The structures on this part of the wafer are cut from the actual detector by the manufacturer and sent to the PQCs. See fig. 37 for a sketch of the patterns. The measurements conducted on the test structures are:

The Coupling Capacitance (C_{ac}) is measured at the Ts-CAP structure. It is made of 26 strips directly coupled to a bias line and the dielectric structure is the same as for the detector. The insulation layers thickness can be derived from this parameter.

Figure 36: The opened Sensor Box. One of the tables is extended and the conductive rubber which connects the bias voltage to the backplane can be seen.

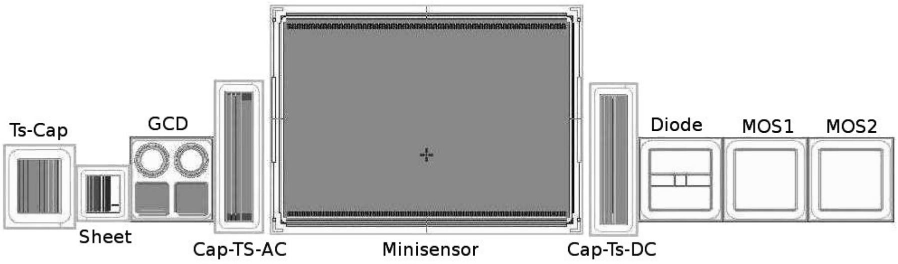

Figure 37: The standard half moon with it's nine test structures.

The Dielectric breakdown (IV_{diel}) is measured at the Ts-CAP structure as well. Contrary to the breakdown of the silicon bulk which is caused by an avalanche effect of charge carriers, the dielectric breakdown is caused by electrons stripped from their atoms. Impurities of the insulating oxide are influencing this effect. This is a destructive test!

The Flatband Voltage(V_{fb}) is done on one of the *Metal Oxide Structures* (MOS1). A CV measurement (CV_{MOS}) is used to derive the flatband voltage. This uncovers how the interface mobility charge beneath the gate acts on the applied bias voltage.

The Surface Current (I_{surf}) is measured at the *Gate Controlled Diode* (GCD) structure which in fact houses 4 GCDs, two circular shaped and two square ones. The right square diode which is used, is made of comb shaped p$^+$ implanted strips entwined with metal-oxide strips. This resembles the interstrip region of the sensor. The current through the diode is plotted while the voltage applied to the gate is varied. The I_{surf} is then extracted from the plot. High surface currents indicate contamination of the oxide during the manufacturing process.

The Sheet Resistances contains 3 resistances which are measured: aluminium, p$^+$ implant and polysilicon resistors. For each material 3 test strips are implanted on the structure to measure the specific resistance of the first two materials while the polysilicon resistor is the same layout as on the actual detector and therefore the particular resistance is measured on the same three copies of the structure.

The Interstrip Capacitance (C_{int}) is measured on the Cap-TS-AC structure. This is an important value to ensure that the readout electronics can operate with high S/N ratios which can only be achieved with a low C_{int}.

The Depletion Voltage and Resistivity (CV_{diode}) is tested on the diode structure in the half moon. The CV curve of the diode is used to extract the depletion voltage which can than be used to derive the bulk resistivity.

The Dark Current and Breakthrough (IV_{baby}) are measured on the minisensor which is a small, 192 strip replica of the actual sensor. An IV curve is plotted and the current at 450 V is read from it, while the breakthrough voltage is made sure to be beyond 500 V.

The Interstrip Resistance (R_{int}) is measured in the CAP-Ts-DC structure. It is very similar to the CAP-TS-AC structure.

The test setup consist of several instruments connected via a switching matrix to the half moon test structure. The contacts to the structure are made with a custom made probecard (see fig. 39) supplied by an industrial manufacturer. The setup is controlled by a computer running a LabView program (see fig. 38).

The probecard is establishing all the connections to the half moon at once with small needles. The card and the connected test structure are kept in a light tight box during measurements (see fig. 40).

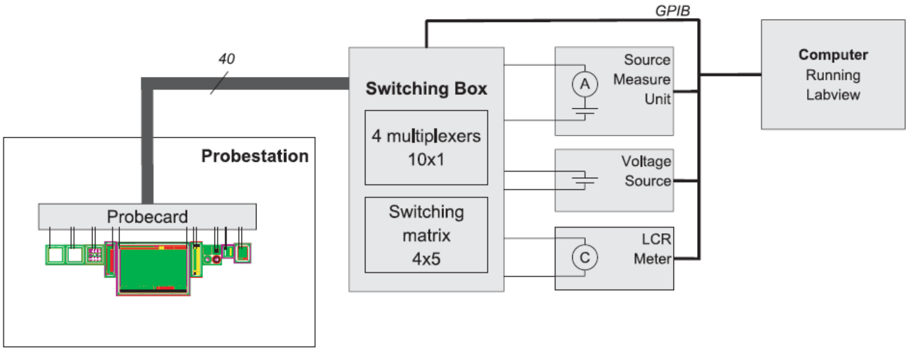

Figure 38: The PQC setup. The probecard and the test structure are located in a light tight box.

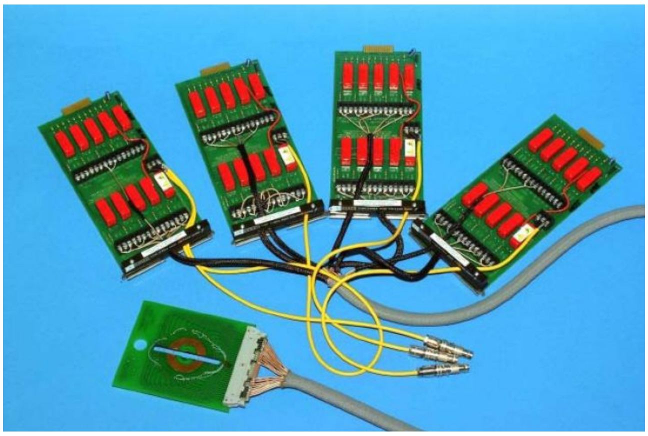

Figure 39: Picture of the probecard connected to four K7154 multiplexer cards. The yellow cables are connected to the K7153 matrix card.

Figure 40: The PQC setup. On the left side the necessary electronics can be seen and on the right side is the gray light tight box

4.2.4 Irradiation Qualification Control

To make sure that the detectors can withstand 10 years of LHC radiation environment, irradiation test have been introduced. Two facilities are used to commence the tests. The *Institut für Experimentelle KernPhysik* (EKP) at the University of Karlsruhe is doing irradiation tests with protons while at the *Universite catholique de Louvain* similar measurements are done, but with neutrons.

4.3 Modules

Having even perfect silicon sensors at disposal is only half the way to a working detector. The sensor has to be integrated into modules not only for stability and handling reasons but also for certain constraints of the readout process.

For the assembly of the modules, 4 major parts are shipped to the HEPHY:

The Carbon Frame which already includes the kapton wiring.

The Hybrid which contains all the on-module readout electronics and the pitch adapter. These parts have already gone through an extensive QA program prior to shipping.

The Rigidifier is a simple piece of plastic which should give some additional mechanic stability to the silicon sensor

The Silicon Sensor the most delicate part, which has already gone through the QA procedure described in the preceding chapter.

Before the assembly process is started, some of the components are subject to additional test, to ensure their integrity after shipment and storage. This includes a quick check on the parameters of the resistances, thermistors and

Figure 41: The chucks used for placing the components during assembly. The recess for the components can be weakly seen.

capacities on the kapton circuitry and some visual and electric tests on the hybrid. The kapton tests are done dirty and simple with a multimeter. They are only done to ensure that frames, which where already stored for some time, are still within specs. In future these test might be skipped.

Although the hybrids and its components(electronics, pitch adapter, bonds) have already been qualified and tested after each of the manufacturing and assembly processes, a short test is also done in our lab. This includes a short visual inspection according to the *visual inspection sheet* which can be found in the appendix. The individual components are scanned for visible defects with a microscope.

The first shipments of hybrids were all characterized electronically with a custom made, specialized test setup. The hybrids had to pass a *fast test* (see chapter 5 for further explanation) but also some additional tests were done for future reference. As these test tended to be not very conclusive but still time consuming, they might be skipped if the hybrid quality arriving at the institute continue to show the experienced continuity.

4.3.1 Assembly

The assembly process is a very delicate and important step. Sensor alignment has to be within tough limits in the order of μm, which led most institutes to use a completely automatised assembly machine, the *Gantry*[11]. However, at the HEPHY a more manual assembly procedure was chosen. Only aided by custom made chucks (see fig. 41) for placing the components and a massive, high precision coordinate measuring machine (see fig. 42), all steps are done by hand.

Certain assembly parameters like sensor placement precision, are all uploaded to the database. The statistics derived from these measurements showed

---

[11] for further information on this machine and the employed assembly procedure consult the Gantry group Web Page at http://www.ba.infn.it/˜CMS_TRKR/gantry1.html

Figure 42: The coordinate measuring machine used to ensure proper alignment of the indivdual components on the module.

an interesting point. The manual assembly process used at the HEPHY showed smaller deviations from the design parameters, than the fully automated one of the gantry robot!

4.3.2 Bonding

After assembling the module, the connections between PA and the sensor have to be made. This is done by *ultrasonic wire bonding.* Small 25 μm aluminium wires are soldered to the sensor pads and the pitch adapter. This was done with an Kulicke & Soffa bonding machine for the first production cycle, but in January 2005 a new Delvotec 6400 automatic bonding machine was commissioned (see fig. 43). This will not only improve the throughput significantly but should also have some influence on the overall bonding quality.

Once again, the most important bonding parameters are monitored and uploaded to the TrackerDB afterwards.

4.3.3 The ARC test

The completed module will then be tested for a number of parameters. Problems that should be easily found can be attributed to two categories:

- Flaws inside the sensor caused by mishandling or by fluctuations in the manufacturing process which did not already show up earlier in QA tests.
- Mistakes during the assembly or bonding process, like open bonds, shorted wires or loose connections.

Figure 43: The new Delvotec 6400 wire bonder.

It should be possible to recognize defects from both categories. The test methods will be explained in detail in the subsequent chapter (chapter 5), but the problems that could turn up and are expected to be detected by the testsetup are referenced in this flaw list. Flaws inside the sensor:

Pinholes are shorts between the p$^+$ implant and the aluminium readout strip. They are caused by defects in the insulation layer and are not only generated during the manufacturing process, but could also develop later. It is not clear if they emerge from an already weak insulation with time or how far mishandling of the sensor influences the creation of pinholes.

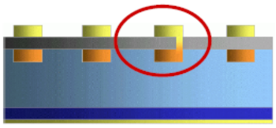

Shorts are quite similar to pinholes, a defect in the insulation layer, but between implants or between aluminium readout strips. The behaviour of such strips looks just like a short produced outside the sensor by the bonding wires as explained in the second flaw list.

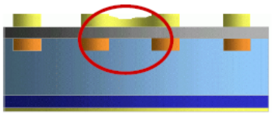

	bad channels	current @450 V
Grade A	<1%	<10 μA
Grade AF	<1%	$> 5\times \mathrm{I}(450)_{DB}$[12]
Grade B	<2%	<10 μA
Grade BF	<2%	$> 5\times \mathrm{I}(450)_{DB}$[12]
Grade C	>2%	
Grade C		>10 μA

Table 5: Grading scheme for modules. Only grades A(F) and B(F) are considered for integration in the Tracker

Noisy Strips are, as the name suggests, strips with increased noise. This is usually caused by an increased leakage current on the strip (remember: noise scales with the current fluctuations or more precisely with $\sqrt{I}$).

High Bias Current Is caused by defects in the bulk material. It poses a high risk for failure of the detector in the future.

Flaws outside the detector:

DCU is read out and the parameters are checked for consistency. This shows any faulty measurements, but may also point to actual problems of the electronics power supply.

Pipeline cells are checked for consistency. If any of the storage cells are damaged, this should show up in the tests.

Opens are disconnected or missing bonds. This can be repaired easily be rebonding the affected channel.

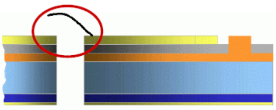

Shorts may be caused by twisted bonds or dirt shorting some channels. These outside effects can also be repaired by cleaning or rebonding the affected channels.

High Bias Current may also be caused by defect or misaligned components on the module.

Naturally there may be additional defects that can not be clearly categorised. Such unexpected effects should still show up in the tests as irregularities which do not fit into any of the expected failure signatures.

The modules are graded into 3 categories according to the test results (see table 5).

---

[12] $\mathrm{I}(450)_{DB}$ bias current at 450 V from sensor probing data.

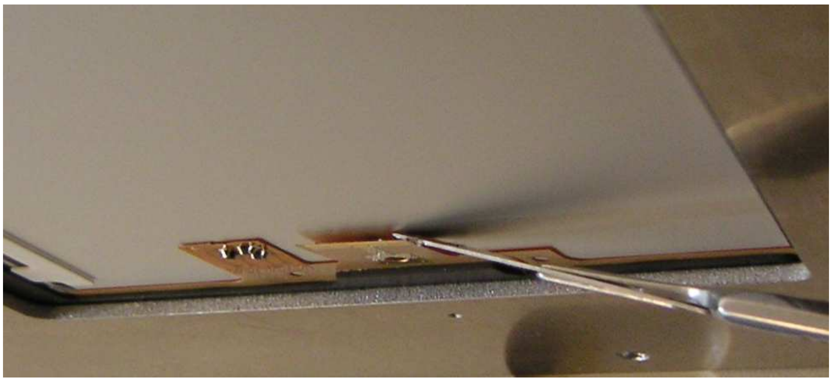

Figure 44: The HV connection of the backplane came loose on some modules early in the production stage. The problem was identified as a lack of pressure during the glues drying phase.

4.3.4 Cooling Tests

For the first production cycle additional cooling tests were commenced. It was agreed that after a first full test run, the modules were cooled down to about -15°C and back to room temperature. This cooling cycle was done about 3 times[13] but later the cycle was extended to -20°C to +50°C. This was necessary due to a problem in the assembly process, where the glue connecting the HV connection of the kapton circuitry with the sensor backplane came loose (see fig. 44). It was believed, that the aggravated cycle would put additional stress to the weak connections without harming any of the other components. It proved quite useful until the remedy of the problem was found by altering the gluing scheme of the backplane connection.

After the cooling cycle, the modules were exposed to a second full test, to identify any problems due to the thermal stress. For simplicity the modules are not tested during the cooled down state, but it is believed that there should be no additional problems for modules that could do a cooling cycle and show the same performance afterwards.

In the later production stage, when the modules proof to be unimpressed by the cooling cycle, this step will be skipped. The cooling cycle with it's additional test, actually puts a constraint on the module test throughput, which will make it necessary to skip this procedure anyway, during the full production phase.

---

[13] Due to limitations of the cooling box control program, the device was usually shut down remotely from home late in the evening. This resulted in irregular repetitions of the cooling cycle.

Figure 45: The cooling box loaded with several modules. The thick isolating material can be clearly seen on the door and inside the box.

5 The Module Teststand

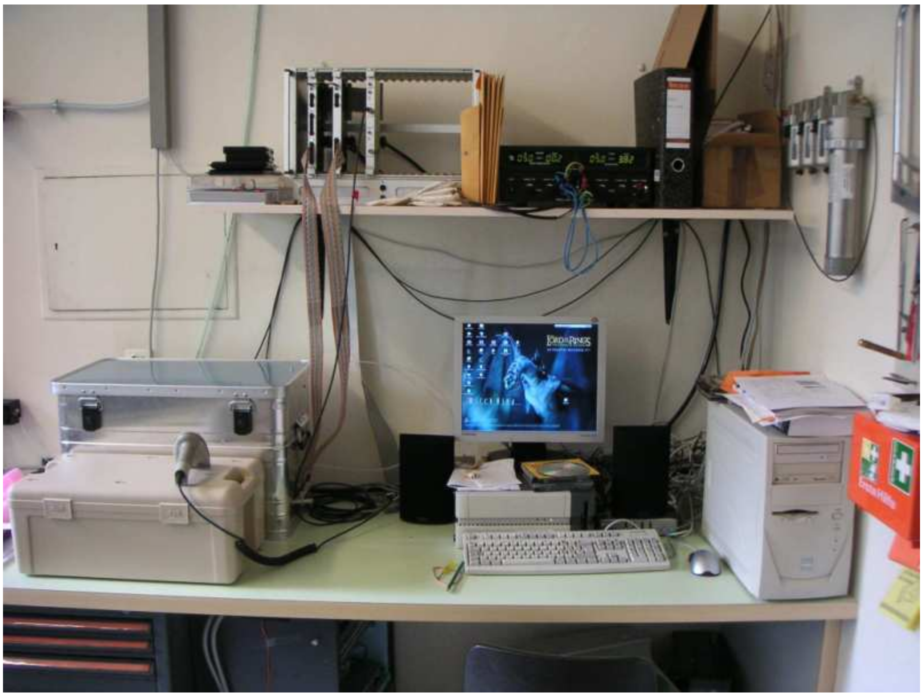

The testing of the modules is done in several different institutes in Europe and the USA. To make sure that the testing conditions are similar at all labs, most of the testing equipment was custom made at the Institute III B of the *Rheinisch Westfählische Technische Hochschule* (RWTH) Aachen[14]. The core equipment like the readout hardware and testing/analysing software is the same at all test labs and therefore results should be comparable. Nevertheless, some of the equipment was left to be developed by each institute to their own specifications, like the Test Box.

5.1 Hardware

The Hardware required to build a CMS silicon teststand consists of several custom made devices. The module control and readout system is commonly referred to as the *APV Readout Controller* (ARC) or ARC system. A test box offers a light tight and humidity controlled environment for the modules while testing and the approved Vienna Coolingbox is put into place to perform the cooling cycles.

5.1.1 The ARC System

The ARC system consists of several devices designed and built by Aachen IIIB and some additional standard support equipment like power supplys and crates.

---

[14] The institute will be further referenced as Aachen IIIB

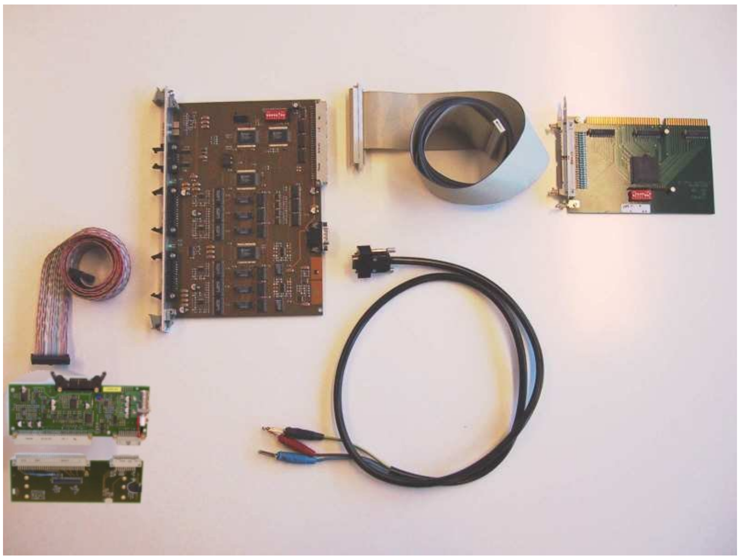

Figure 46: The ARC readout system consist of (from right to left): the PCMIO interface card, the ARC board and the front end adapter. The flatband cables are used to interconnect the devices and a D-Sub to banana plugs cable is used as a line cord.

Readout and Control Hardware The core equipment is the readout and control hardware (see fig. 46). It consists of three devices:

The PCMIO Interface Card fits into a standard ISA slot and serves as an interface for the computer to the ARC boards. A large flatband cable connects it to the ARC board.

The interface card is one of the main drawbacks of the ARC system: the already outdated ISA bus is not easy to get on cheap standard consumer mainboards and modern Windows operating systems like Win NT/2000/XP are very restricted in direct I/O access to periphery. A special hack[15] had to be implemented to make the interface work.

An equivalent parallel port interface should be available from Aachen IIIB as well.

---

[15] for more information on the needed device driver and the installation have a look at http://www.physik.rwth-aachen.de/group/IIIphys/CMS/tracker/en/index.html

The ARC board houses the core electronics to operate detector modules. It is capable of digitising the analog data from the APVs, provide clock and trigger signals and monitor and control all the chips on the hybrid via several I^{2}C controllers. With it's two hybrid connection sockets it is capable of operating two modules at once. An expansion port can be used to feed external clock and trigger signals. Two additional NIM ports are implemented to accept yet another external trigger and a busy signal.

The board is a standard double euro format PCB and can be placed in a 19" crate. It requires a power supply capable of providing +5V/2 A and -5V/1 A for operation.

The Front End (FE) Adapter connects (through the Hybrid-to VUTRI adapter) directly to the hybrid and must therefore be located inside the test box. It houses amplifiers, line drivers and voltage regulators. This design enables long cables to the ARC board and easier adaption to new hybrid designs.

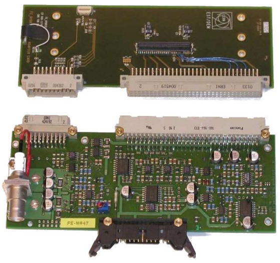

Light Emitting Diode (LED) pulser system An extension to the minimal ARC system is the LED pulser system. It is able to expose the module to electromagnetic emissions in the infrared wavelength region. This can be used to test the sensors response to light pulses or to increase the leakage current by using continuous light. The system consists of:

The LEP16 is the main controller board and is also built on a standard double euro format PCB to place it in a 19" crate just like the ARC board. It is controlled via the connected PCMIO card and the NIM trigger port must be linked to the corresponding socket on the ARC board. A similar power supply with +5 V/-5 V voltages is needed for operation.

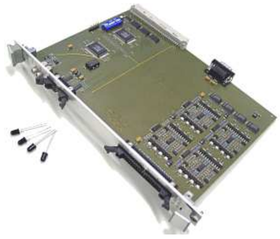

The LED box houses the 16 infrared LEDs in a plastic enclosure. The LEDs are mounted on an aluminium profile and each light source is coupled to four optical fibres, totaling 64 small light sources. The box is connected to the LEP16 controller via a flatband cable.

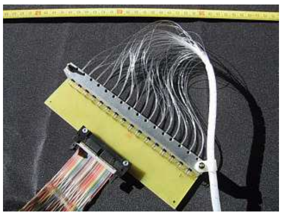

The Emitter is just a small plastic board supporting the array of 64 optical fibres in a pitch of 2mm. It must be place directly above the sensor and is firmly attached via the fibres to the LED box.

DEPletion Power board During the tests, the detector must be operated in depleted mode. An appropriate voltage has to be applied to the sensor, which was agreed to be 400 V for our test purposes. Additionally, one of the tests to be performed, is an IV curve of the sensor where the leakage current has to be measured on a scale nA. Therefore a HV power supply, which is controlled by the ARC system is required. The DEPP is built on the same form factor as the previous two boards and is also connected to the PCMIO interface. Additionally, it requires the same power supply as the previous two boards.

The Crate A standard NIM crate was used to house the ARC board, the LEP16 controller and the DEPP power supply. They are all connected to the same flatband bus cable to the PCMIO interface cable. The crate serves as a convenient and save place to store the boards, but does not have any additional functionality, like power supply or bus connection.

Power Supply A standard power supply (EA-PS 3226-050) is used to power all three boards. The unit is able to supply 2x0..16 V at a maximum load of 5 A. Interestingly, during measurements the current rises even beyond the specifications without compromising the stability of the unit.

The PC A standard PC running a windows operating system is required to run the necessary software environment. Nevertheless, the PC must support ISA expansion boards to accommodate the PCMIO card, which is a noteworthy restriction nowadays, as the ISA bus is already outdated in modern consumer PCs. In contrast to that, the software used to operate the ARC equipment does indeed require the computing power of modern computers.

5.1.2 The Test Box

The test box was custom made at the HEPHY. It should serve several different aspects:

- A light tight environment is needed to operate the detectors. Even small light leaks could drive the leakage current into undesirable regions, which could even damage the sensors, let alone falsify measurements.
- Protection from environmental electromagnetic emissions is essential to shield the electronics. The modules are very sensitive to EM emissions, which would increase the noise that is picked up. A low noise pick up is essential for some tests to give decent results, despite the already built in noise suppression algorithms.
- Another important factor in shielding the module from noise is a proper grounding scheme. Lot's of work has been invested to make the noise level comparable to the different test boxes in the other involved institutes.

Figure 47: The ARC Test Box.

- Simple mechanics to house the module, the FE adapter, the emitter including the LED box and the required cable connections. It should be easily possible to change modules even for different geometries. The LED emitter should be adjustable in height and position with respect to the sensor.
- A low humidity environment must be ensured inside the test box. The relative humidity should be always below 30% when a module is loaded.

The box is a 59 cm×38 cm×38 cm (w×h×d) aluminium case (see fig. 47) with a top opening cover. It offers plenty of space to house all the necessary components and even more.

Inside, a small 45 cm×22 cm (l×w) table (see fig. 48)was mounted to support the test module and the FE adapter. The module (including its transport plate) is positioned on the table by two isolating plastic rails. The FE adapter is also isolated on a block of plastic. The table itself is connected with a thick wire to the box to ensure a proper connection

Two aluminium rails are mounted inside the box on the backside, to support a movable plastic bracket to support the LED emitter. It is adjustable in height and position with respect to the sensor and can be retracted to change the loaded module.

5.1.3 The Vienna Coolingbox

During the first production phase, all modules were subjected to a cooling cycle. They were cooled down to about -20°C and back to room temperature. The cycle was performed about three times. This was done to make sure, that the modules can withstand the thermal stress put on them, when they are cooled down to operation temperature (-15°C) in the tracker and back to room temperature during service intervals. Special attention is paid to bonds getting loose after the cycle or loosened HV connections due to brittle or lack of glue.

As soon as the assembly and bonding process seems to be stable enough to render the cooling cycles useless, they will be skipped for the sake of the needed

Figure 48: The inside of the test box. The LED emitter is placed just over the sensor and on the left the FE adpater can be seen.

module production throughput of two to 4 modules per workday.

The *cooling box* (see fig. 49) is composed of several components[5]:

The box is thermally isolated and holds up to 10 modules on transport plates[16]. It incorporates two water cooled peltier elements for cooling and heating, each offering up to 350 W, temperature sensors inside the box and a gas supply to regulate the humidity inside the box.

The Power Supply offering 0 - 25 V at a maximum of 15 A. It is a custom made solution that can be operated remotely or with a small LCD display on the front panel.

The TRHX is also used in this setup to monitor the temperature and the relative humidity in various places inside the box. Additionally the TRHX_base component has the ability to remote control the power supply for the peltiers as well.

The Control/Monitoring Software runs on a PC with an RS232 serial interface connected to the TRHX_base. It is implemented in LabWindows/CVI[17]

5.2 The ARC Software

A comprehensive software package has been developed by Aachen IIIB to operate the ARC equipment. The software is simply called ARC Software (ARCS) and the latest release[18] can be found at the ARCS webpage[19] including some

---

[16] Simple aluminium plates with a recess for the active sensor area and some mounting holes to secure the module frame, act as handling and transport plate.

[17] An ANSI C development environment with numerous run-time libraries specialized for developing measurement applications. Developed by the same guys that brought us LabView, take a look at http://sine.ni.com/apps/we/nioc.vp?cid=11104&lang=US

[18] All descriptions in this thesis refer to ARCS V7.1 - newer versions should contain a similar set of features.

[19] http://www.physik.rwth-aachen.de/group/IIIphys/CMS/tracker/en/index.html

Figure 49: The cooling box loaded with several modules. The thick isolating material can be clearly seen on the door and inside the box.

additional information. In the final release ARCS should be capable of reading all the information provided by a module via the I^2C bus, execute several complex measurements on the module and interpret the results with several flexible fault finding algorithms. These results should be prepared by ARCS for the upload to the TrackerDB. At the current status when this thesis was written[20] not all features where implemented or ready for use in production. To accomplish the requested operations, like the creation of XML files for the TrackerDB, additional software was used (see chapter 5.3).

Two important files are located in the ARCS install directory:

- `ARCS_main_config.cfg` describes the necessary main parameters for ARCS, which have to be set once when commissioning the software package. The options are commented in the file quite thoroughly and should be easy to adapt to the particular circumstances.
- `testsettings_module.xml` holds all the cuts for the flagging of faulty module channels in an XML file structure. The version used in the first production phase at the HEPHY can be found in the appendix at page 101. It does only contain the most important cuts and settings.

To work properly, ARCS requires three software packages to be installed:

LabView 6.0.2 Runtime Engine [21] The basic LabView runtime engine, to make LabView programs run on machines without the full LabView programming environment installed

ROOT 3.05/02 [22] ARCS is creating .root files to store the test results. This requires a ROOT installation to manipulate these files.

Xerces 2.2.0 [23] is needed for the generation of the XML files needed for the TrackerDB upload.

5.2.1 Main Monitor View

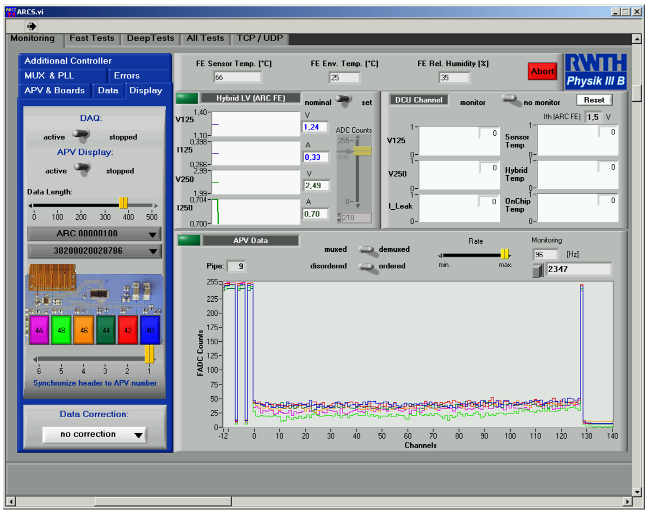

FE Sensor Temp. [°C] 66
FE Env. Temp. [°C] 25
FE Rel. Humidity [%] 35
Ith (ARC FE) 1,5 V
V125: 1,24 V
I125: 0,33 A
V250: 2,49 V
I250: 0,70 A
DAQ: active / stopped
APV Display: active / stopped
Data Length: 0 100 200 300 400 500
ARC 00000100
30200020028786
Data Correction: no correction
Pipe: 9
Monitoring 96 [Hz]
2347

---

[20] 1st quarter of 2005

[21] Can be obtained at www.ni.com

[22] Can be obtained at root.cern.ch

[23] Can be obtained at http://xml.apache.org/xerces-c/

After initializing the modules, the first screen visible in the ARC software is the monitoring page. It provides a short overview of the module parameters read from the APVs and the DCU. The upper left part of the main window shows the low voltage power supply on the FE adapter and the right part shows the temperature and power readings read from the DCU.

In the lower part, the analogue data of all active APVs is sampled. Each color represents an individual APV were the first few (negative) ticks represent the header and channels 1 to 128 are the actual analogue data.

The tabs on the far left side, give access to various settings of the APV, PLL and the MUX chips(*MUX & PLL* and *APV & Boards*), offer simple raw ASCII data taking capabilities (*Data*) and provide a simple error display (*Errors*). The *Display* tab holds some settings for the analogue data display on the right hand side.

The *Additional Controller* tab gives access to additional control panels, see section 5.2.2

5.2.2 Additional Controllers

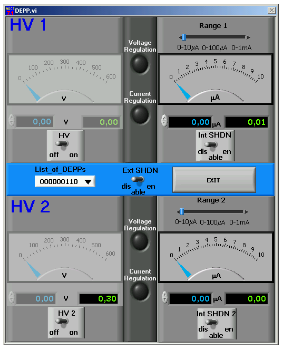

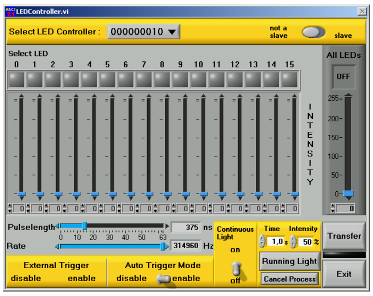

In this tab the buttons *LED* and *DEPP* open separate panels to control the LED16 controller and the DEPP HV supply. This enables the realisation of custom tests utilizing the two devices. All the parameters can be set individually to perform such tests.

When starting the *Fast Tests* or most of the *Deep Tests* individually, the HV must be selected manually. Only the *IV* test runs the HV automatically just as the *LED* and the *Pinhole* tests do with the LED controller. For all other tests, the parameters have to be set manually. When starting *All Tests*, DEPP and LED16 are set up automatically.

5.2.3 Fast Test

The *Fast Test* performs some short measurements, testing the basic functionality of the module's chips. Short noise and pulseshape tests are run to have the opportunity to recognize most bad channels very quickly. This test can be done on modules and on hybrids as well.

A text protocol is saved on disk, which already gives an overview of any apparent faults on the module. A failure in the module component tests usually depicts a bad hybrid which is beyond repair. Problems reported in the noise and pulseshape tests may only be a hint to a problem on the module and should always be verified with the corresponding deep tests.

5.2.4 Deep Test

These set of tests are the main analysing tools for finding faulty channels on a module. Each of the tests was chosen to recognize different problems, although most faults show specific signatures in several tests. Only by interpreting all the tests combined, a reliable conclusion can be made.

Usually a module is tested by utilising the *All Tests* tab. It allows to start a predefined standard set of tests and stores the gathered information in a root file together with a test protocol indicating any found bad channels. Nevertheless, it is possible to run each of the tests individually as well.

Pedestals & Noise & CM

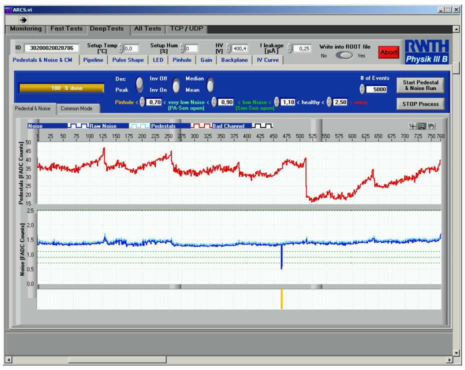
ID 30200020028786
Setup Temp [°C] 0,0
Setup Hum [%] 0
HV [V] 400,4
I leakage [µA] 0,25
Write into ROOT file No Yes
100 % done
# of Events 5000
Pinhole < 0,70 < very low Noise (PA-Sen open) < 0,90 < low Noise (Sen-Sen open) < 1,10 < healthy < 2,50 < noisy

This test is fulfilling three entwined tasks:

- At first, it is doing a pedestal run. It measures the analogue signal of each channel several times and calculates the average for every channel. This way the electrical zero point of each channel is calibrated. The red data in the upper diagram depicts the pedestals.

- Then the noise picked up by the module is recorded for a selectable number of events. This raw noise is shown in the lower diagram in dark blue.

- Then the *Common Mode* (CM) correction is applied to the data. It simply calculates the average of a bunch of 32 channels and subtracts the result from each one. This should eliminate any influences which affect several channels. The resulting *common mode subtracted noise* is shown in light blue on the lower diagram. A histogram for each APV showing the CM noise is calculated when selecting the *Common Mode* tab.

The noise test is a good indicator for opens. Usually Pinholes and shorts do also show characteristic signatures in this test but other tests are more suitable to correctly identify these problems, nevertheless it provides an additional indicator.

The noise that the APVs are experiencing is directly connected to the capacity that is loaded on the preamp inputs of the chips. So the noise test is basically a measurement of the capacitive load that is put on the preamp stage of the APVs. This naive interpretation of the noise measurements is only true if the CM noise is low enough. A maximum of 0.5ADC[24] counts was found to be necessary.

Defects that can be identified:

Open Bonds decouple the readout strips from the APV and therefore reduce the capacitive load on the input. This results in reduced noise. For two sensor modules, [25] even opens *between the sensors* or *between sensor and PA* can be distinguished.

Shorts can come in three variations: on the hybrid, between aluminium readout strips or between p^+ implant strips. Shorts cannot be safely found by the noise test, nevertheless they usually all show reduced and very similar noise.

Pinholes reduce the measured noise significantly to almost none. Therefore pinholes should have an even smaller noise behaviour than opens. These defects are very problematic for the APVs as they put a high load on them and can cause them to fail completely if the load is to high. Therefore, these channels are disconnected by removing the appropriate bond.

Pulse Shape

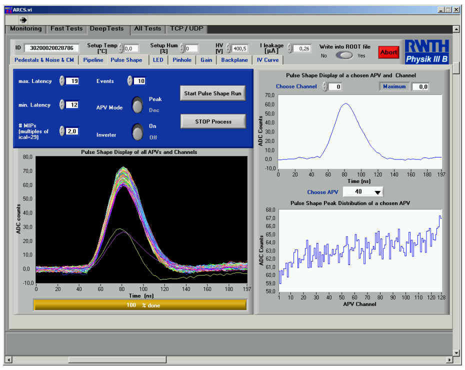
ID 30200020028786
Setup Temp [°C] 0,0
Setup Hum [%] 0
HV [V] 400,5
I leakage [µA] 0,26
Write into ROOT file No Yes
max. Latency 19
min. Latency 12
MIPs (multiples of ical=29) 2,0
Events 10
APV Mode Peak Dec
Inverter On Off
Choose Channel 0
Maximum 0,0
Choose APV 40
100 % done

This test uses the built in capability of the APVs to put a self generated, calibrated amount of charge on each channel. The signal that is produced by the injected charge is then measured. Actually, each pulse is measured several times with different latency settings, to draw the complete shape of the calibration pulses.

The shape of the returned pulse is also closely related to the capacity the APVs are experiencing on the input stages. The bigger the capacity, the broader the pulse will get. This enables the tagging of faulty channels by deducing two parameters:

The Pulse Height is the maximum signal height of a pulse. Bigger capacity will result in a reduced pulse height.

The Peak Time is the latency setting that is required to get the maximum pulse height. Bigger capacity makes pulse's reach their peak later.

---

[24] The standard deviation calculated on the *Common Mode* tab of the ARCS noise test.

[25] At the HEPHY only TEC Ring two modules are produced which do only contain a single sensor.

The pulse shape test is an excellent tool for tagging opens and shorts and is usually also very reliable in finding pinholes. Unfortunately this test is also prone to mistag channels. This may happen, for example, when the charge injection mechanism on the APV is faulty.

Open Bonds put a significantly reduced capacity load on the APV and therefore the pulse gets much narrower and higher. This is shown in a slightly reduced peak time and an increased pulse height.

Shorts are sharing single charge injections among them. This causes a significantly reduced pulse height, where the amount of reduction is directly connected to the number of shorted channels. A two-channel-short will reduce the normal signal height to one half, a three-channel-short will be reduced to one third.

Pinholes are usually not responding to a charge injection at all. The pulse is almost completely flat. This is not always true due to some of the intrinsic features of a pinhole.

Pinhole

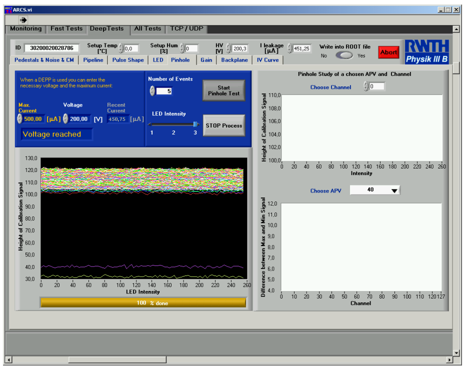

When a DEPP is used you can enter the necessary voltage and the maximum current:

ID 30200020028786
Setup Temp [°C] 0,0
Setup Hum [%] 0
HV [V] 200,3
I leakage [µA] 451,25
Max. Current 500,00 [µA]
Voltage 200,00 [V]
Recent Current 450,75 [µA]
Voltage reached
Number of Events 5
Choose Channel 0
Choose APV 40
100 % done

As the name already suggests, this test was specifically developed to tag pinholes. This is can be done due to a unique property of the pinholes, but it requires the use of the LED system.

Pinholes are (resistive) connections between the aluminium readout strip and the p$^+$ implant. This causes the virtual ground of the APVs preamp input stage to be pushed towards the implants potential. This "drag" is depending on the resistivity of the pinhole, which in turn changes with the current running through it.

The pinhole test utilises this unique feature by varying the leakage current of the sensor, while measuring the calibration pulse height. The leakage current is increased by injecting continuous light with the LED system. Depending on the current running through the strips, the pulse height is changing according to the shift of the virtual ground of the preamp input, until a certain point were the preamp is back at its normal optimal working point. Afterwards the signals height is once again decreasing.

The other defects show a similar behaviour as in the pulse shape tests, without any impact of the leakage current variations.

IV

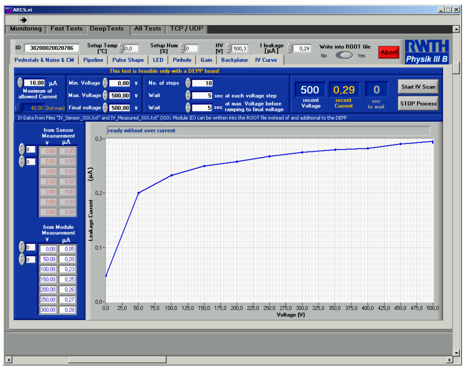

ID 30200020028786
Setup Temp [°C] 0,0
Setup Hum [%] 0
HV [V] 500,3
I leakage [µA] 0,29
Write into ROOT file No / Yes

This test is feasible only with a DEPP board

10,00 µA Maximum of allowed Current
40,00 2nd max)
Min. Voltage 0,00 V
Max. Voltage 500,00 V
Final voltage 500,00 V
No. of steps 10
Wait 5 sec at each voltage step
Wait 5 sec at max. Voltage before ramping to final voltage
500 recent Voltage
0,29 recent Current
0 sec to wait

IV Data from Files "IV_Sensor_XXX.txt" and IV_Measured_XXX.txt" (XXX: Module ID) can be written into the ROOT file instead of and additional to the DEPP

ready without over current

from Sensor Measurement

8
0

V	µA
0,00	0,00
0,00	0,00
0,00	0,00
0,00	0,00
0,00	0,00
0,00	0,00
0,00	0,00

from Module Measurement

0
0

V	µA
0,00	0,05
50,00	0,20
100,00	0,23
150,00	0,25
200,00	0,26
250,00	0,27
300,00	0,28

An easy but important test, is the recording of a current - voltage graph. It does not give any information on a per channel level, but shows problems in the HV supply line on the module, or in the silicon itself. Usually the IV curve should resemble typical reverse bias diode characteristics.

The most important parameter is the current at 450V which is the only measurement used for the automatic fault detection algorithm. Modules with more than 10μA leakage current are grade C (see table 5)

Other Tests Additional test are already implemented in ARCS 7.1 and some more may be incorporated in future versions. These tests will not be used for the automatic bad channel tagging, but may prove to be useful for a closer inspection of problematic modules.

5.3 Additional Software

Certain additional software was used to either overcome current limitations of the available software, or to automatise recurring tasks. These tools are subject to change frequently.

5.3.1 The xFLAG macro

Due to problems in the XML file generator of ARCS prior to version 7.2, a separate tool had to be used to generate the XML files for TrackerDB insertion. The usage of xFLAG tended to be cumbersome, as only precompiled binarys for selected environments where available. Still it was the preferred tool recommended for the creation of XML files to insert them into TrackerDB.

The version used was xFLAG V1.5.1 and can be downloaded at http://hep.fi.infn.it/CMS/marchett/xFLAG/.

The tool is based on some root analysis macros found at http://hep.fi.infn.it/CMS/marchett/files/arcs_macro_6_1.cc

xFLAG uses the root files that ARCS is generating during the module tests to analyse the data and create the XML files. A text file describes the bad channels found by the software.

The original root macro is also used to generate some nice plots and protocols. Although not required, these plots represent an easy and quick way to analyse the test results.

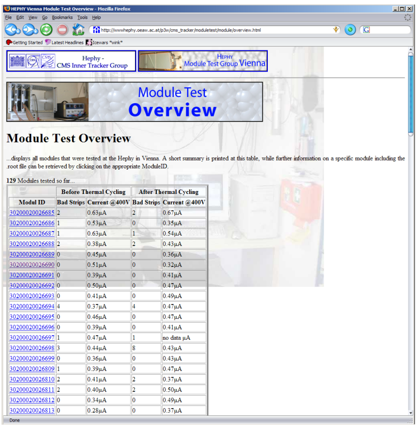

Module Test Overview

...displays all modules that were tested at the Hephy in Vienna. A short summary is printed at this table, while further information on a specific module including the .root file can be retrieved by clicking on the appropriate ModuleID.

129 Modules tested so far...

	Before Thermal Cycling		After Thermal Cycling	
Modul ID	**Bad Strips**	**Current @400V**	**Bad Strips**	**Current @400V**
30200020026685	2	0.63µA	2	0.67µA
30200020026686	1	0.53µA	0	0.35µA
30200020026687	1	0.63µA	1	0.54µA
30200020026688	2	0.38µA	2	0.43µA
30200020026689	0	0.45µA	0	0.36µA
30200020026690	0	0.51µA	0	0.32µA
30200020026691	0	0.39µA	0	0.41µA
30200020026692	0	0.50µA	0	0.47µA
30200020026693	0	0.41µA	0	0.49µA
30200020026694	4	0.37µA	4	0.47µA
30200020026695	0	0.46µA	0	0.47µA
30200020026696	0	0.39µA	0	0.41µA
30200020026697	1	0.47µA	1	no data µA
30200020026698	3	0.44µA	8	0.43µA
30200020026699	0	0.36µA	0	0.43µA
30200020026809	1	0.39µA	0	0.47µA
30200020026810	2	0.41µA	2	0.37µA
30200020026811	2	0.40µA	2	0.50µA
30200020026812	0	0.34µA	0	0.49µA
30200020026813	0	0.28µA	0	0.37µA

Figure 50: The Module Test Webpage - Overview.

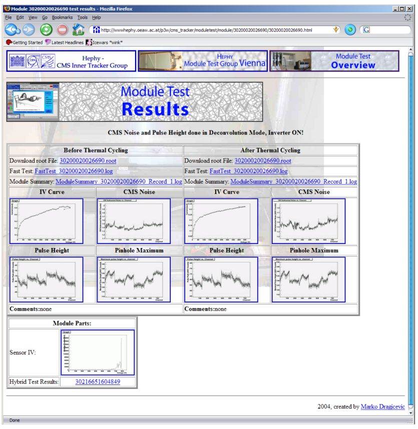

CMS Noise and Pulse Height done in Deconvolution Mode, Inverter ON!

Before Thermal Cycling		After Thermal Cycling	
Download root File: 30200020026690.root		Download root File: 30200020026690.root	
Fast Test: FastTest_30200020026690.log		Fast Test: FastTest_30200020026690.log	
Module Summary: ModuleSummary_30200020026690_Record_1.log		Module Summary: ModuleSummary_30200020026690_Record_1.log	
IV Curve	**CMS Noise**	**IV Curve**	**CMS Noise**
Pulse Height	**Pinhole Maximum**	**Pulse Height**	**Pinhole Maximum**
Comments:none		**Comments:**none	

Module Parts:	
Sensor IV:	
Hybrid Test Results:	30216651604849

2004, created by Marko Dragicevic

Figure 51: The Module Test Webpage - Detail.

5.3.2 The Module Test Webpage Macros

The ARCS test results are written into 3 files: a root file containing all test data, one text file with the results of the fast test and another one showing an overall bad channel report. These files are stored and for safety reasons a backup should be made. Furthermore, it is a good idea to make the test data available to other institutes as well, so all data is copied to a web server, where, as a bonus, the backup is already done on a regular basis.

To make the data easily accessible, some macros have been written to do the copying and the creation of the web pages automatically (see fig. 50 and fig. 51). A separate page for module tests and hybrid tests was made. They take care of several task:

- Generation of plots from the root files created by ARCS which will then be used as a quick overview of test data on the web
- Generation of the html files displaying the plots, comments and links to all the test data.
- Generation of a html overview page, with a short glimpse on the most important data of all tested modules.
- Copying all the necessary files to the web server.

The module and hybrid test result pages can be accessed at
http://wwwhephy.oeaw.ac.at/p3w/cms_tracker/moduletest/.

5.4 Calibration Campaign

As was already mentioned earlier, the test boxes were developed by each institute individually, but the shielding and grounding of the modules tends to be very delicate and has a great amount of influence on certain test results. Therefore a calibration campaign was started to ensure that all test systems show similar behaviour.

This was done by using a single test module, with some artificially created defects, for tests at each lab. The shielding capabilities of the test boxes and the grounding scheme was tuned until all systems showed a similar maximum CM noise behaviour. This made sure that at each lab the same bad channels on the test module were found, and all future test should be comparable among different test systems.

5.5 Production Results

So far around 120 modules have been tested. No major problems have been found. Some smaller or already fixed problems have been:

- A lack of pressure on the HV backplane connection during the module assembly, made the connection become loose. The problem was fixed by introducing a slightly higher pedestal, which gave a little more pressure on the splice.
- Many more pinholes where found during the module tests than during the tests made by the manufacturer Hamamatsu. It is believed that the old bonding machine used for the production in 2004 created these pinholes. Nevertheless, the number of Pinholes found is still neglectible. From 119 built modules (91392 channels) only 23 Pinholes were found (thats 0,025% of the the total channels).
- Some modules were found to have lots of noisy channels. The test data already looked quite inconclusive and it was believed to be rather a software problem than a faulty module. Later this assumption proofed to be true, when the VPSP register was found to be the problem. This register is controlling the initial zero point offset of the APV. By setting them to high, the pedestals on some channels were running into saturation which showed up as increased noise.

Statistics Until the end of 2004, 119 modules were built, which were foreseen to be integrated into the Tracker. A few modules were built for test purposes like calibrating the new bonding machine or doing sensor recuperation attempts[26]

From these 119 modules only 2 modules proved to be faulty beyond repair. Both had problems attributed to the I-V test. For one module the problem is identified as a bad HV connection to the sensor backplane. This is an already known issue which became apparent in 2005. The conducting two-component glue which fixes the HV connection to the backplane shows unacceptably high transition resistivity on a number of modules (a few percent). Alteration to the glueing sceme are currently discussed to resolve the issue. So even this module might be repaired, while the second one experienced an breakdown at 360 V which might be attributed to a damaged sensor and be beyond repair.

Another important issue is not reflected in any of the test results. Certain batches of hybrids are believed to have a major design flaw, which would render them inoperable after an extended period of operation. It was decided to discard all hybrids from these suspicious batches. The status of modules that were

---

[26] The sensor was removed from the carbon frame to be reused on a new module. The procedure proved to be successful and therefore it is possible to recuperate sensors from damaged modules (bad hybrids or broken frames, etc.).

	good	faulty			bad batch
		$> 2\%$ bad channels	bad IV	other	
R2N	63	0	1	0	6
R2S	56	0	1	0	18
Total	119	0	2	0	24

Bonded Channels	91392
Bad Channels	96
% bad	0,16

Table 6: ARCS Module Test Statistics. The *bad batch* column depicts modules which were built with a hybrid from a batches which was declared as suspicious after assembly. Nevertheless, all of these modules passed the ARC test. The smaller tables gives numbers on a per channel view.

already built with such hybrids, were all set to faulty although they were passing the ARC test.

Table 6 shows some more interesting statistics on the ARCS module test.

6 Microdischarge Measurements

Quality assurance procedures are usually defined long before the actual production starts. Certain parameters that seem crucial when issuing contracts to manufactures, may proof to be quite unproblematic later or always well within the capabilities of the manufacturer. In contrast it is also often unavoidable, that problems are detected during the production phase. This may make changes in the stipulated parameters necessary or even new tests have to be defined to prevent jeopardising the whole production.

One such problem arose in the sensor community, when the so called *common mode problem* was first reported.

6.1 Motivation

Already in 2003, a problem in modules built by the *University of California, Santa Barbara* (UCSB) and *Fermi National Accelerator Laboratory* in the United States were experienced, but with modules containing STMicroelectronics sensors only.

The symptoms of these problematic sensors included:

- Higher leakage current is seen than what was reported by the QTC measurements. At more detailed measurements the additional current can usually be attributed to a single strip.
- Channels with high noise are seen. Oddly enough these noisy strips do only turn up at a certain minimum voltage. This *set in voltage* corresponds to the beginning of the deviations of the IV curve reported in the previous item. The noisy channel is usually the one experiencing the increased leakage current also described in the previous item.
- The CM noise correction is driven up for the complete APV containing the noisy strip.

The problem was commonly called *CM Noise Problem* as the problematic modules were typically found by the significantly increased CM noise in the ARC tests. This usually resulted in a high number of noisy channels on a single APV, often rendering the channels of the whole chip noisy.

Several discussions about possible explanations of the problem arose. A very promising cause that was proposed, are *Micro Discharges* (MD) inside silicon. Due to localised field peaks caused by inhomogenities in the sensor bulk and the surface, charge breakdowns can happen in the affected region. These small discharges subside very quickly but the high field configuration is still there.

The current induced by the discharges could explain the increased leakage current seen on single strips. The increased noise the APVs are seeing could be attributed to the fast and reoccuring time behaviour. Additionally this would put an undesired additional load on the APV's preamps which could also explain the failure of the CM correction. On some modules the CM noise problem drove the affected APV into malfunctioning.

To prove the MD assumption, a special test setup was proposed to conduct measurements on the time structure of the leakage current of affected strips.

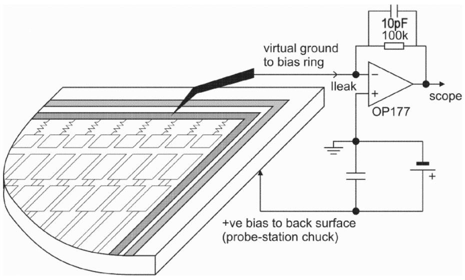

Figure 52: Connection scheme

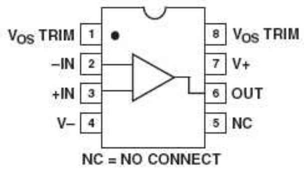

Figure 53: Analog Devices OP177 connection scheme

6.2 The Test Setup

At first the measurement of the leakage current of single strips was tried. This proved to be very delicate and impractical. So a different method was proposed, which proved to be much simpler to realise: the leakage current was not measured on a single strip, but the bias current of the detector was monitored. It should still be possible to detect the discharges happening on the bad strip, as they should be far bigger than the usual noise produced by the remaining good strips or any fluctuations of the HV supply itself.

The positive HV is applied to the backplane of the sensor, while the bias ring is connected to the negative input of the amplifier circuit. That way, the amplifier acts as ground connection on the bias ring, and converts current to voltage, which can then be measured via the scope on the output of the circuit. See fig. 52 for a detailed scheme of the measuring principle and fig. 53 for the pin layout of the operational amplifier used in the circuit. A small low pass filter made of two resistors and a 10nF capacitor put between + and - of the high voltage, should stabilize the power supply.

The simple circuit board is pictured in fig. 54. The design is quite simple and straightforward but sufficient for the intended purpose. The 5 connectors are (from top to bottom):

- Output connector to the scope
- Ground connection
- Red DC power supply for the amplifier (-)
- Blue/Black DC power supply for the amplifier (+)
- Input connection to the needle contacting the bias line

The most critical point is to make the input connection to the needle as short as possible. A 4 cm LEMO cable was used to make the connection.

The board is simply fixed with adhesive tape to the needle tool as can be seen in fig. 55. The picture shows the basic layout of the box used to measure the sensors. On the right half you can see the aluminium carrier plate which holds the sensor. It is isolated from the surrounding shielding box, as it is mounted on two thick pieces of plastic. The positive HV is applied to the carrier plate.

The black cables are ground connections for the DC power supply and the HV supply which are all connected to a terminal inside the box. A common

Figure 54: The amplifier circuit board

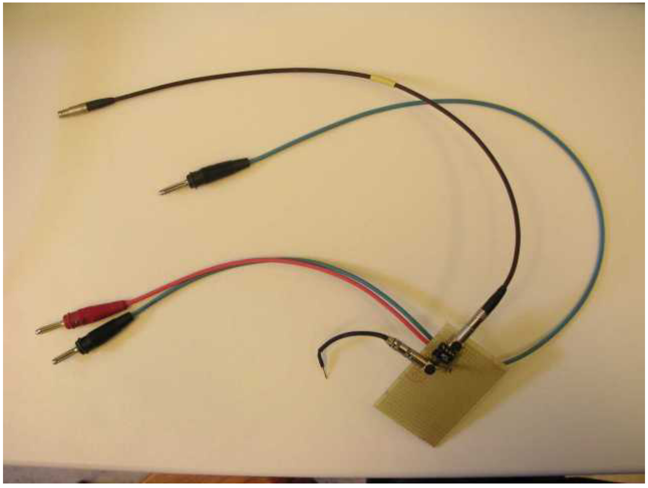

grounding terminal is quite essential to prevent ground loops and bad noise influence on the circuit.

Fig. 56 shows how the silicon sensor is placed on a piece of conductive rubber to supply the positive HV from the carrier plate to the backplane. In the lower right corner the needle is contacting the bias ring to connect it to the amplifier circuit.

For the actual measuring, the box had to be light tight of course. It also serves as a faraday cage to shield it from stray pick-up.

A connection terminal at the box provides access to the electronics inside. In fig. 57 the connected devices can be seen. They consist of:

- Source Measure Unit supplying and measuring High Voltage and DC current (Keithley 237)
- Digital Oscilloscope (Tektronix TDS3054B)
- Laboratory DC Power Supply (±5V for the Amp circuit)

6.3 Results

The measured ST sensors showed quite an unstable and varying behaviour. Some sensors had significantly increased current immediately after ramping up the HV, but the current settled down after a few minutes of biasing (see fig. 58. This was seen very frequently and the high current was accompanied by fluctuations which usually subside when the leakage current has stabilised. These ramp up fluctuations/high current where ignored and data takeing was only done after a few minutes, when the sensor had already settled.

It seemed like the biasing of the sensor up to a voltage of around 550 V changed some of the internal properties of the silicon. This is especially true for sensors drawing an increased current of more than 2 μA.

Figure 55: Top view of the box

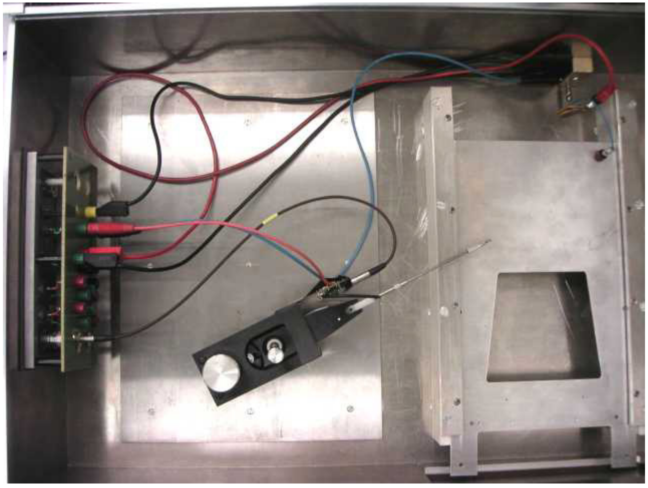

Figure 56: Connected sensor seen from above

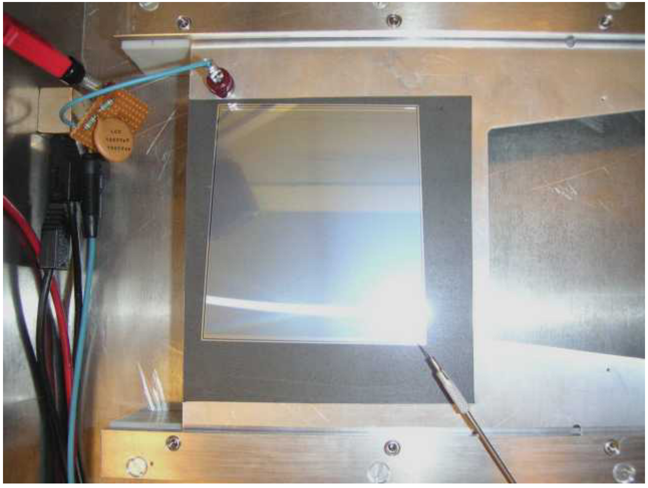

Figure 57: View of the setup

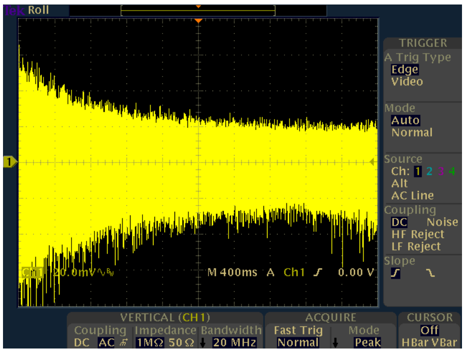

Figure 58: A situation seen frequently on the scope: current and fluctuations are high shortly after applying the HV. Subsides quickly but ususally does not get completely stable (Sensor ID:30211334091219)

Changes in the sensor properties occurred on a larger timescale as well. Some sensors never showed the same IV behaviour when measured multiple times. Total leakage current and amount of fluctuations were different when testing certain sensors on different days. The variations in leakage current where verified by measuring the sensors in the QTC setup again.

Two characteristics in the time behaviour of the leakage current had been observed. Some sensors showed an *increased noise* (see fig. 59) which might be attributed to fast recurring discharges, while large current fluctuations on a timescale of seconds (see fig. 60) might be attributed to even more sever problems in the detector bulk.

A clear evidence supporting the MD hypothesis could not be found, nor was a direct link connecting noisy or fluctuating bias current and the CM noise problem confirmed. Nevertheless, certain ST sensors did show unstable bias current with fluctuations on a scale that would definitely influence the APVs in an unpredictable manner. These fluctuations became more probable for a sensor drawing an increased leakage current.

Due to the randomness of the phenomena it was not possible to develop a reliable QA procedure based on a cut on a simple measurement, which is able to find bad sensors with high current fluctuations or noise. Nevertheless it was possible to minimize the probability of producing a module with *common mode* problems, by selecting sensors with low leakage current (¡ 2 μA).

Interestingly enough, after presenting the results of these studies to the manufacturer, the quality of the sensors concerning the scope of these measurements, increased significantly. Still they claim not to have changed the manufacturing process.

A comparison of randomly selected sensors from batches produced before and after the ”improvement” is seen in fig. 6.3. The histogram clearly shows a major improvement in current stability.

So, although the MD measurements were not able to clearly identify and explain the problem, they did point to a severe problem that existed in sensors produced by STMicroelectronics in Catania. It led to a more stringent selection of sensors on basis of the overall leakage current (¡ 2 μA). Additionally, despite the claims of the manufacturer that the manufacturing process had not been

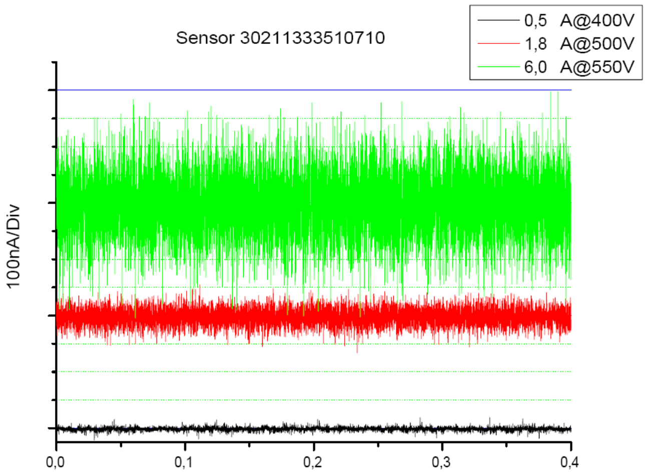

Figure 59: Noise on the bias line of a sensor. A "good" sensor would show a straight line. The noise at 550 is in the order of several 100 nA where the total leakage current for a good sensor should be below 2000 nA! Different colors represent different bias voltages. (Sensor ID:30211333510710)

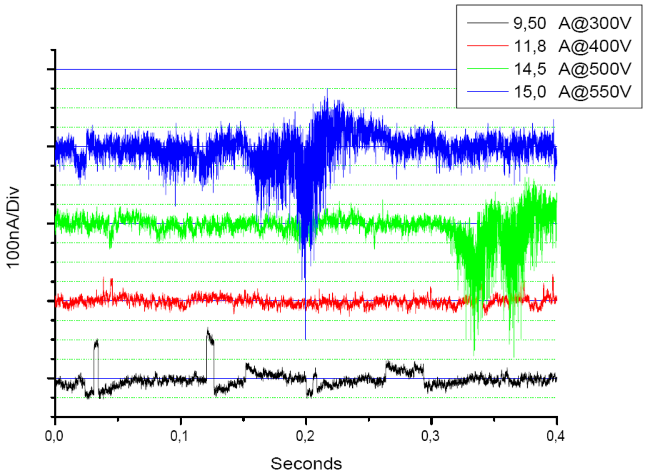

Figure 60: Noise and fluctuations on the bias line of a sensor. A good sensor would show a flat line. The total leakage current of a good sensor is usually around 2 μA where the fluctuations reach a maximum of around 1 μA for this sensor. (Sensor ID: 30211333711008)

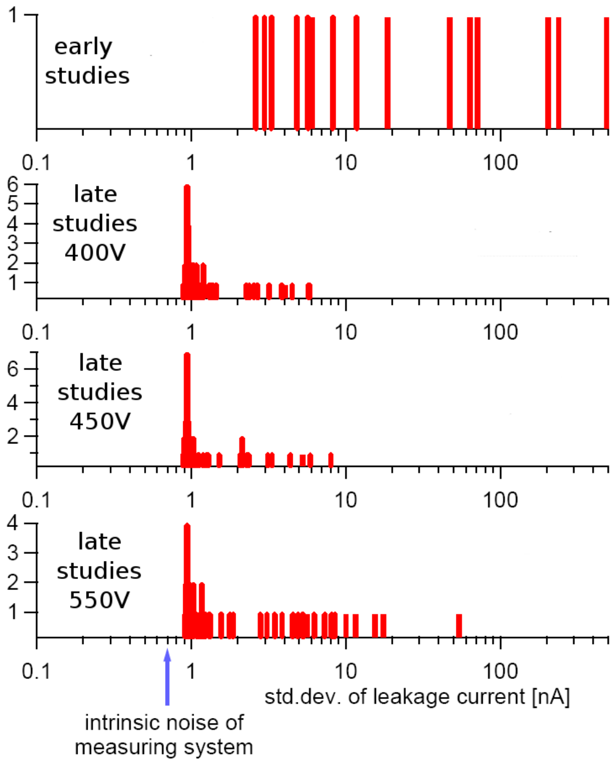

Figure 61: Histogram of the standard deviation of 50.000 points per sensor measured. For the earlier studies, different bias voltages had to be used, as not all of the sensor could reach the desired voltages.

altered, a significant improvement was seen in our measurements with newer batches, which rendered the matter solved.

Nevertheless, when issuing contracts and the accompanying QA procedures to a manufacturer, the MD matter should be considered again.

ModuleID	Type	Irradiation (1 MeV neutron equiv.)	Tests Done
30200020005207	OB1	0.65×10^{14}	all + XY scan
30200020005211	OB1	0.1×10^{14}	all
30200020005208	OB1	0.29×10^{14}	all
30200020005275	OB1	none	all + XY scan
30200020005217	OB2	0.1×10^{14}	all
30200020005222	OB2	0.28×10^{14}	all
30200020005223	OB2	none	all
30200020020561	W5	0.58×10^{14}	pedestal only
30200020020531	W5	0.28×10^{14}	none
30200020027536	W5	none	all
30200020020532	W5	none	all
30200020027045	W3	none	XY scan

Table 7: Modules used for the CMS Tracker DESY 22/04 Testbeam.

7 The DESY 22/04 Testbeam

Thorough research, careful production and efficient QA procedures are the most import points when developing new detectors or any sophisticated tools. Nevertheless, at a certain point it is essential to proof if the predictions, theoretical models and the quality of the product can fulfil the demands that originally led to the present designs. Such a test run of the equipment in an "almost real" environment must be made - and as soon as possible.

The CMS Tracker DESY 22/04 Testbeam was done from the 26.10.2004 to 5.12.2004 at the testbeam 22 facility of the DESY research facility.

7.1 Motivation

Before going into full production, a test beam was scheduled to see if the detectors are performing up to their expectations. It was especially interesting to see how irradiated modules are performing and therefore this was the main focus.

For the tests we have selected modules from three different geometries. For each geometry 3 different irradiation levels should be provided but unfortunately we did not have the irradiated modules for all the desired fluences available. An additional, non irradiated W3 module was used for a XY scan. The irradiation covered the complete module including all the readout electronics on the hybrid. Table 7 is a complete list of all modules measured during the testbeam.

The irradiated modules required special treatment. They have to be kept at temperatures below 0°C to eliminate any reverse annealing effects. Only for very short periods, when changing the test module for example, may they be exposed to room temperature as reverse annealing will change the module propertie within a few hours to a couple of days.

7.2 The DESY Testbeam 22

The testbeam was done at the *Deutsches Elektronen SYnchrotron* in Hamburg, Germany. Information on the testbeam 22 installation that was used for the

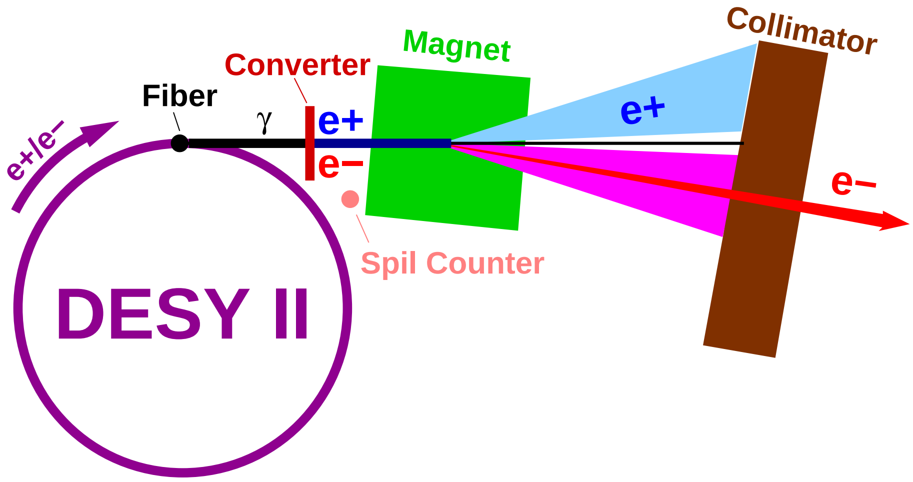

Figure 62: Schematic layout of the DESY testbeams.

measurements can be found at http://adweb.desy.de/˜testbeam/.

The schematic layout of testbeams 21,22 and 24 can be seen in fig. 62. An electron/positron beam is generated by dumping the DESY II e^+/e^- beam into a fibre target, where a photon beam is generated by bremsstrahlung. The photon beam is then converted to e^+/e^- pairs by a metal plate. A dipole magnet is spreading the beam horizontally and a collimator is finally selecting a small cut of the beam. By adjusting the magnet's field the beam momentum can be selected.

The timing of the beam is somewhat peculiar. Typically the beam spill takes 40 ms followed by a pause of 160 ms. The clock signal is gone during the pause. This created some problems when setting up the clock and trigger logic, as the pause had to be filled with a somewhat slower extra clock, which created some jitter when the DESY clock came back. The problem was solved by cutting of the first few cycles after the clock restart. This further reduced our trigger rate and in the end it was quite low at less than 10Hz.

The preinstalled telescope consists of 6 silicon strip detectors with a pitch of 25 μm. Three are measuring the X and three Y coordinates. Two scintillators are used for trigger information. The telescope is operated by a computer running a real time operating system storing the acquired data on harddisk.

A motor controlled mounting point provides the possibility to move the test target in X,Y coordinates and rotate it around the X axis.

7.3 Test Equipment

Two important decisions had to be made concerning additional equipment:

- A box for the test module had to be constructed. It should provide a light tight environment for the used module geometries. It must be possible to cool the inside of the box, nevertheless the modules should be easy

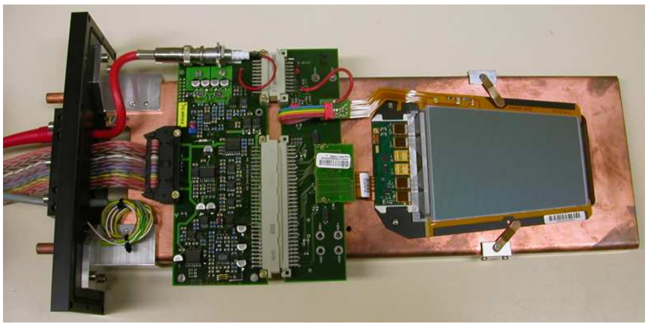

Figure 63: Inside view of the testbeam box with a module already mounted. On the left side the red HV cable, the flatband readout cable and the gray cable for the temperature sensor can be seen.

and fast to change. Finally, the box must be integrated into the already existing mounting at the testbeam.

- A suitable readout system must be found. It should be able to accept trigger and clock information from the beam telescope and the DESY clock. The system should be easy and quick to setup to avoid wasting to much time on calibrating the readout. Some basic data analysis should exist to see if the modules are operating correctly.

Testbeam Box A custom made testbeam box has been designed. It had to enclose not only the module but the FE adapter of the ARC system as well (see next paragraph on the selected readout system). The cables for the readout, the HV supply and a temperature sensor had to be incorporated into the box as well.

A massive piece of copper served as the mounting platform. Copper was chosen due to its good thermal conduction which is necessary to ensure stable temperature conditions for the module. The cooling pipe was mounted directly below the copper plate. See fig. 63.

The cover of the box is made of thick plastic with a large beamwindow. It is sealed with 8 allen screws which can be spotted on the far left side. The blue pipe is the feed line for the nitrogen to flush the inside and keep it at low relative humidity. See fig 64.

Readout System The lack of available options made the decisions quite easy. The well known ARC system including the ARCS testing software was chosen as readout system. Although designed as testing system, it offers some basic data taking capabilities. Only minor changes had to be implemented to accept external clock and trigger signals in the software.

The system offered the possibility to alter all necessary settings of the APVs and it incorporated some very basic data display capabilities, nevertheless it proofed to be quite slow and a little unstable. The raw analogue data read from the APVs was saved in simple coma separated text files, including a timestamp for each sample.

Still it was necessary to have some more data analysis capabilities to check the data for basic consistency. Therefore some small analysis macros have been

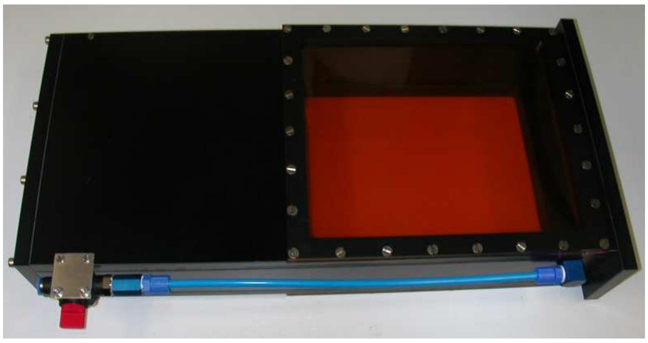

Figure 64: The closed testbeam box. The nitrogen feed line is visible and the large window is not yet covered with a light tight foil.

	Events	Telescope		Parameters
Latency Scan	3 kEv	no	peak	find best latency
			dec	find best latency
Pedestal Run	10 kEv	no	peak	for ”online” data analysis
			dec	for ”online” data analysis
Voltage Scan	5 kEv	no	peak	400 V
			dec	50 V, 100 V, 200 V, 300 V, 400 V, 550 V, knee in 50 V steps
Energy Scan	10 kEv	yes	peak	3 GeV, 6 GeV
			dec	1.6 GeV, 3 GeV, 4.6 GeV, 6 GeV
Angle Scan	10k Ev	yes	peak	20°, 40°, 60°
			dec	10°, 20°, 30°, 40°, 50°, 60°, -40°, -60°
Temperature Scan	5 kEv	no	peak	-15°C, -20°C, -10°C
			dec	-15°C, -20°C, -10°C
XY Scan	20-50 kEv	yes	peak	Pos 1,2,3,4,5
			dec	

Table 8: The DESY 22/04 testbeam program. For a description of the XY Scan positions see fig. 65

written in ROOT. They perform pedestal and common mode corrections and show a very simple event display to spot bad channels. Furthermore a signal height histogram is plotted to see if the data follows the predicted landau distribution. Any deviations point to possible problems of the setup or a dirty beam.

7.4 Performed Measurements

Several measurements were performed for each module, gathering a couple of gigabytes of data. Some measurements, in particular the XY scan, were not done on all modules due to time constraints and two W5 modules refused to work at -15°. Table 8 shows the categories of measurements that were done.

Each of the measurements was designated to reveal certain detector properties:

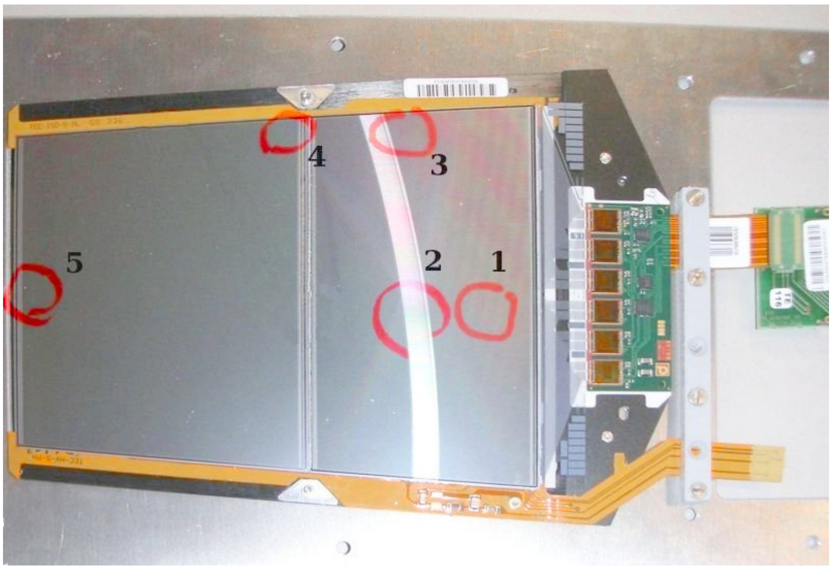

Figure 65: Approximate location of the five XY scan measurements.

Latency Scan The signal received from an event has certain rise times. So the *measured* signal height does not only depend on incidents particles deposited energy, but also from the exact point in time when the signal height is measured. This can be controlled by the *latency setting*. The intention is to read the signal at the highest possible point to get the best S/N ratios. The optimal latency setting depends on the module geometry and should be quite similar for the same module types.

It is obvious that the latency calibration must be done prior to any other measurements.

Pedestal Run The ”online” consistency check of the data basically plots the signal heights, which should follow a Landau distribution. The small ROOT macro requires separate ”noise only” runs to calculate the pedestals. In the actual analysis this will be derived from each run, but for simplicity, this was not yet implemented for this simple consistency check.

Voltage Scan The S/N ratio should change with the depletion of the detector bulk. When reaching full depletion, S/N should reach a plateau as well. Therefore this measurement should provide the full depletion voltage of the detector.

Energy Scan It is quite interesting to see S/N ratio and the resolution for particles with different energies. In theory both parameters are dependable on the particles energy, as the energy deposit in the detector changes according to eq. 6 (see also fig. 11). But for the energy range of electrons that we had available at the testbeam (1.6 GeV to 6 GeV) no change should be evident (see also remarks in section 7.6.1).

Angle Scan Varying the incident angle has an effect on the S/N ratio, as the detector ”thickness” that the traversing particle ”sees” changes and a different amount of energy is deposited in the detector bulk. Additionally some simple geometrical considerations show, that a different number of strips will be hit by the deposited charge and therefore the cluster width should change accrodingly. Telescope data was taken as well to study the influence on the detector resolution.

Temperature Scan The temperature influence on the detectors was measured, which is especially interesting for irradiated modules. The heavily irradiated modules require low temperature environment to work at all, otherwise the leakage current would get to high.

XY Scan The S/N and position resolution is expected to be uniform over the whole active detector area. For three modules certain crucial positions were measured to reassure the expectations. These locations include the sensor corner and the gap between two sensors, see fig. 65.

7.5 Analysis

Analysis of the data collected during the testbeam was approached in two different attempts. Considerable effort was invested in the attempt to use the official *CMS/Tracker Testbeam Software* [6]. Unfortunately this approach proofed to be unsuccessful. Although promissing at first, the testbeam software did not turn out to be easily adaptable to our needs. After many painstaking weeks of remedying bugs and incompatibilities caused by a switch between two versions of the *ORCA*[27] framework, it was still not clear if the testbeam software would ever be cappble of running the desired analysis on our data.

At last, it was decided to abandon the attempt on integrating the testbeam software and all efforts were put in a different approach to analyse the data. A custom made software was specifically written for the data collected at the DESY 22/04 testbeam. It is implemented in *ROOT* [8], which is basically a C++ like framework which offers a macro interpreter for easy development and many physics analysis specific classes. It enables the fast and easy creation of various plots and histograms. It is also well documented and fairly stable and reliable.

7.5.1 The ROOT Analysis Code

The software developed for the analysis is split into 3 different parts:

AnalyseData Is processing the raw data, which was written by ARCS. It reads the ASCII data files, applies pedestal subtraction and common mode correction. A few plots are generated to visualize the results and they are saved in a *.root* file. Fig. 66 shows a sample output of the macro.

The macro exists in two versions, one for data from 6 APV modules and the other for 4 APV modules.

BeamData Is doing the actual analysis which in the end results in a Signal-to-Noise histogram (see example in fig. 67). The histogram is fitted with

---

[27] *Object-oriented Reconstruction for CMS Analysis.* A C++ framework for the online and offline analysis of CMS data. Currently under heavy development and unfortunately not very well documented in the current status. See [7]

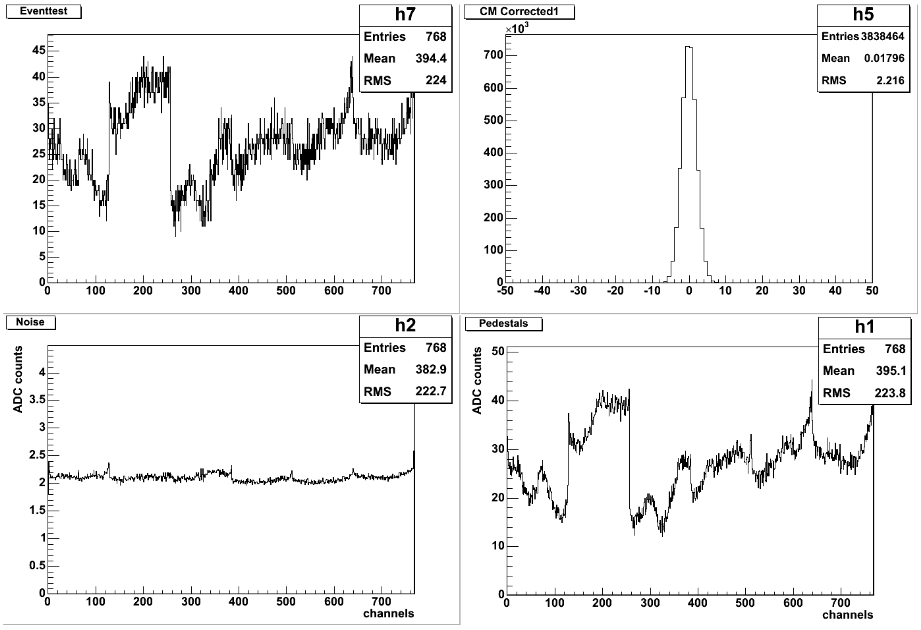

Figure 66: Output of the *AnalyseData* macro. Only the 4 most important plots are shown. In *Eventtest* a single event is shown (can be selected by modifying a variable in the source code) and *CMS corrected* is a histogram of the noise after Pedestal and CM correction. Noise depicts the average *Noise* of the module, *Pedestal* shows the calculated pedestals. Data is taken from a pedestal run and therefore does not contain any signal.

a Landau distribution:

$$f(x) = \frac{1}{2\pi i}\int_{c-i\infty}^{c+i\infty} \exp(xu + u\ln(u))\mathrm{d}u, \tag{18}$$

where c and u are the fit parameters. The *Most Probable Value* (MPV) is then considered as the signal to noise ratio. Before that, noise flagging and cluster finding algorithms are processing the data.

This macro exists in two versions as well, one for data from 6 APV modules and the other for 4 APV modules.

MultiAna Is just a wrapper around the previous two macros. It enables the batch analysis of several data files at once. As the macro plots the calculated S/N ratio for each analysed file over a selectable value (depletion voltage, temperature, angle, particle energy), it should always be fed with a set of related data. An example result is seen in fig. 68.

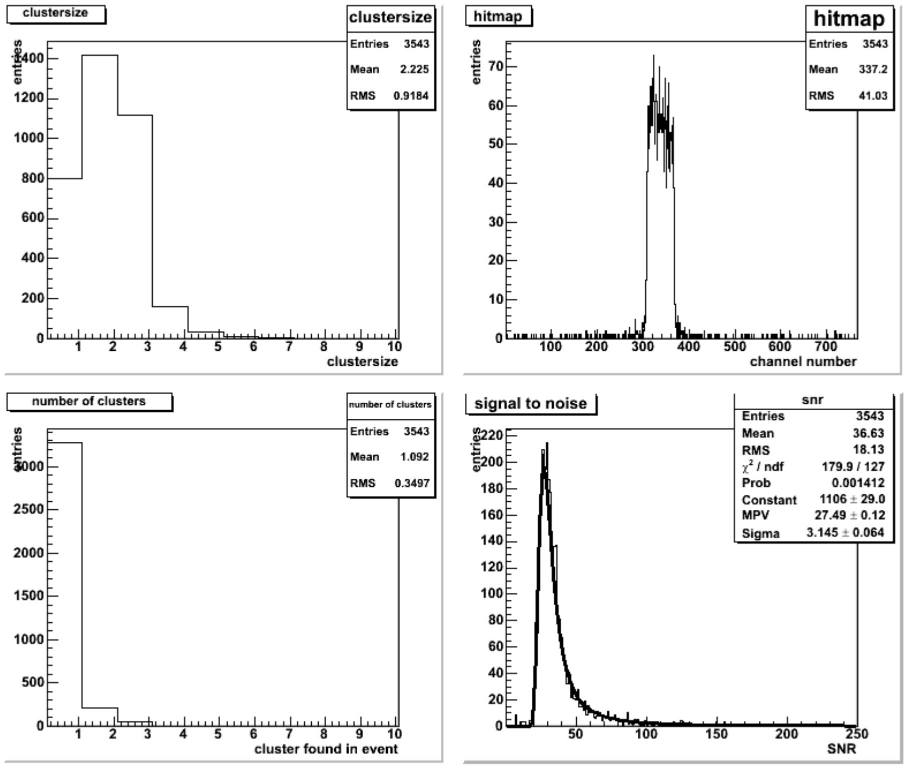

Figure 67: Output of the *BeamData* macro. The left plots show the clustersize and the number of clusters found per event, while the right plots show a nice hitmap and, most importantly, a signal to noise plot.

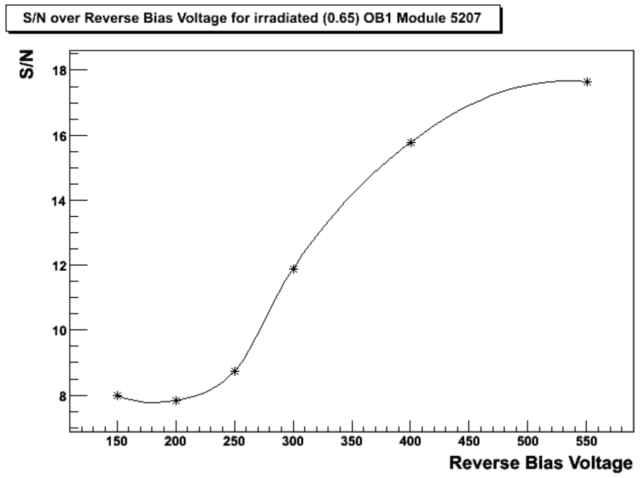

Figure 68: Output of the *MultiAna* macro.

Location	S/N
1	21
2	21.6
3	21.3
4	20
5	19

Table 9: Table showing the S/N at different locations on the silicon sensor. See fig. 65 for a picture of the individual locations. (Module 05207, Type OB1, Irradiation: 0.65 × 10^14 1 MeV neutron equivalent ≡ 10 years of LHC)

7.6 Results

The careful analysis of the testbeam data was lead by the demand to show, that the performance requirements of the silicon detector modules are met even after experiencing 10 years of LHC environment. During this time period, the modules are exposed to heavy radiation and therefore will gather a significant amount of defects in the silicon (see section 3.2). Nevertheless they should still be in perfect working condition and provide a S/N of at least 12/1. To give evidence to that, we have compiled several plots of modules which have accumulated different levels of irradiation. These graphs show the S/N as a function of the reverse bias voltage. The increase of the depletion voltage[28] should be evident in the graphs as well.

But first, we will show, that the readout and analysis chain of the testbeam was working as expected to justify our results. This is done by including several measurements of well known silicon detector features:

Stable S/N over the whole active detector area. The detector ought to be capable of providing the same S/N over the whole area. Edge effects should only have a very marginal influence on the performance which are below, the error in measurement.

S/N for different particle energy. The S/N of the detector should be depending on the incident particle energy according to equation 6 in section 3.1.1. We had a range of 1.6 GeV to 6 GeV electrons available and the difference in deposited energy is only marginal (see fig. 69).

7.6.1 Consistency Checks

As already described above, we will show two measurements to check the consistency of our readout and analysis chain.

Geometrical Consistency The first part will show that our scans are geometrically stable over the whole active detector region. Thanks to the well crafted design, any edge effects should be negligible and therefore the same S/N for different locations should be measured as table 9 proves.

There is no significant deviation in S/N over the detector area, except for location 5, which is situated on the far sensor. Here the signal has to travel

---

[28] Due to increase of charge carriers and holes in the silicon caused by radiation, a higher voltage is necessary to deplete the sensitive detector area.

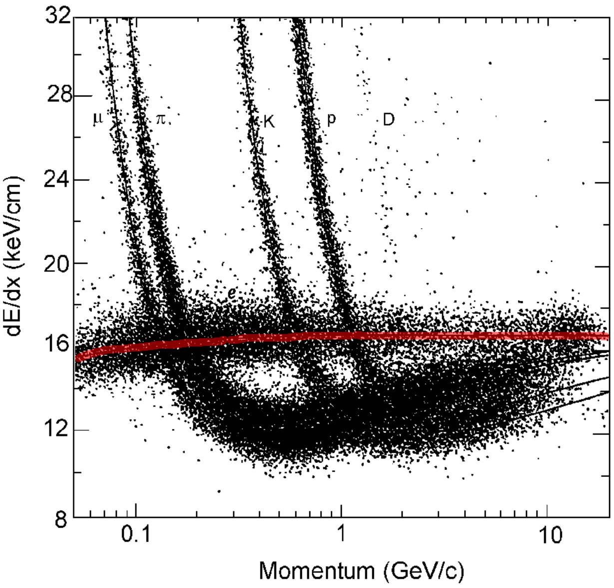

Figure 69: Energy loss measurements for different particles. The theoretical prediction for electrons is marked in red. [9]

along both sensors and the interconnecting bonds, which results in a somewhat higher strip resistance, which in turn decreases the S/N.

Nevertheless, the results show a stable S/N over the active detector region as expected.

Energetic Consistency Now we will show, that the S/N response of the modules is as expected from the theoretical calculations derived in section 3.1.1. For the energy range of the beam (1.6 GeV to 6 GeV) no energy dependence is expected (see fig. 69).

In fig. 70 we have plotted several modules. It shows that there is no evident dependence of S/N on particle energy. Some more interesting information is hidden in this graph as well. The modules shown in the plot have all accumulated different levels of irradiation from none to the full 10 years of LHC lifetime. Nevertheless they do all show a S/N of 16 - 18 while being operated at a reverse bias voltage of 400 V. This already suggests, that the modules are capable of operating within specs, after exposure to 10 years of LHC environment when operated at a minimum of 400 V.

7.6.2 S/N and Irradiated Modules

The most interesting question of the testbeam analysis was, whether the detectors are still capable of operating with the required S/N after experiencing 10 years of LHC lifetime. According to [10] the expected irradiation after 10 years of LHC is 0.35×10^{14} neutrons (1 MeV) per square cm for the outer barrel (see fig. 5). Keeping in mind a safety factor of at least 1.5, the maximum irradiation experienced by the tested modules (OB1 module 05207 with 0.65×10^{14}) is comparable to 10 years of LHC environment.

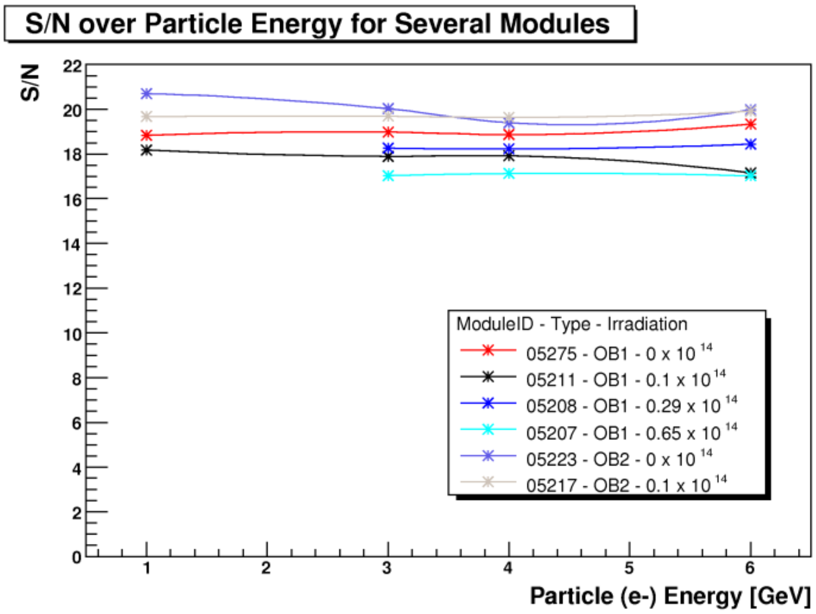

Figure 70: S/N as a function of incident energy particle for several OB1 and OB2 modules. Keep in mind that these modules experienced different levels of irradiation and they are all operated at the same reverse bias voltage of 400 V

Undoubtedly, it might be necessary to increase the reverse bias voltage over the years, to make sure the silicon is depleted. Nevertheless, certain constraints limit the maximum voltage that can be applied to the modules:

- Voltage stability of the silicon and the module components
- Current and voltage limitations of the power supplies
- Limitations of the cooling capabilities

In practice, the reverse bias voltage may not exceed a maximum of 500 V, where a module should still provide a S/N of more than 12 to contribute to the tracker analysis in a reasonable way.

We have plotted the *S/N over reverse bias voltage* for a series of modules from the same geometry (OB1 - see fig. 71 and OB2 - see fig. 71) but different irradiation levels.

Due to some irregularities in the noise behaviour of the modules during measurement (remember: the readout was done with the ARC system which is basically a test system and not intentionally made for module readout during testbeams) we additionally added the same plots for *signal over reverse bias voltage* as well (OB1 - see fig. 72 and OB2 - see fig. 72).

From both plots it can be clearly seen, that the depletion voltage is ever increasing with the level of irradiation. Nevertheless the S/N is well above 12 at 400 V of reverse bias voltage for all modules!

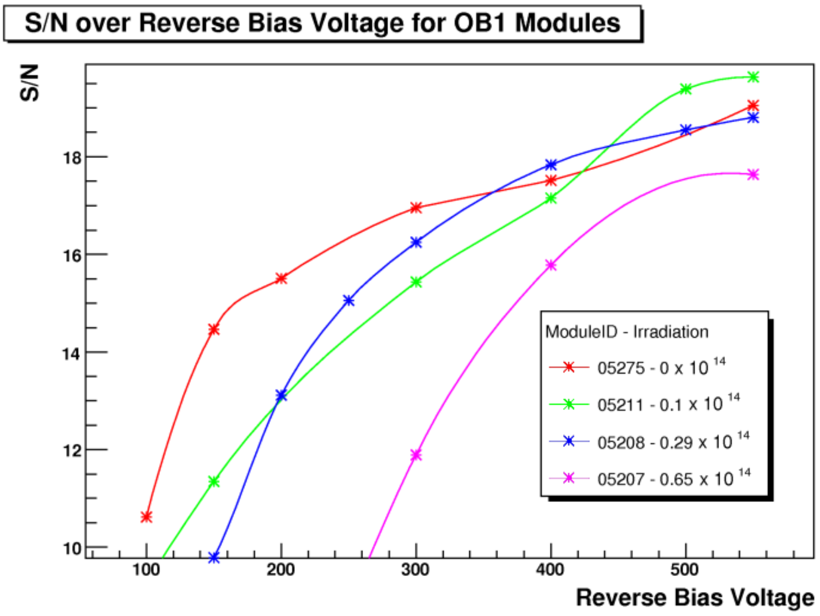

Figure 71: S/N over reverse bias voltage for 4 OB1 modules of different irradiation levels. Temperature was at -15°C. The legend shows the module IDs and the integrated fluence in 10^{14} 1 MeV neutron equivalents.

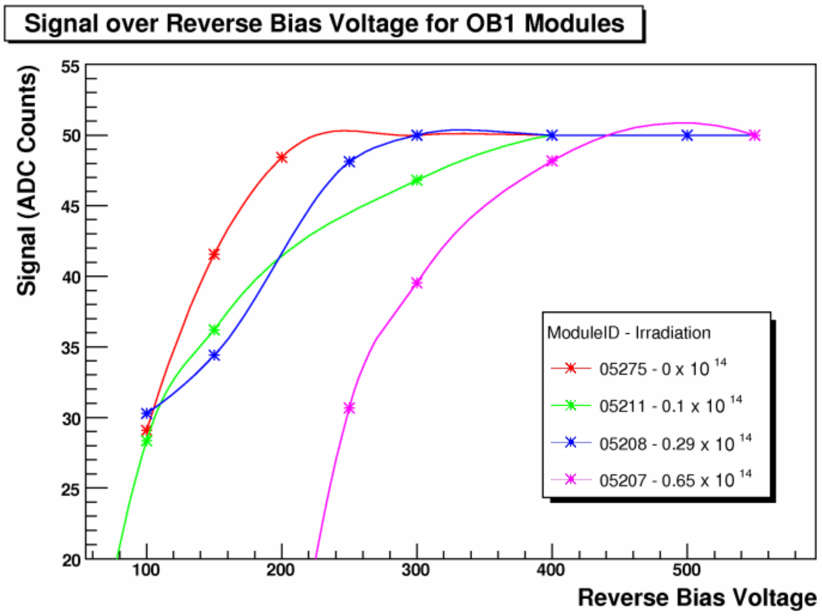

Figure 72: Signal over reverse bias voltage for 4 OB1 modules of different irradiation levels. Temperature was at -15°C. The legend shows the module IDs and the integrated fluence in 10^{14} 1 MeV neutron equivalents.

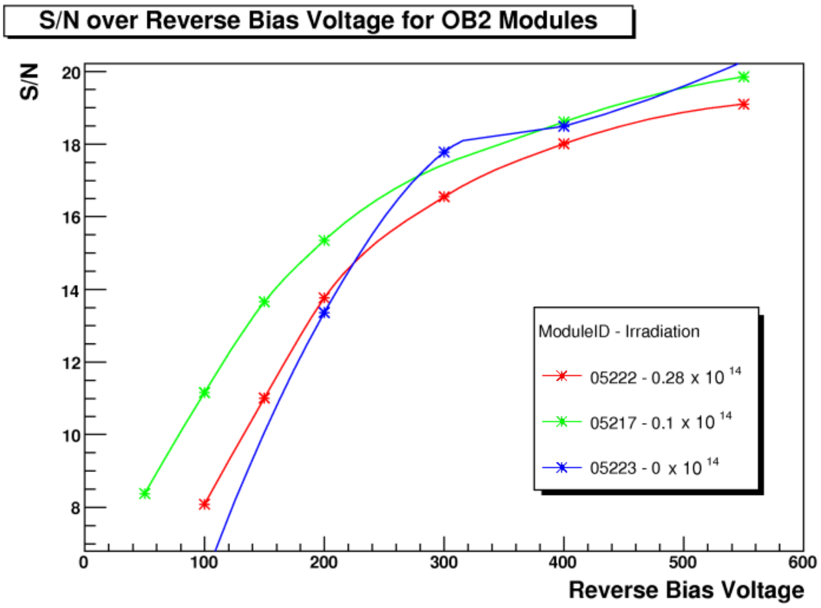

Figure 73: S/N over reverse bias voltage for 3 OB2 modules of different irradiation levels. Temperature was at -15°C. The legend shows the module IDs and the integrated fluence in 10^{14} 1 MeV neutron equivalents.

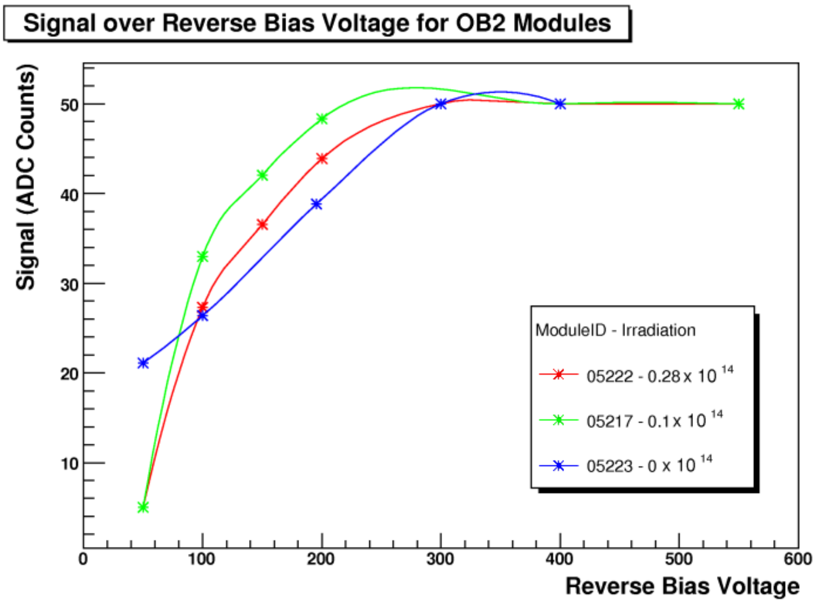

Figure 74: Signal over reverse bias voltage for 3 OB2 modules of different irradiation levels. Temperature was at -15°C. The legend shows the module IDs and the integrated fluence in 10^{14} 1 MeV neutron equivalents.

7.6.3 Conclusion

We have seen that with the modules used in the DESY 22/04 testbeam, we achieved a S/N of well above 12, when the reverse bias voltage is set to at least 400 V. This holds true for OB1 modules and even more for the less critical OB2 modules[29].

For practical reasons, it might be a good suggestion to set the reverse bias voltage for all OB1 and OB2 modules to 400 V. This should ensures that most modules are well within working conditions for most of the LHC lifetime. It might be necessary to increase the voltage for certain modules in the OB1 layer towards the end of LHC operation time.

---

[29] The OB2 layer is farther away from the interaction point and does therefore experience less irradiation than OB1

8 Summary

After having reviewed some basic information about the LHC and CMS experiment in general, this thesis gave a short introduction in the current state of silicon sensor design. After reviewing the quality assurance scheme for the detector module production in general, we had a closer look on three important steps, which were conducted by the author.

We have shown for the sensor QA, that a sophisticated, predefined QA scheme is very important, but that one has to keep an eye on unexpected deviations from the anticipated specifications. In section 6 the author presented such a study which, due to the extended secretiveness of commercial companies, the findings of the work and its effects on the manufacturing process could not be closely linked. Nevertheless the study proofed to be useful, as the observed defects were significantly reduced in the subsequent production.

The very delicate assembly and bonding procedure of the detector modules is monitored by a sophisticated hardware and software system set up by the author. We have shown in section 5.5 that according to these test, the production quality at the HEPHY in Vienna is remarkably good. Some minor problems are described and how they were solved.

Finally we have shown in section 7, that after all the efforts put into the design and production of the silicon detector modules for the CMS tracker, they are working as expected. A strong emphasis has been put into verifying, that detectors which have already been exposed to radiation comparable of up to the full 10 years of LHC lifetime, are still working within the necessary S/N limits. The results look very promising and our small sample for the outer barrel region suggest, that the tracker will still functional, until the end of the foreseen LHC lifetime.

Acknowledgements

First an foremost, I'd like to thank my supervisor *Manfred Krammer* for giving me the opportunity work on such an interesting field.

A number of people at the HEPHY in Vienna have helped me to successfully accomplish my work: *Markus Friedl* with many helpful tips on electronics, *Rudolf Eitelberger* and *Roland Stark* by perfectly assembling the measurement setups, *Margit Oberegger* and *Dieter Uhl* for doing a precise job on testing, bonding and handling many sensors and modules, *Josef Hrubec* for always having some advice, *Edmund Widl* who is the perfect man for theoretical questions, while his soldering performance is mediocre, *Stephan Hänsel* for keeping the module test business in perfect working condition and last, but not least *Thomas Bergauer* for myriads of tips, hints, books, queries, hardware, software, ...

Further thanks to those folks having endured the long data taking nights and days at the DESY testbeam: *Georg Steinbrück*, *Marcel Bleyl* and *Markus Stoye*. Further more to *Thomas Weiler* for the execellent work on the analysis macros.

Many thanks to the *Fachschaft Physik* at the Vienna University of Technology. I have spent many delightful hours of learning, discussing, playing, despairing and having a few beers there without which I could have never made it through the whole mess of studying physics. Extra credits go to my long time fellows: *Stephan Hänsel*, *Vinzent Schwarz* and *Edmund Widl*!

An extra special thanks to my parents *Gerda* and *Voja Dragicevic* who have always supported me with all the care they could find.

Danke das ihr immer an mich geglaubt habt und es auch immer noch tut!

Finally I have to give all my gratitude to *Karin Schnelzer*, who is an essential part of my live now. Your support was so very important to achieve all this and more.

Danke Käfer!

References

[1] G. Flügge at al., **CMS Tracker Technical Design Report,** CERN/LHCC 98-6, CMS TDR 5, 1998.

[2] C. Bozzi et al., **Test Results on Heavily Irradiated Silicon Detectors for the CMS Experiment at LHC,** IEEE Transactions on Nuclear Science, Vol. 47, No. 6, December 2000.

[3] A. Vasilescu, Gunnar Lindström, **Notes on the fluence normalisation based on the NIEL scaling hypothesis,** Available as ROSE/TN/2000-02 on `http://cern.ch/rd48`.

[4] J. Bartels et al., **The European Physical Journal C,** Springer Verlag, Vol. 15, No.1-4, 2000.

[5] M. Friedl et al., **Cooling Box Webpage,** Available at `http://wwwhephy.oeaw.ac.at/u3w/f/friedl/www/coolingbox/`.

[6] I. Tomalin et al., **Beam/System-Test Analysis,** Available at `http://cms-btau-datahandling.web.cern.ch/cms-btau-datahandling/`.

[7] S. Wynhoff et al., **CMS OO Reconstruction,** Available at `http://cmsdoc.cern.ch/orca/`.

[8] R. Brun et al., **ROOT - An Object-Oriented Data Analysis Famework,** Available at `http://root.cern.ch/`.

[9] D. R. Nygren, J. N. Marx, **The Time Projection Chamber,** Physics Today, 31 (1978) 46.

[10] J. -L. Agram et al., **The silicon sensors for the Compact Muon Solenoid trackerdesign and qualification procedure,** Nuclear Instruments and Methods A, Volume 517, Issues 1-3, 2004.

```
******* please make use of * or / if you add a commenting line
*******************************************************
******* Types of Interface: 1 = PCISA, 2 = EPP (0x278),  3 = EPP (0x378)
_Interface:  1
******* Directory for Data Storage:
_Directory: H:\ARCtests
******* Test Center
_Center: VIENNA
******* Operator(your name)
_Operator: Marko Dragicevic
******* oject type[(0)hybrid, (1)hybrid with pa, (2) mmodule]
_Test_object_type:  2
******* parameter settings for cuts
_testsettings_file_name: TEC_R2_testsettings_v3.xml
******* automated initialisation [(0)no, (1)yes] (don't forget to enter the board types and addresses
******* at the end of this config file)
******* auto_init: 0 is presently deactivated !!!
_auto_init: 1
******* start operator modus(no interaction necessary)[(0)no; 1yes]
_operator_modus: 0
******* tell Lyon the number of your ARC board and your ARC FE adapter
******* and they will provide you with a tool_id with you have to enter here!
_tool_id: 1500
******* enter your center type [(0)hybrid test;1 gantry;2 bonding;3 module test]
_center_type: 3
******* You like to perform a cooling cycle? [(0) no, 1 yes]
_cooling_cycle:  0
******* enter the tests which should be marked if "select all tests" button in pushed in all tests
******* presently you can choose 25 different test on the all tests page so that 2^25-1=33554431 is max
/Hybrid: _all_tests: 262142
/Module:
_all_tests: 12599295
******* if you want to start now enter your board types and their address which is defined by the DIL switch
******* on every board; note ARC boards have 8, LED and HV boards have 9 digits
******* ARC 00000100 would be an ARC board where just bit 6 on your switch is set
******* note that you assign the ARC board with its DEPP and LED boards (arranging them directly one after the other)
_ARC:  00000100
_DEPP: 000000110
_LED1: 000000010
```

```xml
<?xml version="1.0" encoding="ISO-8859-1" ?>
<!DOCTYPE Setting   SYSTEM "arcssettings.dtd">

<Setting name="arcs">

<ArcsPedRunDescriptor name="peakinvon" nevents="5000" absPinholeNoise="0.50"
absTwoOpenNoise="0.50" absOneOpenNoise="0.70" absNoisy="1.35"/>
<ArcsPedRunDescriptor name="peakinvoff" nevents="5000"  absPinholeNoise="0.50"
absTwoOpenNoise="0.50" absOneOpenNoise="0.70" absNoisy="1.35"/>
<ArcsPedRunDescriptor name="decinvon" nevents="5000" absPinholeNoise="0.70"
absTwoOpenNoise="0.70" absOneOpenNoise="1.05" absNoisy="1.75"/>
<ArcsPedRunDescriptor name="decinvoff" nevents="5000" absPinholeNoise="0.70"
absTwoOpenNoise="0.70" absOneOpenNoise="1.05" absNoisy="1.75"/>

<ArcsPShRunDescriptor name="peakinvon" nevents="10" minLat="13"/>
<ArcsPShRunDescriptor name="peakinvoff" nevents="10" minLat="13"/>
<ArcsPShRunDescriptor name="decinvon" nevents="10" minLat="13"/>
<ArcsPShRunDescriptor name="decinvoff" nevents="10" minLat="13"/>

<ArcsPipeRunDescriptor name="peakinvon" nevents="100"/>
<ArcsPipeRunDescriptor name="peakinvoff" nevents="100"/>
<ArcsPipeRunDescriptor name="decinvon" nevents="100"/>
<ArcsPipeRunDescriptor name="decinvoff"  nevents="100"/>

<ArcsGainRunDescriptor name="peakinvon"  nevents="100"/>
<ArcsGainRunDescriptor name="peakinvoff" nevents="100"/>
<ArcsGainRunDescriptor name="decinvon" nevents="100"/>
<ArcsGainRunDescriptor name="decinvoff" nevents="100"/>

<ArcsLEDRunDescriptor name="default"/>
<ArcsIVRunDescriptor name="default"/>
<ArcsPinHRunDescriptor name="default"/>
<ArcsCutsDescriptor name="default"/>

<ArcsPShCutDescriptor name="decinvon" Height_Perc_vevelo="20" Height_Perc_velo="20" Height_Perc_lo="20"
Height_Perc_hi="20" Height_Perc_vehi="20" PeakTime_Abs_vevelo="30" PeakTime_Abs_velo="30" PeakTime_Abs_lo="3"
PeakTime_Abs_hi="3" PeakTime_Abs_vehi="5"/>
<ArcsPShCutDescriptor name="decinvoff" Height_Perc_vevelo="20" Height_Perc_velo="20" Height_Perc_lo="20"
Height_Perc_hi="20" Height_Perc_vehi="20" PeakTime_Abs_vevelo="30" PeakTime_Abs_velo="30" PeakTime_Abs_lo="3"
PeakTime_Abs_hi="3" PeakTime_Abs_vehi="5"/>
```

```
<ArcsPShCutDescriptor name="peakinvon" Height_Perc_vevelo="15" Height_Perc_velo="15" Height_Perc_lo="15"
Height_Perc_hi="15" Height_Perc_vehi="15" PeakTime_Abs_vevelo="30" PeakTime_Abs_velo="30" PeakTime_Abs_lo="5"
PeakTime_Abs_hi="5" PeakTime_Abs_vehi="5"/>
<ArcsPShCutDescriptor name="peakinvoff" Height_Perc_vevelo="15" Height_Perc_velo="15" Height_Perc_lo="15"
Height_Perc_hi="15" Height_Perc_vehi="15" PeakTime_Abs_vevelo="30" PeakTime_Abs_velo="30" PeakTime_Abs_lo="5"
PeakTime_Abs_hi="5" PeakTime_Abs_vehi="5"/>

<ArcsPinHCutDescriptor name="decinvoff" PinMax_Abs_vevelo="0" PinMax_Abs_velo="0" PinMax_Abs_lo="0"
PinMax_Abs_hi="20" PinMax_Abs_vehi="40"/>
<ArcsPinHCutDescriptor name="peakinvoff" PinMax_Abs_vevelo="0" PinMax_Abs_velo="0" PinMax_Abs_lo="0"
PinMax_Abs_hi="20" PinMax_Abs_vehi="40"/>

<ArcsGainCutDescriptor name="decinvon"/>
<ArcsGainCutDescriptor name="decinvoff"/>
<ArcsGainCutDescriptor name="peakinvon"/>
<ArcsGainCutDescriptor name="peakinvoff"/>

<ArcsBPPRunDescriptor name="decinvon" nevents="50" spacer_min="3" spacer_max="22"/>
<ArcsBPPRunDescriptor name="decinvoff" nevents="50" spacer_min="3" spacer_max="22"/>
<ArcsBPPRunDescriptor name="peakinvon" nevents="50" spacer_min="3" spacer_max="22"/>
<ArcsBPPRunDescriptor name="peakinvoff" nevents="50" spacer_min="3" spacer_max="22"/>

<!--the 'PropertiesUsed' define which 'TestObjectProperties' are used as the default value -->
<PropertiesUsed  TestObjectProperties="W4_TEC" />

********************
55 lines omitted
********************

<I2CDescriptor  name="default"
  Mode="15"
  Latency="4"
  Vpsp="35"
/>

*******************
rest omitted
*******************

</Setting>
```